

Copyright
by
Jeremy Stuart Faker
2014

The Thesis Committee for Jeremy Stuart Faker
Certifies that this is the approved version of the following thesis:

**Comparison of Seismic Site Response Analysis and
Downhole Array Recordings for Stiff Soil Sites**

APPROVED BY
SUPERVISING COMMITTEE:

Supervisor:

Ellen M. Rathje

Brady R. Cox

**Comparison of Seismic Site Response Analysis and
Downhole Array Recordings for Stiff Soil Sites**

by

Jeremy Stuart Faker, B.S.

Thesis

Presented to the Faculty of the Graduate School of

The University of Texas at Austin

in Partial Fulfillment

of the Requirements

for the Degree of

Master of Science in Engineering

The University of Texas at Austin

May 2014

Dedication

To my parents, Phil and Jane, and my brother, Jason: thank you for your unconditional love and support.

Acknowledgements

I would like to express my sincere gratitude to my advisor, Dr. Ellen Rathje, for her guidance, assistance, patience, and support throughout this research project. She has helped develop my competency in, and critical understanding of, geotechnical engineering. She is an outstanding professor, teacher, researcher, and mentor. I am privileged to have had the opportunity to work with and learn from her.

I would also like to thank Dr. Brady Cox for his guidance, patience, and support during my time at the University of Texas.

I also extend my sincere thanks to George Zalachoris. Despite the demands of his own doctoral studies, George generously donated his time to provide me with data necessary to complete this research and to answer my questions. I am appreciative and grateful for his assistance and encouragement.

I would also like to thank my fellow graduate students for their friendship and support.

Abstract

Comparison of Seismic Site Response Analysis and Downhole Array Recordings for Stiff Soil Sites

Jeremy Stuart Faker, M.S.E.

The University of Texas at Austin, 2014

Supervisor: Ellen M. Rathje

Accurately predicting surface ground motions is critical for many earthquake engineering applications. Equivalent-linear (EQL) site response analysis is a numerical technique used to compute surface ground motions from input motions at bedrock using the site-specific dynamic soil properties. The purpose of this study was to investigate the accuracy of EQL site response analysis for stiff soil sites by comparing computed and observed transfer functions and response spectral amplification.

The Kiban Kyoshin network (KiK-net) in Japan is a seismograph network consisting of downhole array sites with strong-motion accelerometers located at the ground surface and at depth. Recorded motions and shear wave velocity profiles are available for most sites. Observed transfer functions and response spectral amplification were computed for 930 individual seismic recordings at 11 stiff soil KiK-net sites. Computed transfer functions and response spectral amplification were calculated from EQL site response analysis by specifying the KiK-net base sensor motion as the input motion. Sites were characterized using the measured shear wave velocity profiles and

nonlinear soil properties estimated from empirical models. Computed and observed transfer functions and response spectral amplification were compared at different levels of strain for each site. The average difference between the observed and computed response spectral amplification across the 11 sites were compared at different levels of strain.

Overall, there is reasonable agreement between the computed and observed transfer functions and response spectral amplification. There is agreement between the computed and observed site periods, but with over-prediction of the computed response at the observed site periods. Higher modes often computed by the theoretical model were not always observed by the recordings. There is very good agreement between the computed and observed transfer functions and response spectral amplification for periods larger than the site periods. There is less agreement between the computed and observed transfer functions and response spectral amplification for periods less than the site periods. There is mostly over-prediction of the response spectral amplification at these periods, although some under-prediction also occurred. Across all 11 sites the computed spectral amplification is within +/-20% at shear strains less than 0.01%. At shear strains between approximately 0.01 and 0.03%, the spectral amplification is over-predicted for these sites, in some instances by as little as 5% and in other instances by a factor of 2 or more.

Table of Contents

Abstract	vi
List of Tables	x
List of Figures	xii
Chapter 1: Introduction	1
1.1 Research Significance & Objectives.....	1
1.2 Organization of Thesis	2
Chapter 2: Site Response Analysis Techniques.....	3
2.1 Introduction.....	3
2.2 Influence of Soil Conditions on Earthquake Shaking.....	3
2.3 Wave Propagation Analysis.....	9
2.4 Equivalent-Linear Site Response Analysis.....	14
2.5 Summary.....	19
Chapter 3: Selection and Characterization of Downhole Array Sites.....	20
3.1 Introduction.....	20
3.2 Downhole Arrays	20
3.3 Available Data from KiK-net.....	21
3.4 Site Selection	23
3.5 Site Characterization.....	29
3.6 Summary.....	31

Chapter 4: Comparison of Computed and Observed Site Response.....	32
4.1 Introduction.....	32
4.2 Example of Site Response Comparison.....	32
4.3 Low Intensity Shaking.....	46
4.4 Large Intensity Shaking.....	53
4.5 Aggregated Results.....	67
Chapter 5: Summary, Conclusions, and Recommendations.....	74
5.1 Summary.....	74
5.2 Conclusions.....	75
5.3 Recommendations for Future Studies.....	76
Appendix A: Individual Site Average Residual Plots.....	77
Appendix B: Layer Discretization for EQL Site Response Analysis.....	80
Appendix C: Site Boring Logs.....	85
References.....	106

List of Tables

Table 3.1: Final sites selected including prerequisite criteria.....	25
Table 4.1: Strain bins for site response comparison	36
Table 4.2: Site IWTH27 layer discretization for EQL site response analysis	38
Table 4.3: Number of recordings assigned to strain bins for site IWTH27	39
Table 4.4: Total number of KiK-net recordings per site and corresponding strain bins	46
Table 4.5: Reported and adjusted shear wave velocity profiles for site IWTH04.....	52
Table 4.6: Largest calculated maximum shear strain at the 11 sites.....	60
Table 4.7: Summary of computed, observed, and approximated KiK-net site periods	68
Table 4.8: Number of recordings per strain bin for average residual contour color plots	70
Table 4.9: Percent contribution of recordings to strain bin per site and percent contribution of each strain bin to total number of motions for aggregate average residual contour color plots	70
Table B.1: Site FKSH09 layer discretization for EQL site response analysis.....	81
Table B.2: Site IWTH04 layer discretization for EQL site response analysis.....	81
Table B.3: Site IWTH05 layer discretization for EQL site response analysis.....	81

Table B.4: Site IWTH21 layer discretization for EQL site response analysis.....	82
Table B.5: Site IWTH24 layer discretization for EQL site response analysis.....	82
Table B.6: Site IWTH25 layer discretization for EQL site response analysis.....	82
Table B.7: Site IWTH27 layer discretization for EQL site response analysis.....	83
Table B.8: Site MYGH06 layer discretization for EQL site response analysis.....	83
Table B.9: Site NIGH09 layer discretization for EQL site response analysis.	83
Table B.10: Site NIGH12 layer discretization for EQL site response analysis.....	84
Table B.11: Site SMNH01 layer discretization for EQL site response analysis...	84

List of Figures

Figure 2.1: Schematic of site response analyses	4
Figure 2.2: Refraction of seismic shear waves while propagating from source to site surface	5
Figure 2.3: Locations of UNAM and SCT strong-motion instrument stations in Mexico City with respect to Foothill, Transition, and Lake Zones, and with respect to depth of soft soil	6
Figure 2.4: Acceleration-time series recorded at UNAM and SCT strong-motion instrument stations from 1985 Michoacán Earthquake and corresponding response spectra	8
Figure 2.5: Acceleration-time domain method sequence	10
Figure 2.6: Site response analysis nomenclature	12
Figure 2.7: Comparison of example transfer functions using input outcrop motion and input within motion at bedrock	13
Figure 2.8: Stress-strain behavior of cyclically loaded soils	15
Figure 2.9: Shear modulus represented as backbone curve	16
Figure 2.10: Strain-compatible shear modulus and damping ratio iterations	17
Figure 2.11: Example shear strain-time series and effective strain	18
Figure 3.1: Map of Japan with location of final 11 sites selected.....	25
Figure 3.2: Shear wave velocity profiles of 11 sites selected	26

Figure 3.3: Z_{1000} and V_{s30} for final selected sites	27
Figure 3.4: D_{base} and V_{s30} for final selected sites.....	28
Figure 3.5: Example Darendeli and Stokoe (2001) modulus reduction and damping curves at mean effective stresses of 0.25, 1.0, 4.0, and 8.0 atm, and Schnabel (1973) rock modulus reduction and damping curves	30
Figure 4.1: Shear wave velocity profile for site IWTH27	33
Figure 4.2: Computed peak shear strain with depth for three input motions of varying PGA_{base} for site IWTH27.....	34
Figure 4.3: Comparison of calculated maximum shear strain from EQL site response analysis and corresponding observed PGA_{base} for 930 KiK-net recordings	35
Figure 4.4: Strain bins for site response comparison relative to example modulus reduction curve and damping curve	37
Figure 4.5: Computed and observed transfer functions for site IWTH27	40
Figure 4.6: Computed and observed response spectral amplification for site IWTH27.....	42
Figure 4.7: Average residuals plotted versus period T and T/T_{SITE} for site IWTH27.....	45
Figure 4.8: Transfer functions for low intensity shaking with calculated maximum shear strains less than 0.01%	48
Figure 4.9: Spectral amplification for low intensity shaking with calculated maximum shear strains less than 0.01%	50

Figure 4.10: Observed and computed spectral amplification using reported and adjusted shear wave velocity profiles for site IWTH04	52
Figure 4.11: Transfer functions for large intensity shaking with calculated maximum shear strains between 0.01 and 0.03%	54
Figure 4.12: Transfer functions for large intensity shaking with calculated maximum shear strains between 0.03 and 0.1%	55
Figure 4.13: Transfer functions for large intensity shaking with calculated maximum shear strains of 0.1% or greater	56
Figure 4.14: Observed transfer functions with calculated maximum shear strains less than 0.01%, 0.01 - 0.03%, 0.03 - 0.1%, and 0.1% or greater	57
Figure 4.15: Computed transfer functions with calculated maximum shear strains less than 0.01%, 0.01 - 0.03%, 0.03 - 0.1%, and 0.1% or greater	58
Figure 4.16: Spectral amplification for large intensity shaking with calculated maximum shear strains between 0.01 and 0.03%	62
Figure 4.17: Spectral amplification for large intensity shaking with calculated maximum shear strains between 0.03 and 0.1%	63
Figure 4.18: Spectral amplification for large intensity shaking with calculated maximum shear strains of 0.1% or greater	64
Figure 4.19: Observed spectral amplification with calculated maximum shear strains less than 0.01%, 0.01 - 0.03%, 0.03 - 0.1%, and 0.1% or greater	65
Figure 4.20: Computed spectral amplification with calculated maximum shear strains less than 0.01%, 0.01 - 0.03%, 0.03 - 0.1%, and 0.1% or greater	66

Figure 4.21: Aggregate average residuals plotted versus period T and T/T_{SITE}
for 910 motions across 11 sites73

Figure A.1: Average residuals plotted versus period T for the 11 sites.....78

Figure A.2: Average residuals plotted versus T/T_{SITE} for the 11 sites.....79

Chapter 1: Introduction

1.1 RESEARCH SIGNIFICANCE & OBJECTIVES

Predicting surface ground motions is an important aspect of geotechnical earthquake engineering. Predicted surface ground motions are required for many earthquake engineering applications including the development of structural design spectra, dynamic structural analyses, evaluation of liquefaction potential, and seismic slope stability analyses. Recorded surface ground motions are rarely available at a given location and local soil conditions play a significant role in determining surface ground motion characteristics. Site response analyses are numerical techniques that use wave propagation to compute surface ground motions from input motions at bedrock using the site-specific dynamic soil properties. Equivalent-linear (EQL) site response analysis is often considered adequate to model the non-linear dynamic response of stiff soil. The ability to accurately predict surface ground motions from EQL site response analysis is critical to earthquake engineers.

The main objective of this research is to investigate the accuracy of EQL site response analysis for stiff soil sites. Specifically, this study compares observed transfer functions and response spectral amplification determined from 930 individual seismic recordings at 11 stiff soil downhole array sites in Japan with those computed using EQL site response analysis. The average difference between the observed and computed response spectral amplification across the 11 sites is evaluated at different levels of earthquake-induced shear strain.

1.2 ORGANIZATION OF THESIS

This thesis is organized into five chapters. After this introduction, Chapter 2 discusses the influence of local soil conditions on earthquake shaking and the basic concepts behind EQL site response analysis.

Chapter 3 discusses available data from the Kiban Kyoshin strong-motion seismograph network (KiK-net) in Japan. The selection and characterization of stiff soil KiK-net downhole array sites for use in this study are described, and the final 11 selected sites are presented.

Chapter 4 discusses the site response comparison for the 11 sites. The computed and observed transfer functions and response spectral amplification are presented and compared for low intensity and large intensity shaking and at different levels of strain. The aggregate average difference between the observed and computed spectral amplification at different levels of strain is presented and discussed.

Chapter 5 summarizes the results from this study and presents the general conclusions. Recommendations are offered for future site response comparison studies at stiff soil sites.

Chapter 2: Site Response Analysis Techniques

2.1 INTRODUCTION

This chapter discusses the techniques of one-dimensional site response analyses for predicting surface ground motions for earthquake engineering applications. The influence of soil conditions on earthquake shaking is demonstrated. The linear-elastic wave propagation techniques used to predict earthquake motions at the ground surface are described. The equivalent-linear approximation to the nonlinear response of the soil is also presented.

2.2 INFLUENCE OF SOIL CONDITIONS ON EARTHQUAKE SHAKING

One-dimensional site response analyses are numerical techniques that predict surface ground motions for the purpose of determining structural design spectra or surface time series for subsequent advanced earthquake engineering analyses. A surface ground motion (output motion) is predicted by specifying a recorded motion at the bedrock (input motion), and propagating the input motion through a uniform or layered soil medium to the ground surface. The input parameters for site response analyses include the shear wave velocity (V_s), unit weight (γ), shear modulus (G), and damping ratio (D or ξ) of each layer of soil and the bedrock. A graphical representation of site response analyses is provided in Figure 2.1.

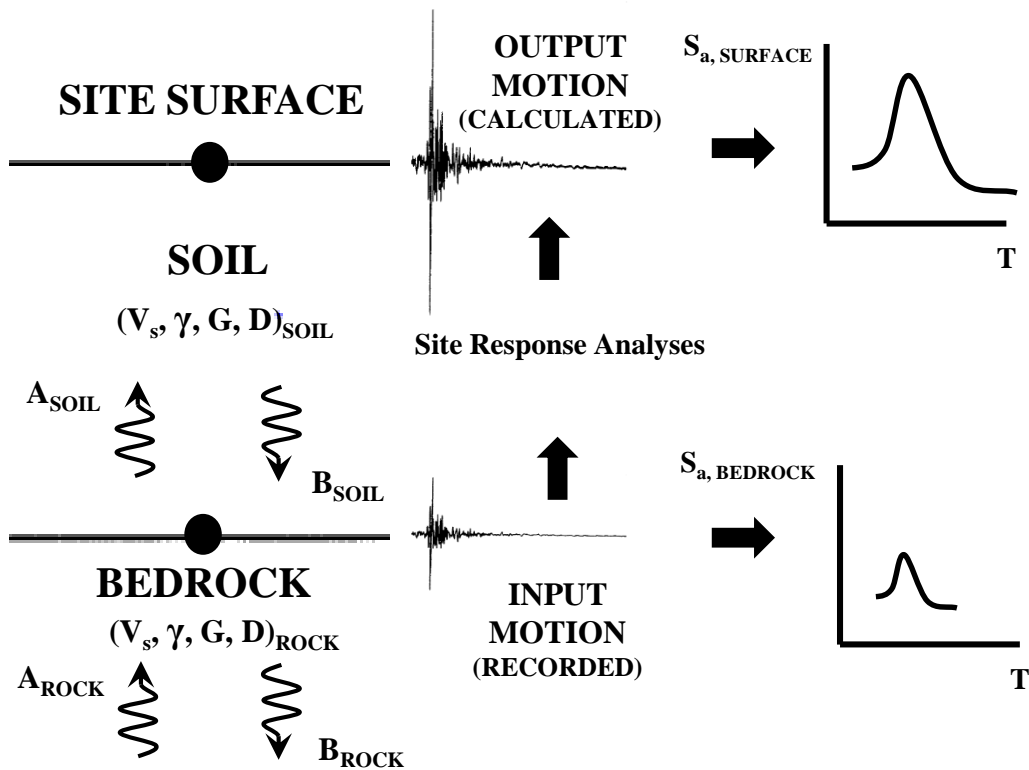


Figure 2.1: Schematic of site response analyses.

Generally, earthquakes start to rupture kilometers below the surface of the earth. As the induced earthquake waves propagate from the source, the seismic waves refract between layer boundaries and become more vertical with respect to the surface according to Snell's Law of refraction (Figure 2.2). As seismic waves reach the earth's surface, they are considered to propagate vertically (Kramer, 1996).

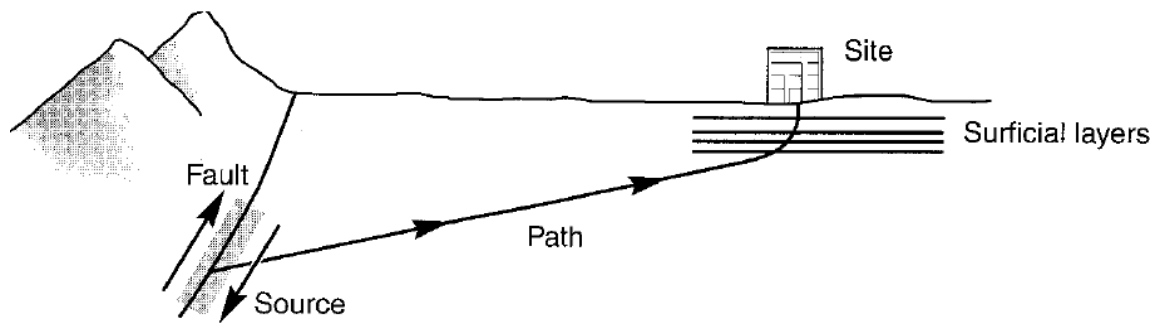


Figure 2.2: Refraction of seismic shear waves while propagating from source to site surface (Kramer, 1996).

Although seismic waves travel through kilometers of rock before reaching the ground surface, the relatively shallow surficial soil deposits above bedrock often play a significant role in determining the surface ground motion characteristics. A soil deposit can significantly amplify or dampen the motion from the bedrock as it propagates to the ground surface at a given site.

An example of this phenomenon was observed in Mexico City during the September 19, 1985 Michoacán earthquake. The epicenter of the earthquake was located 350 kilometers west of Mexico City within a subduction zone off the coast. Extensive structural damage and loss of life was observed in some zones of Mexico City, while minimal damage and loss of life was observed in others. The geology of Mexico City can be divided into three main zones with different subsurface conditions: the Foothill Zone, the Lake Zone, and the Transition Zone, as shown in Figure 2.3 (Kramer, 1996).

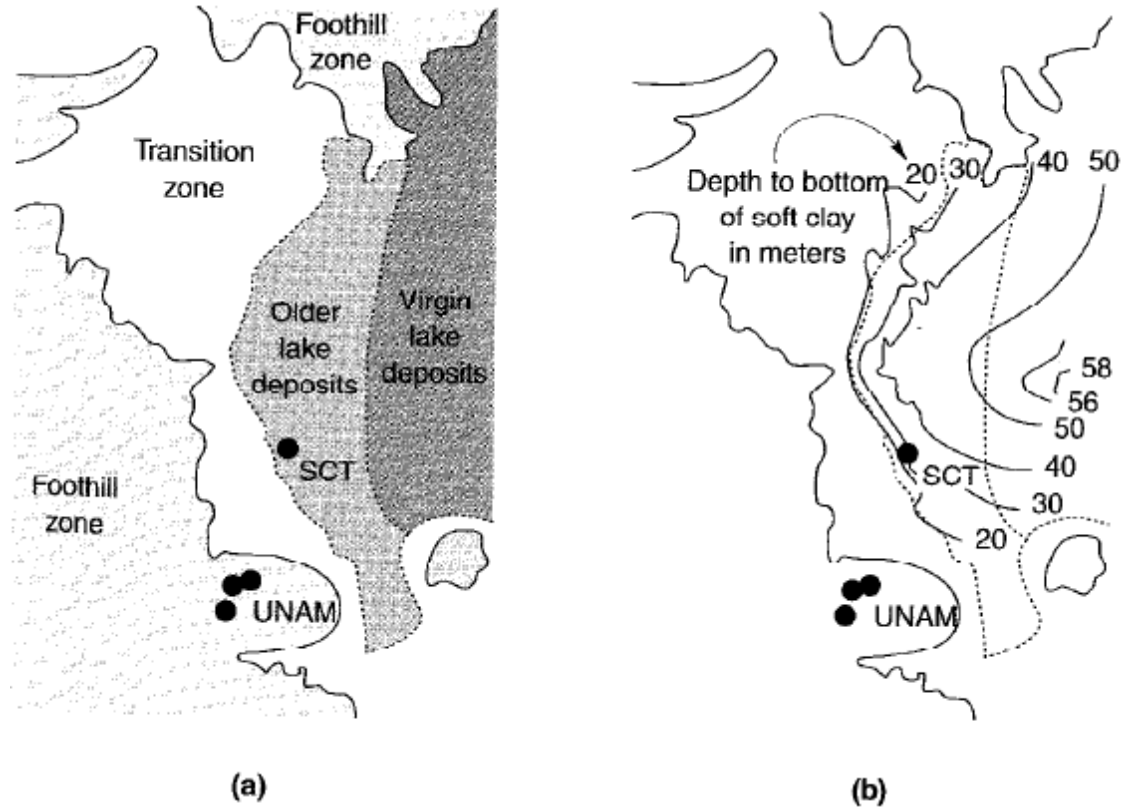


Figure 2.3: Locations of UNAM and SCT strong-motion instrument stations in Mexico City: (a) with respect to Foothill, Transition, and Lake Zones; (b) with respect to depth of soft soil (Kramer, 1996).

The Foothill Zone is composed mainly of basalt overlain by shallow deposits of granular soil. The Transition Zone is composed of thin soft soil deposits interspersed with alluvial deposits to depths of approximately 20 m. The Lake Zone is composed of very soft soils formed from the pluviation of airborne silt, clay and ash from nearby volcanoes and these deposits extend to depths greater than 55 m (Figure 2.3) (Kramer, 1996). The majority of the damage in Mexico City occurred in the Lake Zone.

Strong-motion instrument stations located at the Universidad Nacional Autonoma de Mexico (UNAM) in the Foothill Zone and at the Secretary of Communications and Transportation (SCT) in the Lake Zone recorded surface ground motions from the 1985 Michoacán earthquake (Kramer, 1996). Figure 2.3 shows the locations of the UNAM and SCT strong-motion instrument stations in relation to the geologic zones and depth to bottom of soft soil. Acceleration-time series recorded at the UNAM and SCT strong-motion instrument stations during the 1985 Michoacán earthquake and their corresponding response spectra are presented in Figure 2.4. Although the UNAM and SCT strong-motion instrument stations are less than 15 kilometers apart, the ground surface motion characteristics and corresponding response spectra differ significantly (Romo & Seed, 1986). As shown in Figure 2.4, the amplitude of the acceleration-time series from the SCT strong-motion instrument station in the Lake Zone is significantly greater than the amplitude of the acceleration-time series from the UNAM strong-motion instrument station in the Foothill Zone. In addition, the acceleration-time series from the SCT station has lower frequency content as compared to the acceleration-time series from the UNAM station. The greater amplitude and lower frequency content of the acceleration-time series of the SCT station result in greater response spectra at longer periods as compared to the response spectra from the UNAM acceleration-time series.

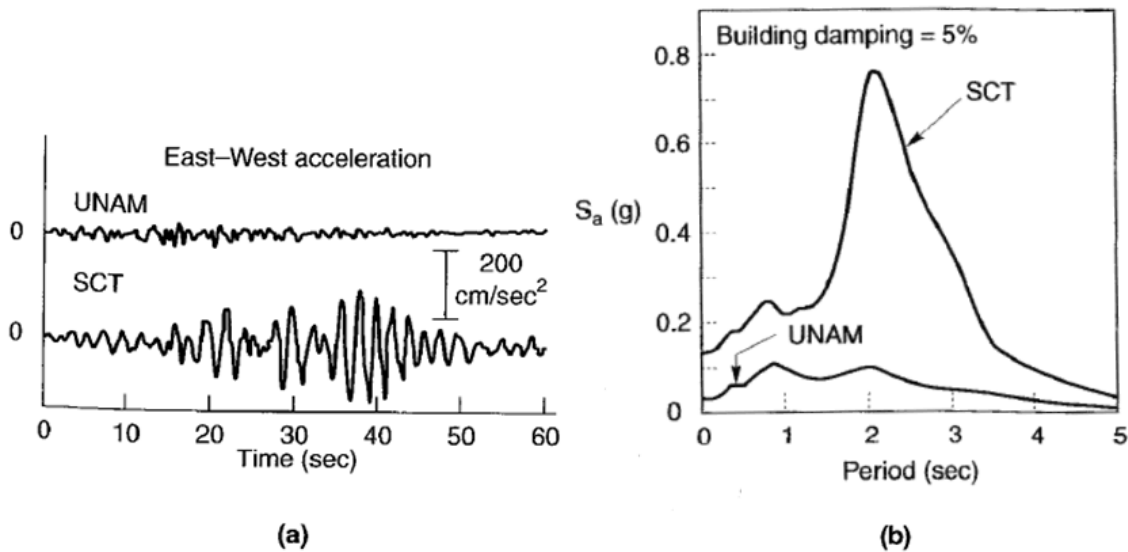


Figure 2.4: From 1985 Michoacán Earthquake: (a) acceleration-time series recorded at UNAM and SCT strong-motion instrument stations; (b) response spectra computed from recorded acceleration-time series at UNAM and SCT strong-motion instrument stations (Kramer, 1996).

The difference in surface ground motion characteristics (amplitude and frequency content of acceleration-time series) from the 1985 Michoacán earthquake can be attributed to the different characteristics of the soil deposits beneath the strong-motion stations. The shallower, stiffer soil deposits in the Foothill Zone produced less intense surface ground motions; while the deeper, softer soil deposits in the Lake Zone produced more intense surface ground motions and low frequency content. Significant structural damage and loss of life was observed in the Lake Zone of Mexico City, while damage in the Transition and Foothill Zone was less pervasive. The observations from the 1985 Michoacán earthquake demonstrate the effect of local soil conditions on surface ground motion characteristics, and the need to reasonably predict surface ground motions.

2.3 WAVE PROPAGATION ANALYSIS

One-dimensional, linear-elastic site response analysis is based on the solution to the one-dimensional, differential wave equation. The solution to the wave equation provides displacement as a function of depth and time for a given frequency of harmonic motion. The soil medium is assumed to behave as a Kelvin-Voigt solid, meaning the dynamic response of the soil medium is described using an elastic spring and a viscous dashpot. The stiffness of the spring is related to the shear modulus of the soil, and the viscosity of the dashpot is related to the damping ratio of the soil. The soil is assumed to be linear-elastic, such that the dynamic properties (shear modulus and damping ratio) do not vary with shear strain. The solution to the wave equation assumes that horizontally polarized shear waves propagate vertically from the underlying bedrock through the soil medium to the ground surface, and that all soil and rock boundaries are horizontal and extend infinitely in the horizontal direction. The bedrock is assumed to be an elastic half-space (Kramer, 1996).

Transfer functions are used to predict the surface ground motion from underlying bedrock motion. Transfer functions represent the ratio of the surface and input motion amplitudes as a function of frequency and are derived from the solution to the wave equation. This solution treats each frequency as a harmonic motion that is independent from all other frequencies. Because earthquake motions are not harmonic, the fast Fourier transform (FFT) is used to convert the input motion into the frequency domain and the transfer function is applied to the resulting Fourier amplitude spectrum (FAS). This process is illustrated in Figure 2.5. The input acceleration-time series (Figure 2.5(a)) is converted to the FAS using the FFT (Figure 2.5(b)). The transfer function (Figure 2.5(c)) is multiplied by the input FAS to generate the FAS at the top of the soil

deposit (Figure 2.5(d)). The surface FAS is converted back to the time domain using the inverse FFT to compute the acceleration-time series at the surface (Figure 2.5(e)).

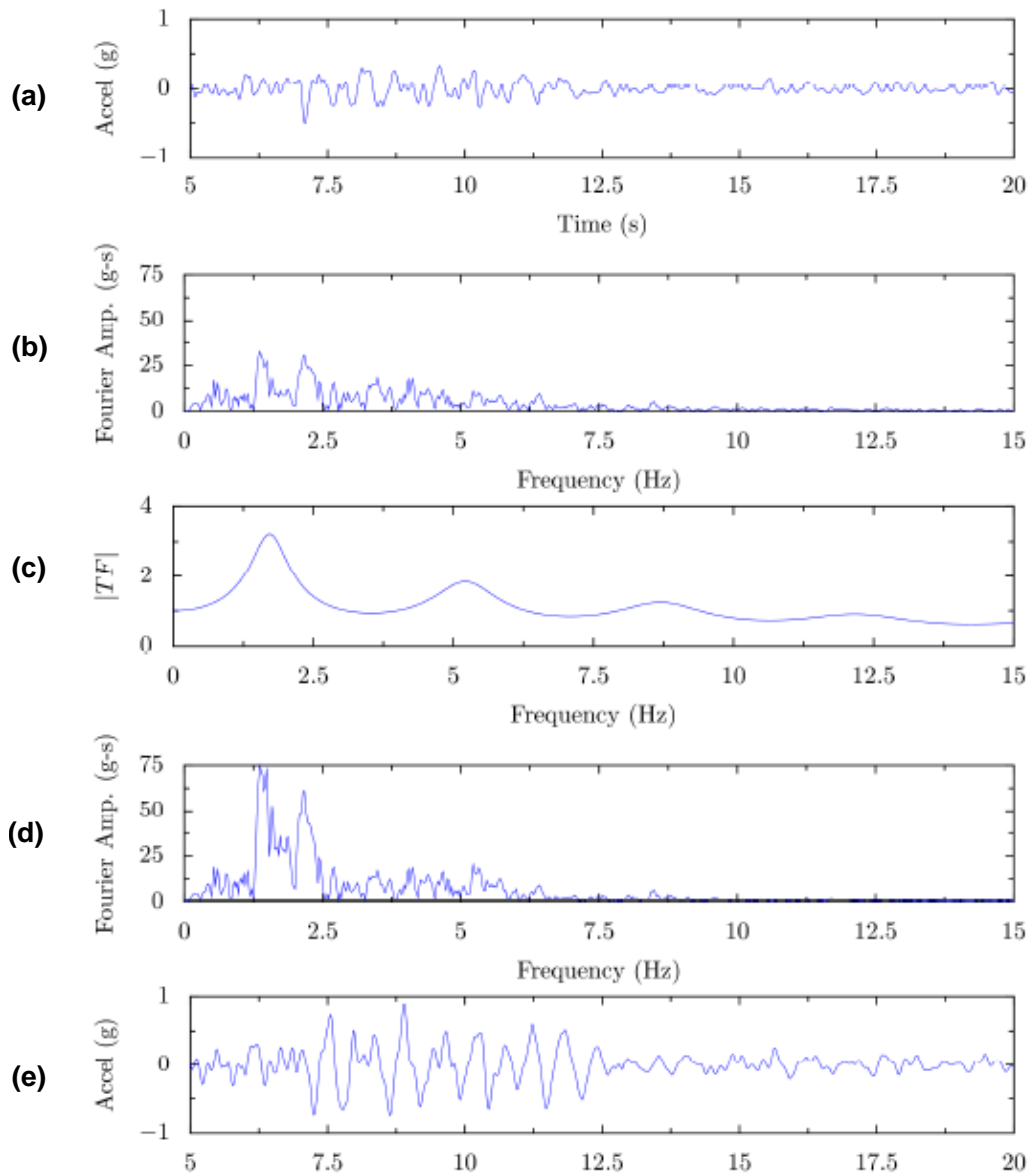


Figure 2.5: Acceleration-time domain method sequence: (a) input acceleration-time series, (b) input FAS, (c) transfer function from input to output FAS, (d) output FAS, and (e) output acceleration-time series (Kottke & Rathje, 2008).

A transfer function relates the ratio of amplitudes of the FAS as a function of frequency and illustrates the dynamic response of the soil deposit. Another way to observe the dynamic response of a soil deposit is to compute the ratio of the surface to input response spectra as a function of period. This ratio is commonly known as response spectral amplification. Because response spectra are used by engineers in various design procedures, spectral amplification is of particular interest for engineering applications. Both the transfer function and spectral amplification are representations of the same phenomenon, but their numerical values are different because a response spectrum represents the maximum responses of single-degree-of-freedom oscillators and a Fourier Amplitude Spectrum is a direct representation of an acceleration-time history.

Site response analyses are typically performed by using an input ground motion at bedrock that was recorded at a strong-motion instrument station located at the surface on outcropping rock (Figure 2.6). Motions recorded at a free surface are known as “outcrop” motions. Upward propagating seismic shear waves are completely reflected at a free surface; hence, the outcrop motions are comprised of upward and downward propagating seismic shear waves of equal magnitude A (wave amplitude $2A$). Motions recorded at depth within the ground are known as “within” motions. At a layer interface within the ground there is only partial reflection of the upward propagating seismic shear wave; hence, within motions are comprised of upward and downward propagating seismic shear waves of different magnitude (upward magnitude A and downward magnitude B ; total wave amplitude $A+B$).

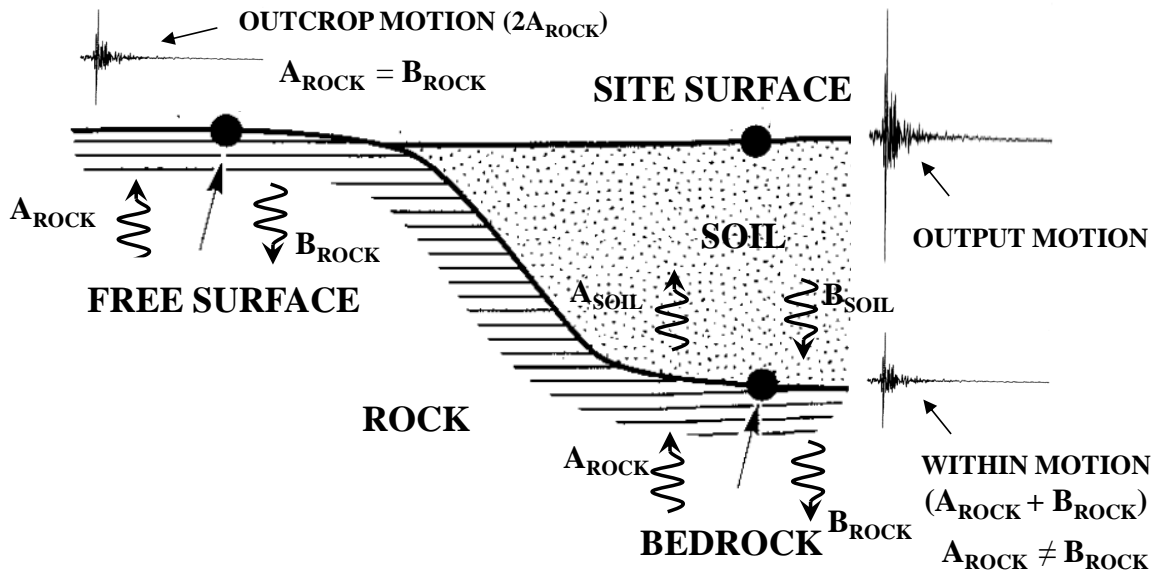


Figure 2.6: Site response analysis nomenclature.

The computed transfer function is influenced by the assumed boundary condition at the base as it relates to the recorded motion used as input. **An outcropping rock motion must be converted to a within motion before being used as an input motion.** The significance of this effect is demonstrated by Figure 2.7, which illustrates two transfer functions derived from the same input motion: one that relates the surface motion to an outcrop input motion and one that relates the surface motion to a within input motion. As shown in Figure 2.7, assuming an outcropping input motion results in a transfer function that has smaller peaks at its modal frequencies than a transfer function that assumes a within input motion. This difference is a result of the outcropping input motion being converted into a within motion as part of the analysis, which suppresses the motion at the site's modal frequencies. Most site response analyses in practice use the transfer function for outcropping input motions because recorded surface motions are

used as input. The only time that the transfer function for within motions is used is when the input motion is recorded within the ground. The distinction between outcrop input motions and within input motions is an important part of site response analysis (Kramer, 1996).

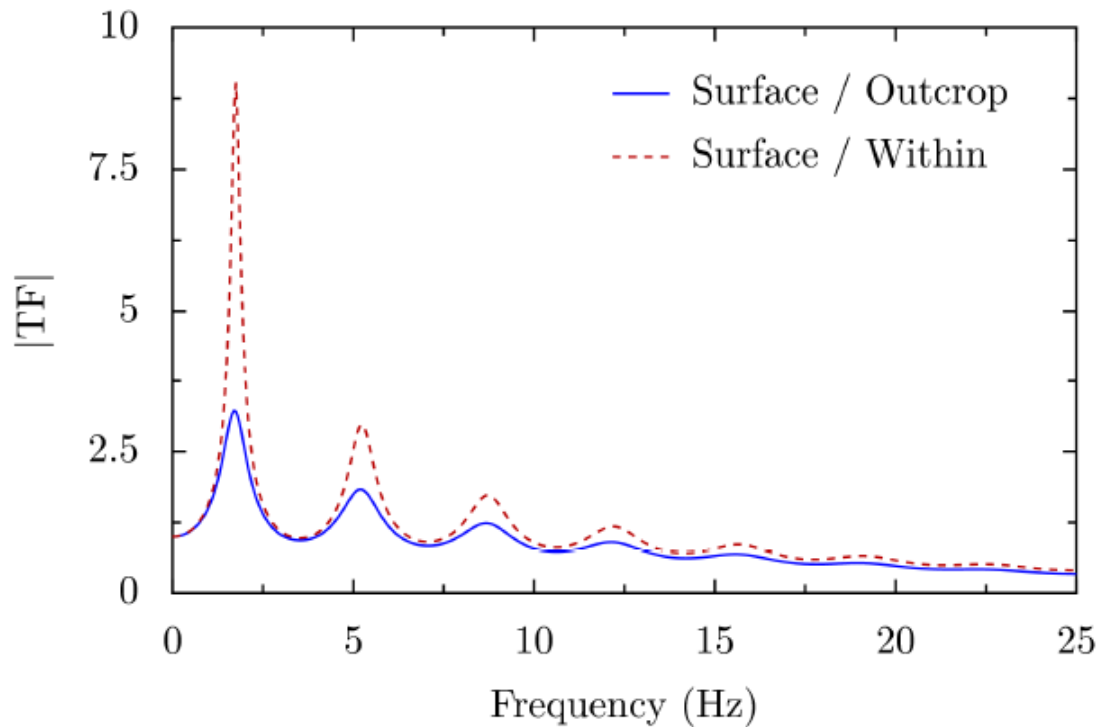


Figure 2.7: Comparison of example transfer functions using input outcrop motion and input within motion at bedrock with significant difference at modal frequencies (Kottke & Rathje, 2008).

2.4 EQUIVALENT-LINEAR SITE RESPONSE ANALYSIS

The wave propagation solution presented in the previous section assumes the soil is linear-elastic, such that the stiffness and damping does not vary with cyclically induced shear strain. In reality, the relationship between shear stress (τ) and shear strain (γ) induced by cyclic earthquake shaking is non-linear. One-dimensional, equivalent-linear (EQL) site response analysis uses the linear-elastic, wave propagation solution, but approximates of the non-linear, stress-strain behavior of soil during earthquake loading.

The stress-strain behavior of cyclically loaded soils is presented by a hysteresis loop (Figure 2.8). The slope and area of the hysteresis loop represent the average stiffness and energy dissipation (damping) of the soil, respectively (Kramer, 1996). The stiffness of the soil, determined by the tangent shear modulus (G_{tan}), varies along the hysteresis loop for a given loading cycle. However, the stiffness of the soil over the entire hysteresis loop can be approximated using the secant shear modulus (G_{sec}), which is the average of all tangent shear moduli. The energy dissipation of the soil is approximated by the damping ratio (D), which is related to the area of the hysteresis loop. The secant shear modulus and damping ratio are referred to as equivalent-linear soil properties because they approximate the non-linear behavior of soil using linear-elastic parameters (Kramer, 1996).

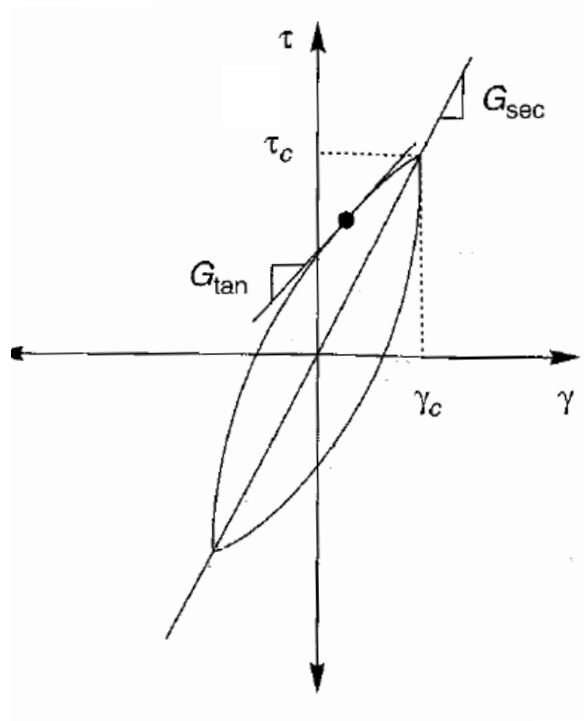


Figure 2.8: Stress-strain behavior of cyclically loaded soils depicting secant shear modulus, G_{sec} and tangent shear modulus, G_{tan} (Kramer, 1996).

The secant modulus can be derived at different strain levels from a backbone shear stress- strain curve, as shown in Figure 2.9(a). The secant shear modulus decreases with cyclic shear strain amplitude and can be normalized by the maximum secant modulus (G_{max}) and presented as a modulus reduction curve (Figure 2.9(b)). The modulus reduction curve is convenient because the maximum secant modulus can be determined accurately from the shear wave velocity of the soil, which is relatively easy to measure in the field, and the remaining part of the curve can be derived from laboratory testing. The damping ratio also varies with cyclic shear strain amplitude. The damping ratio increases with shear strain and its variation with shear strain is defined by a damping curve.

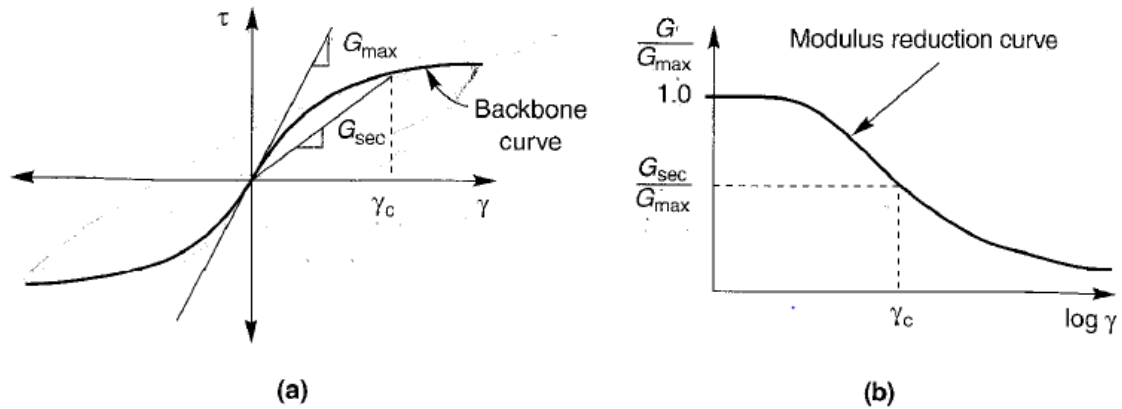


Figure 2.9: Shear modulus represented as: (a) backbone curve showing typical variation of G_{sec} with shear strain; (b) corresponding modulus reduction curve (Kramer, 1996).

The shape of the modulus reduction and damping curves are influenced by many factors including, but not limited to, confining pressure, plasticity index, void ratio, geologic age, cementation, overconsolidation ratio, strain rate, and number of loading cycles (Kramer, 1996). Various empirical models are available that predict the modulus reduction and damping curves as a function of some or all of these parameters.

The goal of EQL site response analysis is to reasonably predict surface ground shaking by incorporating the non-linear stress-strain response that is exhibited in real soils under cyclic earthquake loading. As previously stated, dynamic soil properties vary with cyclically induced shear strain, and therefore, the intensity of shaking. EQL analysis uses an iterative procedure, outlined in Figure 2.10, to determine values of shear modulus and damping ratio in each layer that are consistent with the level of shear strain induced in each layer by the input motions. In this procedure, the shear strain-time history within each layer first is computed using the initial dynamic soil properties of each layer ($G^{(1)}$)

and $\xi^{(1)}$ in Figure 2.10) and a transfer function that relates the shear strain directly to the input motion. Because the maximum shear strain acts for only a moment, an effective shear strain level is used to select the strain-compatible soil properties. The effective shear strain level is used to select the strain-compatible soil properties. The effective shear strain commonly is taken as 0.65 of the maximum shear strain. An example of a shear strain-time history and corresponding effective strain is presented in Figure 2.11. This effective shear strain ($\gamma^{(1)}$ in Figure 2.10) is used to identify the strain-compatible shear modulus and damping ratio ($G^{(2)}$ and $\xi^{(2)}$ in Figure 2.10) from the modulus reduction and damping curves for each layer. These properties are used in the next iteration of analysis that computes the effective strain in each layer and the corresponding shear modulus and damping ratio. Iterations continue until the values of the shear modulus and damping ratio determined from one iteration to the next ($G^{(2)}$ and $G^{(3)}$, and $\xi^{(2)}$ and $\xi^{(3)}$ in Figure 2.10) are within a limiting value (5% for example) for every layer. After the strain-compatible shear modulus and damping ratio are determined for each layer, the dynamic response of the soil deposit is computed using those properties (Kramer, 1996).

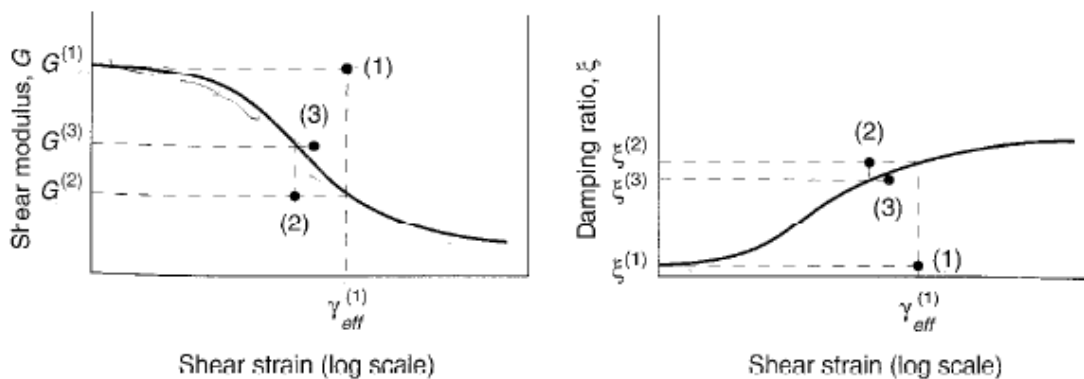


Figure 2.10: Iteration toward strain-compatible shear modulus and damping ratio for a given layer (Kramer, 1996).

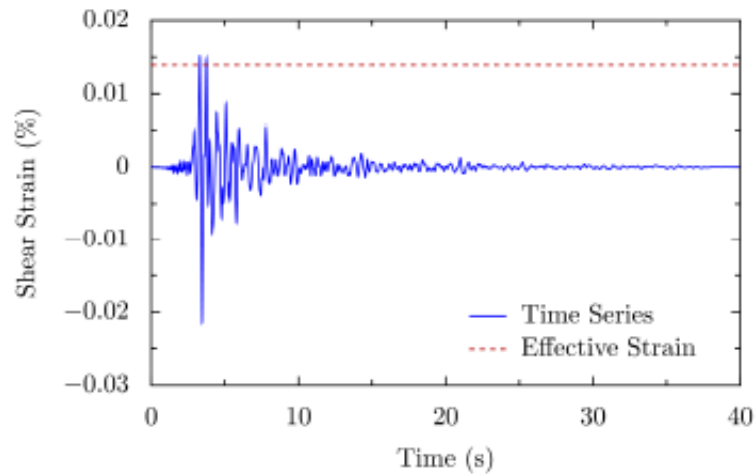


Figure 2.11: Example shear strain-time series and effective strain determined using a transfer function from an input acceleration-time series (Kottke & Rathje, 2008).

Advantages of EQL site response analysis are its computational ease and the use of soil properties that are relatively simple to obtain, such as the shear wave velocity and unit weight of the soil. EQL site response analysis can provide reasonable results for cyclically induced strain ranges up to 0.5 to 1%. Disadvantages of EQL site response analysis are that deformations or failures cannot be modeled because the analysis assumes the soil is linear-elastic and therefore the shear strain level will return to zero after loading (Kramer, 1996). Another limitation is that EQL site response analysis assumes that there is only one shear strain level per layer, when in reality, the shear strain (and, therefore, dynamic soil properties) varies throughout each layer. Due to the assumption of horizontal layers, the effects of topography cannot be modeled. Horizontal soil layers are more likely to exist naturally in softer formations deposited by slow moving alluvial environments, and less likely to exist naturally in older, stiffer formations deposited by non-alluvial environments.

2.5 SUMMARY

Local soil conditions can significantly influence the intensity and frequency content of earthquake shaking from the underlying bedrock to the ground surface. One-dimensional site response analyses are numerical techniques used to predict surface ground motions from input motions at bedrock for earthquake engineering applications. The input parameters include the shear wave velocity, unit weight, and shear modulus reduction and damping curves of the soil. Site response analyses are based on the solution to the wave equation and the assumption that horizontally polarized seismic shear waves propagate vertically through a layered or uniform soil medium from bedrock. Transfer functions are used to predict surface ground motions from underlying bedrock motions. In EQL site response analysis, the non-linear response of the soil is modeled through the selection of strain-compatible dynamic soil properties. The main advantage of EQL site response analysis is that it can quickly and efficiently provide reasonable results for cyclically induced strain ranges up to 0.5 to 1%.

Chapter 3: Selection and Characterization of Downhole Array Sites

3.1 INTRODUCTION

This chapter discusses downhole arrays and the Kiban Kyoshin strong-motion seismograph network in Japan. Published available data from the Kiban Kyoshin network is also discussed. The selection and characterization of stiff soil downhole array sites for this study are described, and the final selected sites are presented.

3.2 DOWNHOLE ARRAYS

A downhole array is a vertical borehole with high sensitivity seismographs containing strong-motion accelerometers distributed at the ground surface and at depth. The Kiban Kyoshin network (KiK-net) is a strong-motion seismograph network in Japan consisting of approximately 700 downhole array sites nationwide. Strong-motions are simultaneously recorded by KiK-net strong-motion accelerometers at the ground surface and at depth, and are transmitted directly to the data management center of the National Research Institute for Earth Science and Disaster Prevention (NIED) in Japan. NIED publishes strong-motion recordings, shear wave velocity profiles, installation depths to base sensors, and basic soil descriptions with depth for most KiK-net sites.

Using KiK-net strong motion recordings, observed response spectra at the surface and at depth can be calculated at a given site. These recordings can be used to evaluate site response analysis procedures by specifying the KiK-net base sensor motion as the input motion, and computing the surface motion using EQL site response analysis. The base sensor motion is specified as a “within” motion and the site response model for analysis is developed using the published and estimated soil properties at the site. The computed and observed transfer functions (i.e., ratio of surface Fourier amplitude

spectrum to input Fourier amplitude spectrum) and spectral amplification (i.e., ratio of surface response spectra to input response spectra) can be compared at a given site.

3.3 AVAILABLE DATA FROM KIK-NET

NIED publishes general site information (station details), boring logs including shear wave velocity profiles, and strong-motion records for most Kik-net downhole array sites. Available station details include site name, abbreviation, geographic coordinates, site map, surface altitude, and installation depth of base strong-motion accelerometers, among others.

Simple boring logs are available in Japanese for most sites, and are available in English for a limited number of sites. The original Japanese and (loosely translated) English versions of the boring logs for the sites selected for this study are provided in Appendix C. The boring logs provide basic soil and rock descriptions with layer thicknesses and geologic units; and compression and shear wave velocity profiles in both graphical and numerical form. From the published shear wave velocity profiles, the site class, average shear wave velocity over the top 30 m, and estimated depth to shear wave velocity of 1,000 m/s were determined for most sites. In situ seismic measurement techniques have been used to determine shear wave velocity profile at the sites, but the measurement technique that was used is not reported.

Strong-motion recordings are available for individual seismic events and are simultaneously recorded by strong-motion sensors at the surface and at depth. Each strong-motion sensor records two horizontal components, an East-West (EW) component and a North-South (NS) component, per seismic event. Therefore, there are four individual horizontal recordings per seismic event: surface EW, surface NS, base EW,

and base NS. In site response analysis, EW and NS components for an individual seismic event are typically analyzed separately.

Raw KiK-net strong-motion recordings were downloaded from NIED. The raw recordings are later processed using a fifth-order Butterworth, time-domain, acausal filter with a low-pass cut-off frequency of 30 Hz and a high-pass cut-off frequency of 0.15 Hz (Zalachoris & Rathje, 2013). Using the processed recordings, Fourier amplitude spectra and response spectra are calculated, and the ratios of surface to input spectra are determined for EW and NS components, separately. The ratio of the surface to input Fourier spectra with frequency is the observed transfer function. The observed transfer functions are smoothed using a logarithmic triangular window with a width equal to one-fifth of a decade (Zalachoris & Rathje, 2013). The ratio of surface to input response spectra with period is the observed spectral amplification.

All KiK-net strong-motion recordings used for the purposes of this research were downloaded and processed by George Zalachoris, including calculations of observed Fourier amplitude spectra, observed response spectra, observed transfer functions, and observed spectral amplification.

3.4 SITE SELECTION

Of the approximate 700 KiK-net downhole array sites, 11 sites were selected as suitable for this study. Stiff soil sites were selected based on four criteria: average shear wave velocity over the 30 m (V_{s30}), number of available strong-motion recordings, depth to shear wave velocity of 1,000 m/s (Z_{1000}), and installation depth of base sensor (D_{base}).

3.4.1 Prerequisites

According to the 2014 International Building Code (IBC), the shear wave velocity of stiff soils (site class D) is classified as 180 to 360 m/s and the shear wave velocity of very dense soils and soft rock (site class C) is classified as 360 to 760 m/s. Because the goal of this study was to evaluate EQL site response analysis for stiff soil sites, only sites with V_{s30} between 400 and 700 m/s were considered.

Sites were selected based on the number of available strong-motion recordings. To date, some sites have fewer than 5 strong-motion recordings available, while other sites have greater than 100 strong-motion recordings available. For this study, we consider the median computed and observed transfer functions and spectral amplification for a given site. Increasing the number of motions provides a better representation of the median observations for a given site. Additionally, a larger number of motions potentially provides a larger range of input intensities. Therefore, sites were selected that have a large number of available recorded strong-motions and large peak ground accelerations at the base sensor. The number of available recorded strong-motions and peak ground accelerations at the base and surface sensor were determined from the published data.

According to the 2014 International Building Code (IBC), the shear wave velocity of rock (site class B) is classified as 760 to 1500 m/s. Z_{1000} is an indicator of the depth to bedrock. In the interest of comparing site response analysis over a range of depths to bedrock, sites were selected to vary Z_{1000} .

Site selection also considered D_{base} . To date, most sites have D_{base} between 100 and 200 m. Some sites have D_{base} less than 100 m and greater than 500 m. In the interest of comparing EQL site response analysis for varying site characteristics and depth to bedrock, sites were selected to vary D_{base} .

3.4.2 Final Sites Selected

Eleven sites were selected based on the criterion of having V_{s30} between 400 and 700 m/s, while maximizing the number of available recorded strong-motions and maximum peak ground accelerations at the base sensor, and providing a range of Z_{1000} and D_{base} . The final 11 sites selected are listed in Table 3.1 with their V_{s30} , number of available recordings used in analysis, Z_{1000} , and D_{base} . The V_{s30} values range from 429 to 670 m/s, and the Z_{1000} values range from 4 to 196 m. Figure 3.1 provides a map of Japan showing the locations of the final 11 sites selected. Of the 11 sites selected for this study, 7 are located in northeastern Japan, while the remaining 4 are located in central or southern Japan. Figure 3.2 provides the shear wave velocity profiles of the final 11 sites selected.

Table 3.1: Final sites selected including prerequisite criteria.

KiK-net Site Name	V_{s30} (m/s)	No. Recordings	Z_{1000} (m)	D_{base} (m)
FKSH09	585	92	10	200
IWTH04	456	74	49	106
IWTH05	429	124	37	100
IWTH21	521	134	20	100
IWTH24	486	62	196	150
IWTH25	506	116	64	260
IWTH27	670	124	4	100
MYGH06	593	26	86	100
NIGH09	463	42	80	100
NIGH12	553	80	136	110
SMNH01	464	56	22	101
Total	NA	930	NA	NA

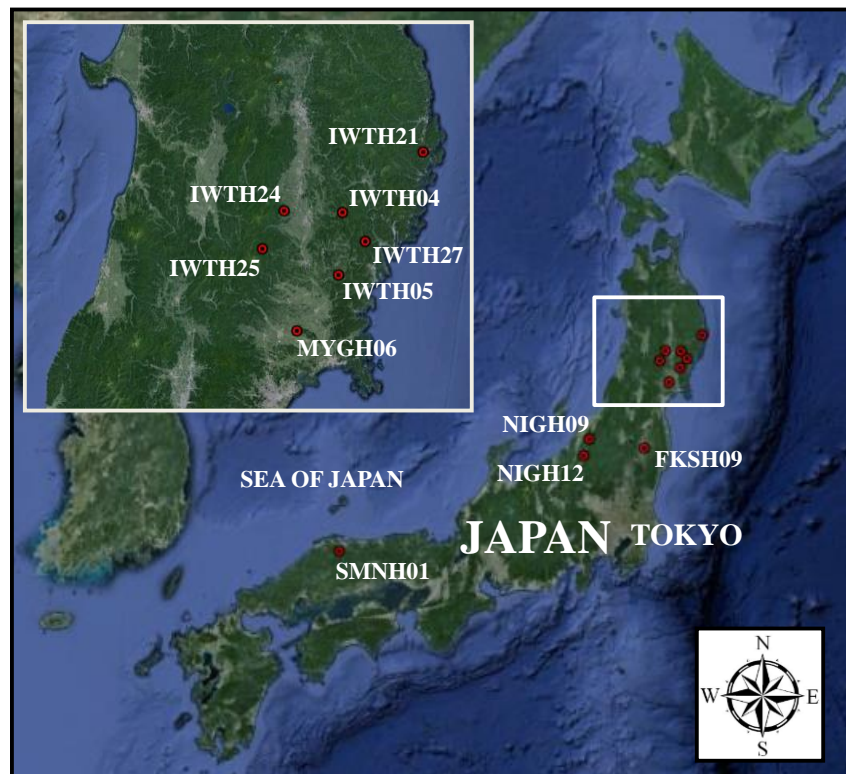


Figure 3.1: Map of Japan with location of final 11 sites selected.

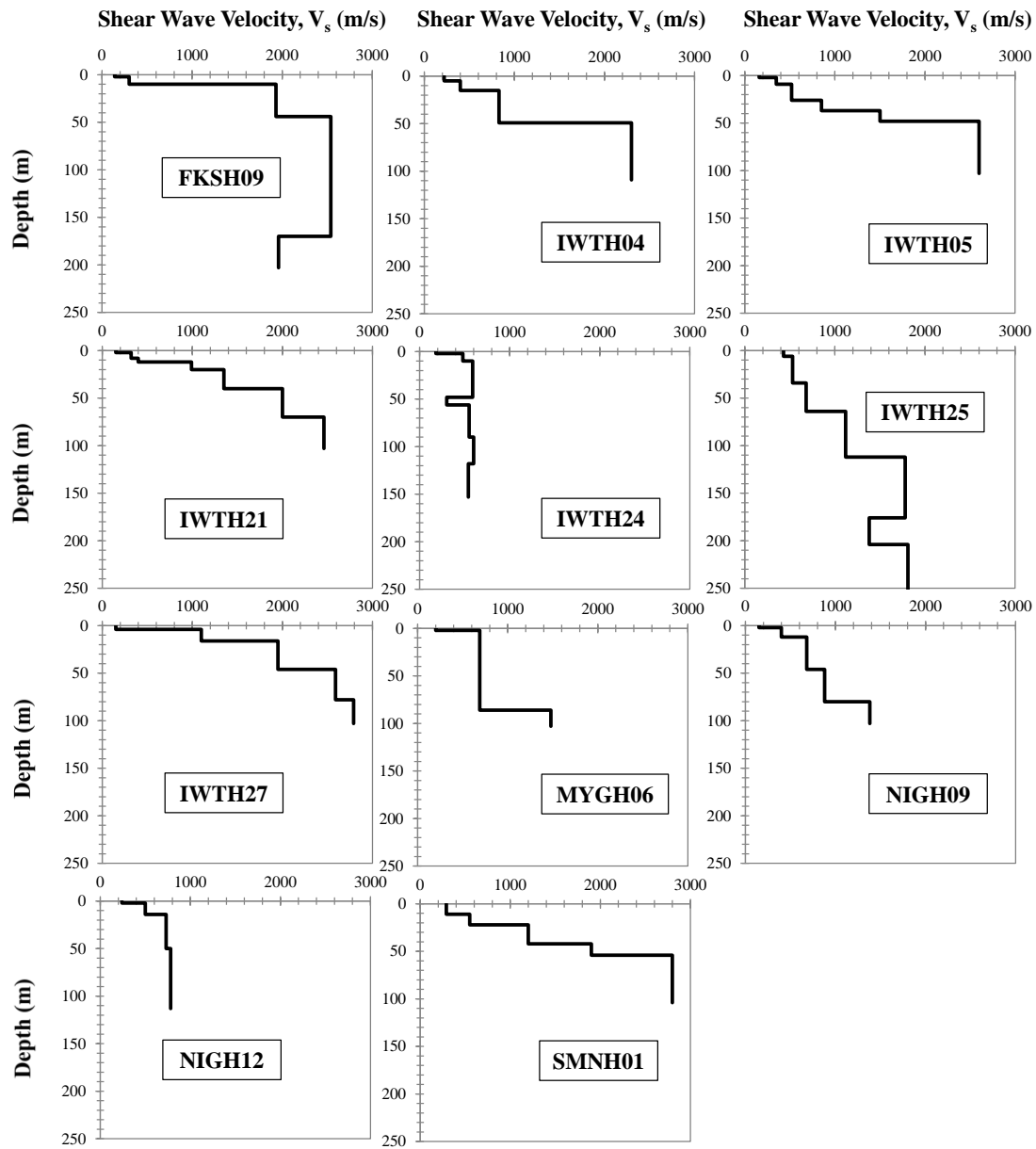


Figure 3.2: Shear wave velocity profiles of 11 sites selected.

The V_{s30} and Z_{1000} for the final 11 sites selected are plotted against each other in Figure 3.3. Of the 11 final sites selected, 6 have Z_{1000} less than 50 m, 3 have Z_{1000} between 50 and 100 m, and 2 have Z_{1000} greater than 100 m. The largest Z_{1000} is approximately 200 m. There is no strong relationship between V_{s30} and Z_{1000} for the sites selected, except that the largest Z_{1000} does have one of the smaller V_{s30} .

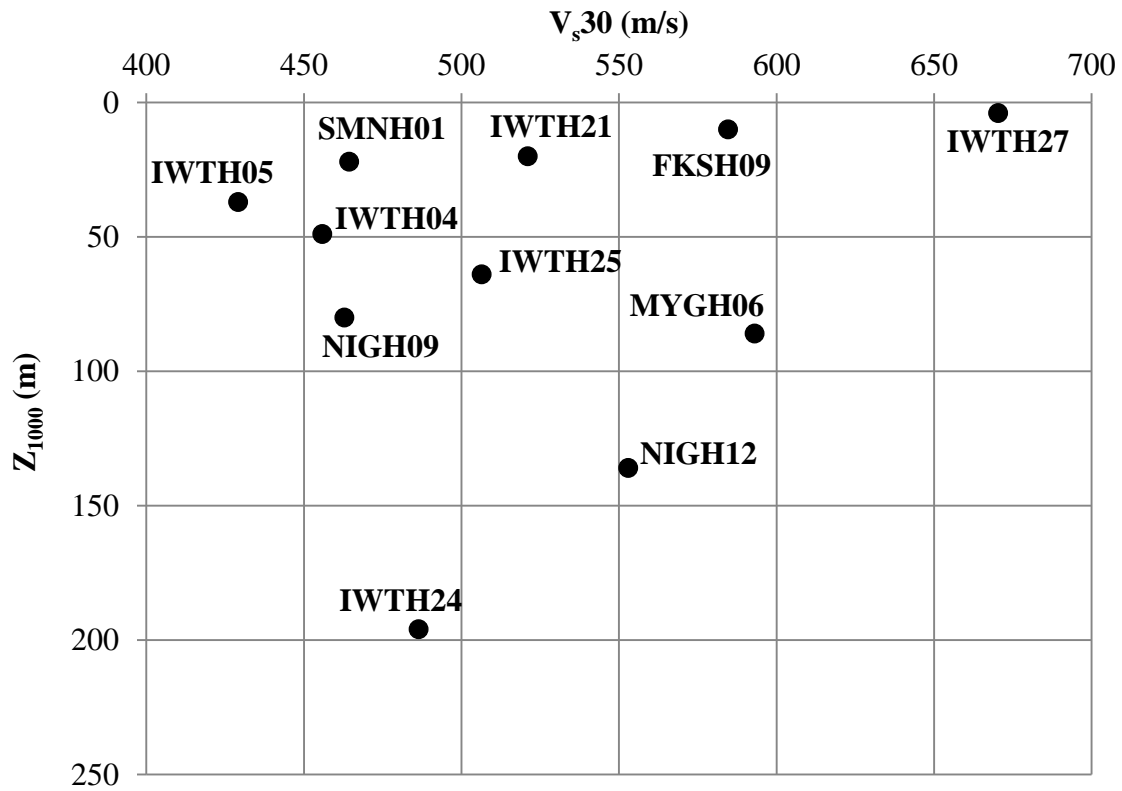


Figure 3.3: Z_{1000} and V_{s30} for final selected sites.

A comparison of D_{base} and V_{s30} for the final 11 sites selected is shown in Figure 3.4. Of the final 11 sites, 8 have D_{base} of approximately 100 m. The remaining 3 sites have D_{base} of approximately 150, 200, and 250 m. Of the 11 sites selected, 5 have V_{s30} between 400 and 500 m/s, 5 have V_{s30} between 500 and 600 m/s, and 1 has V_{s30} between 600 and 700 m/s.

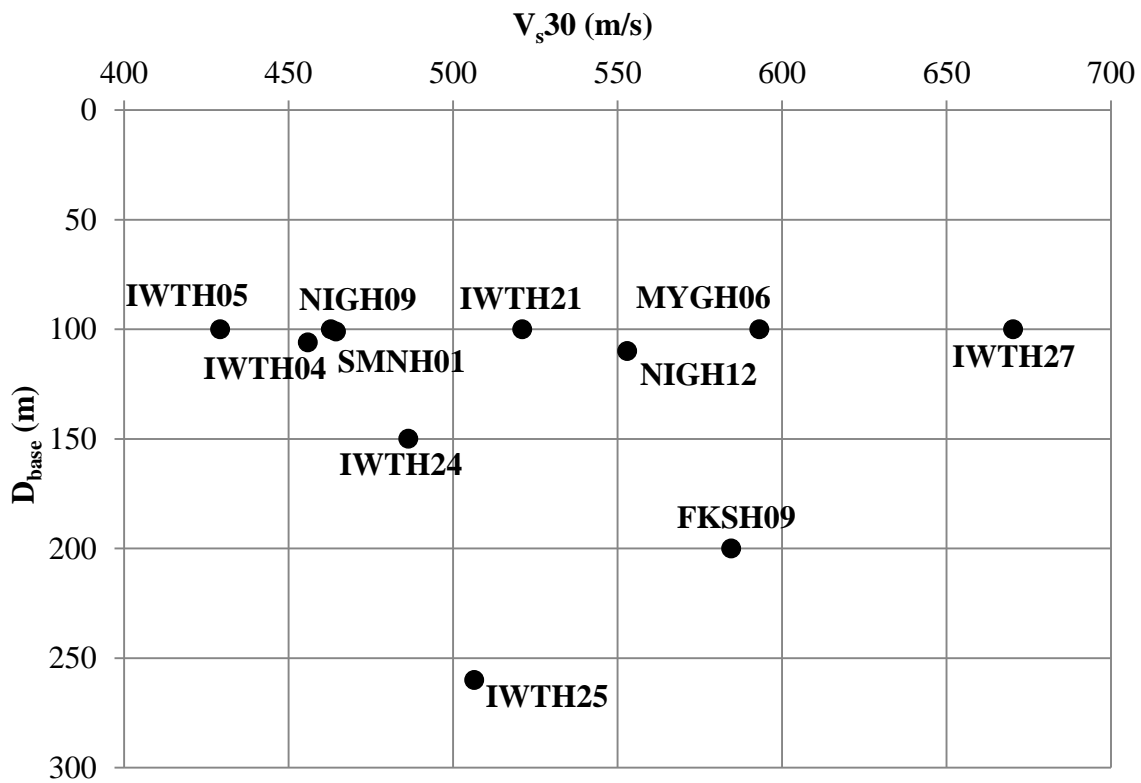


Figure 3.4: D_{base} and V_{s30} for final selected sites.

3.5 SITE CHARACTERIZATION

All EQL site response analyses presented in this research were performed using the program Strata (Kottke & Rathje, 2008) and the time series approach. The calculation parameters for the strain-compatible soil properties included a 2.0 percent error tolerance, a maximum of 10 iterations, and an effective strain ratio of 0.65. The layer discretization was defined using a maximum frequency of 100 Hz and a wavelength fraction of 0.10.

Sites were characterized using published and estimated soil properties. Shear wave velocities and soil layer thicknesses were defined using the published V_s profiles. The unit weight of all soil layers, including the bedrock layer, was assumed to be 19 kN/m³. The ground water table was assumed to be at a depth of 5 m at all sites.

Modulus reduction and damping curves were specified using Darendeli and Stokoe (2001) for layers with V_s less than 800 m/s. The Schnabel (1973) rock curves were specified for layers with V_s greater than 800 m/s. The Darendeli and Stokoe (2001) model for modulus reduction and damping is dependent on confining pressure and plasticity index. Assumed Darendeli and Stokoe (2001) model parameters include a minimum mean effective confining pressure of 0.25 atm, an overconsolidation ratio of 1.0, and a plasticity index of 15. An excitation frequency of 1.0 Hz and 10 cycles were also assumed. Figure 3.5 shows examples of the modulus reduction and damping curves used. The Darendeli and Stokoe (2001) curves are shown for the range of confining pressures represented by the sites. The Darendeli and Stokoe (2001) curves in Figure 3.5 show less modulus reduction and smaller damping as confining pressure increases, and the rock curves show even less modulus reduction and smaller damping. The bedrock layer was modelled using 0.40% damping and assumed to extend infinitely in depth.

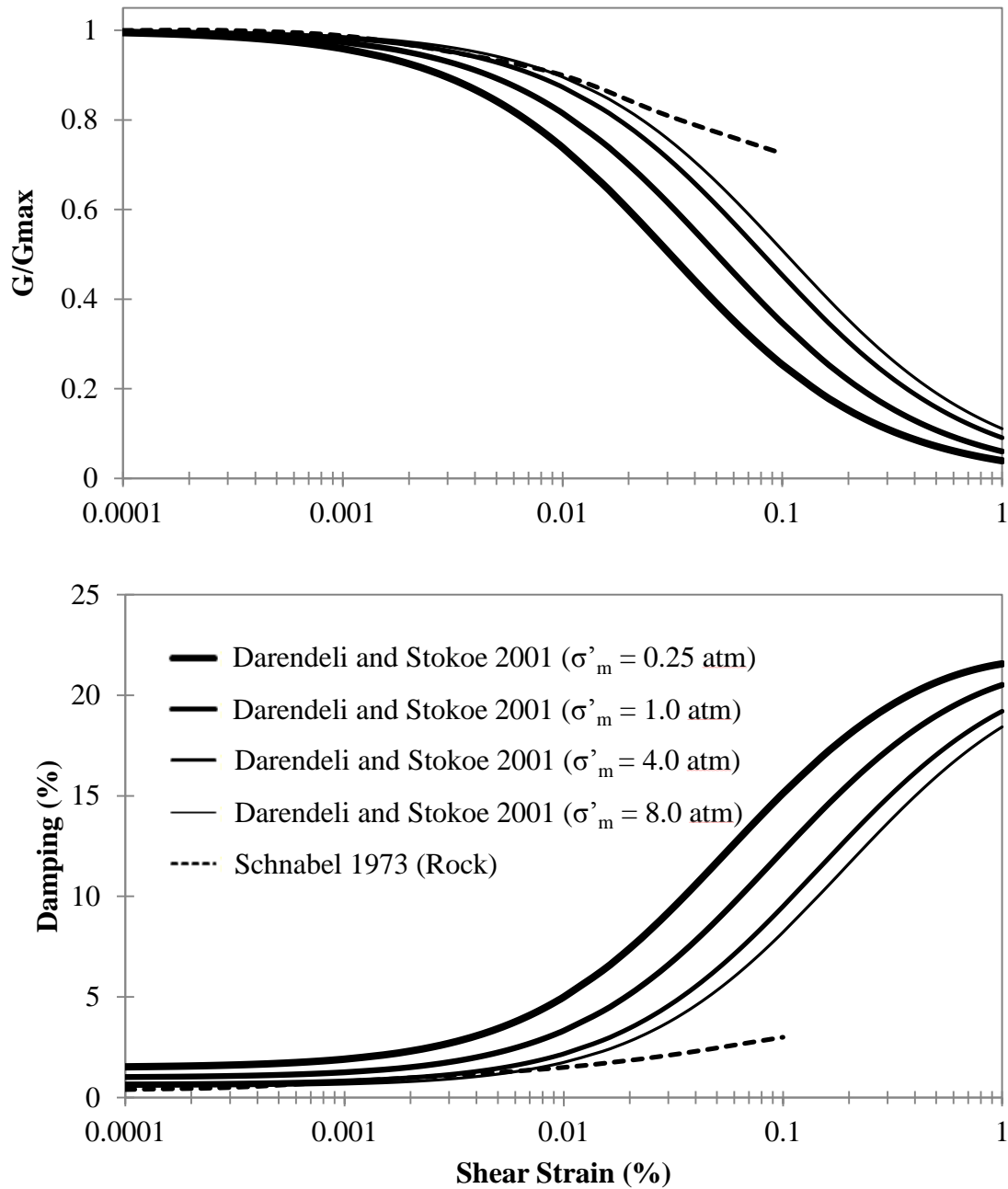


Figure 3.5: Example Darendeli and Stokoe (2001) modulus reduction and damping curves at mean effective stresses of 0.25, 1.0, 4.0, and 8.0 atm, and Schnabel (1973) rock modulus reduction and damping curves.

3.6 SUMMARY

KiK-net is a strong-motion seismograph network in Japan consisting of approximately 700 downhole array sites with high sensitivity seismographs containing strong-motion accelerometers located at the ground surface and at depth. Observed transfer functions and spectral acceleration can be determined and compared against computed transfer functions and spectral acceleration from EQL site response analysis. A total of 11 sites were determined to be suitable for this research based on the following criteria: average shear wave velocity over the top 30 m, number of available strong-motion recordings, depth to shear wave velocity of 1,000 m/s, and installation depth of base sensor. Sites were characterized using published and estimated soil properties, and using the Darendeli and Stokoe (2001) and Schnabel (1973) rock curves for modulus reduction and damping.

Chapter 4: Comparison of Computed and Observed Site Response

4.1 INTRODUCTION

This chapter discusses comparison of the computed and observed site response for the 11 KiK-net sites selected for this study. The site response comparisons are first demonstrated using a single KiK-net site that is representative of the overall findings. For the 11 sites, the median computed and observed transfer functions and response spectral amplification are presented and compared for low intensity and large intensity earthquake shaking. The aggregated results from the 11 sites are presented and discussed.

4.2 EXAMPLE OF SITE RESPONSE COMPARISON

Observed transfer functions and response spectral amplification were determined at 11 KiK-net downhole array sites for 930 individual seismic recordings. Transfer functions and response spectral amplification were calculated by specifying the KiK-net base sensor motion as the input motion, and computing the surface motion using EQL site response analysis. This section describes the site response results for site IWTH27, which is representative of the overall findings. The shear wave velocity profile for site IWTH27 is shown in Figure 4.1.

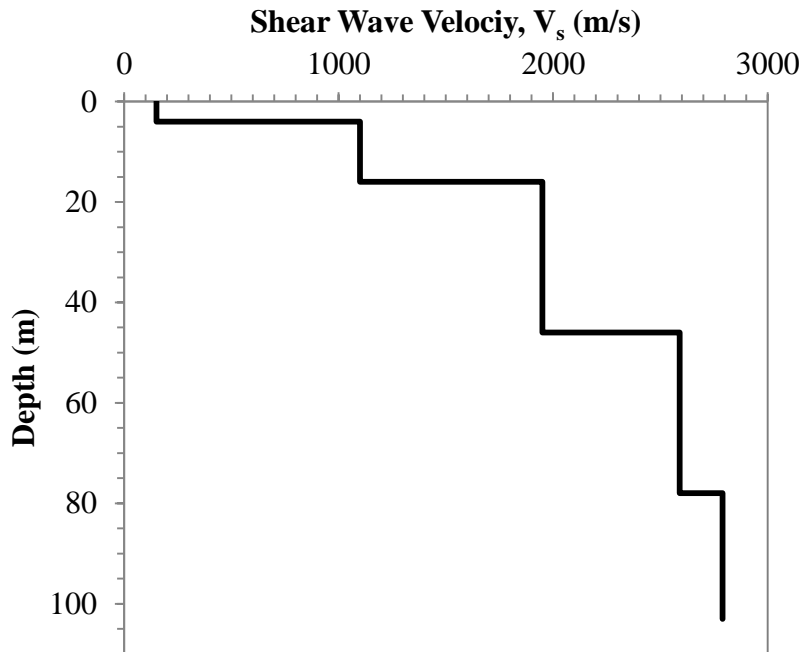


Figure 4.1: Shear wave velocity profile for site IWTH27.

The dynamic response of a soil deposit depends on the intensity of earthquake shaking due to the nonlinear stress-strain response of the soil. The peak ground acceleration of the base sensor motion (PGA_{base}) may be used as a measure of the intensity of earthquake shaking. While the PGA_{base} is related to the level of nonlinearity induced in a soil deposit, it is not a direct measure of the shear strain induced in the soil. Additionally, different sites will experience different levels of strain for the same PGA_{base} due to differences in shear wave velocities. The shear strain calculated by EQL site response analysis provides a direct indication of the nonlinearity induced in the soil, but it is a computed quantity and its accuracy will depend on the accuracy of the numerical model. Nonetheless, the maximum shear strain is used as the indicator of nonlinearity for the analyses performed in this study.

Figure 4.2 shows the calculated peak shear strain as a function of depth for three input motions that vary in intensity (i.e., PGA_{base} of 0.01, 0.04, and 0.12 g) for site IWTH27. The maximum shear strain is defined as the largest peak shear strain within the soil column and it often occurs near the surface in the softest layers. From Figure 4.2, the maximum shear strain occurs at a depth of approximately 3 m for all three motions. This depth corresponds with the surface layer that has a shear wave velocity of 150 m/s (Figure 4.1). The maximum shear strain varies from approximately 0.005% to 0.3% across the three motions, with the strain increasing with increasing PGA_{base} .

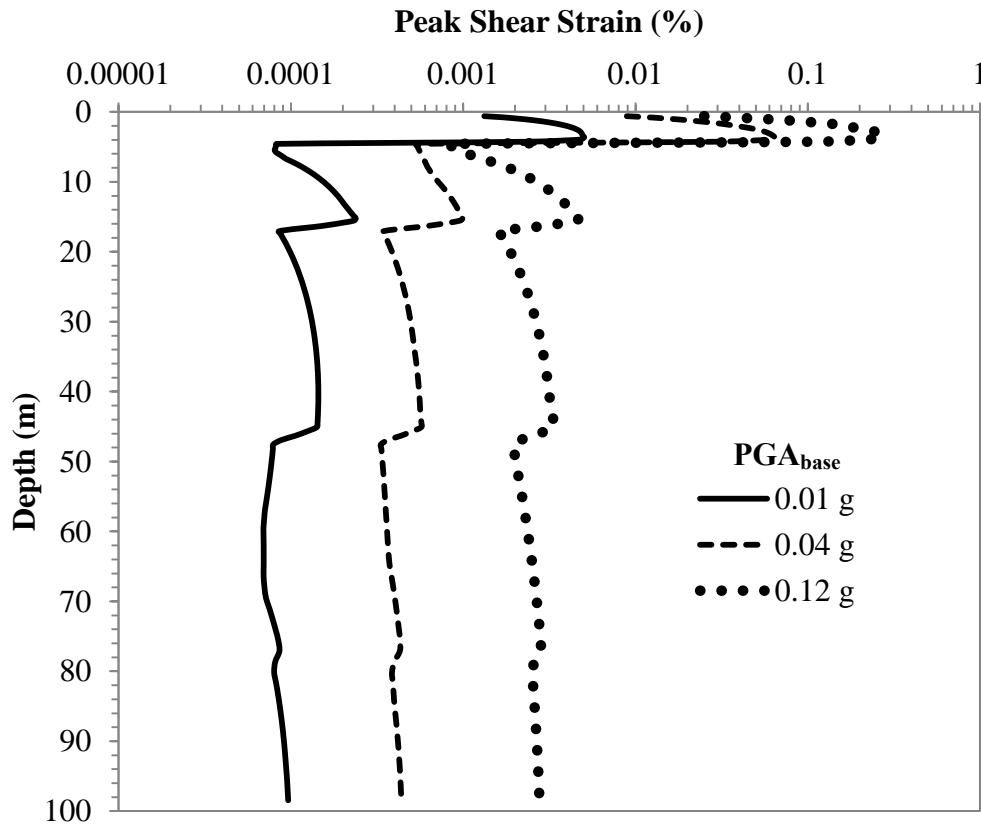


Figure 4.2: Computed peak shear strain with depth for three input motions of varying PGA_{base} for site IWTH27.

Figure 4.3 compares the calculated maximum shear strain and the corresponding observed PGA_{base} for all of the KiK-net recordings used in this study across the 11 sites. The relationship between the calculated maximum shear strain and the observed PGA_{base} is approximately proportional. However, for a given PGA_{base} the computed maximum shear strain can vary by more than an order of magnitude owing to differences in the shear wave velocity profiles across the sites. Therefore, the computed maximum shear strain is used as the measure of induced soil nonlinearity.

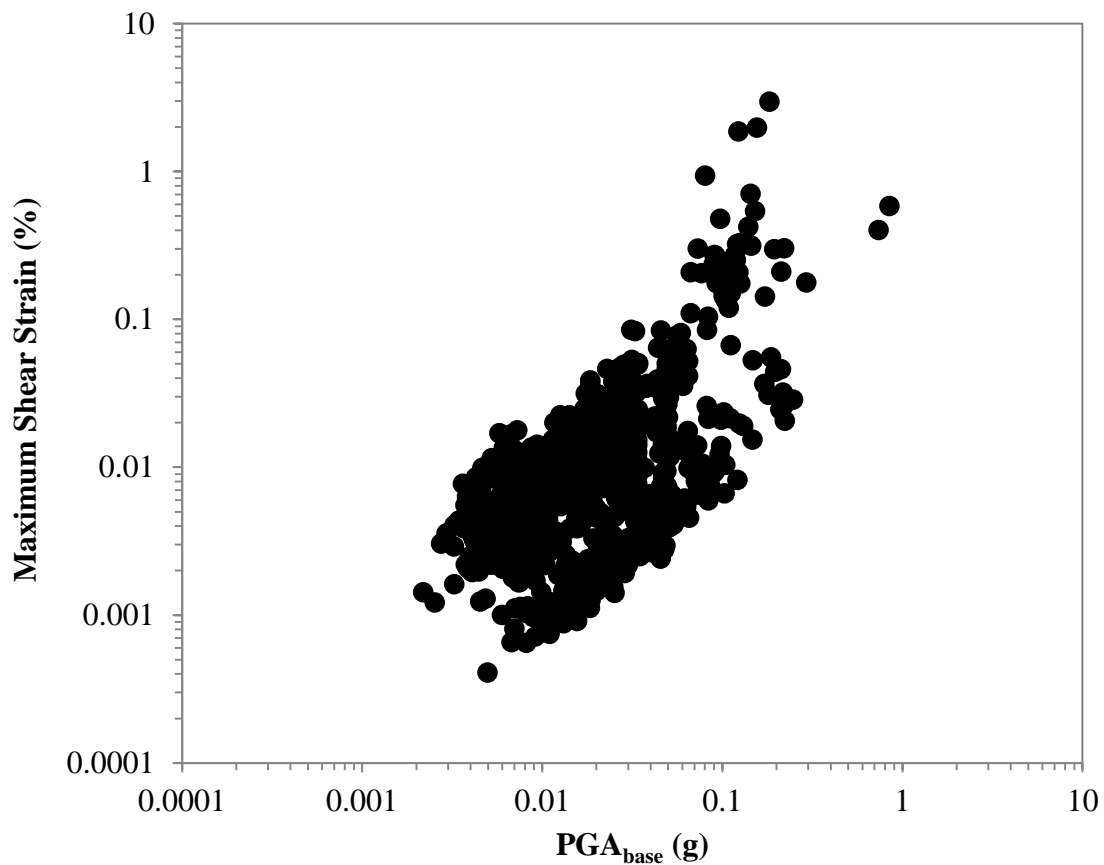


Figure 4.3: Comparison of calculated maximum shear strain from EQL site response analysis and corresponding observed PGA_{base} for 930 KiK-net recordings.

To compare similar levels of nonlinearity across different motions and sites, the computed and observed site response were compared relative to four bins of shear strain representing half-log cycles. Table 4.1 shows the four strain bins and Figure 4.4 shows the strain bins relative to example modulus reduction and damping curves. The smallest strain bin extends from very small strains (i.e., 0.0001%), where the response is essentially linear, to 0.01%, where the response starts to become more nonlinear. The remaining strain bins capture the strains over which the changes in stiffness and damping are significant.

Table 4.1: Strain bins for site response comparison.

Bin	Calculated Maximum Shear Strain (%)
1	< 0.01
2	0.01 – 0.03
3	0.03 – 0.1
4	> 0.1

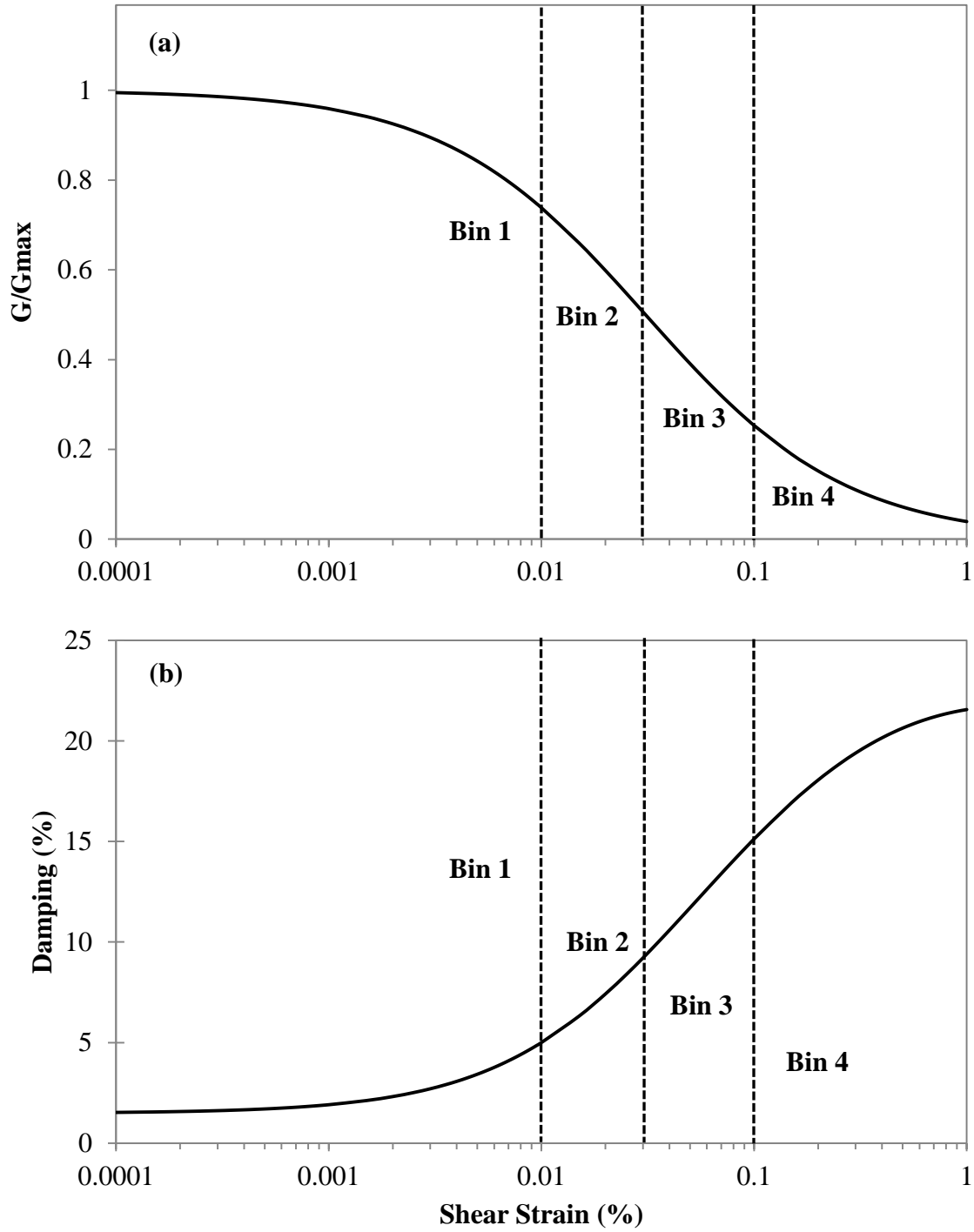


Figure 4.4: Strain bins for site response comparison relative to example (a) modulus reduction curve and (b) damping curve.

Table 4.2 provides a summary of the input shear wave velocity layering for site IWTH27, along with the estimated mean effective stress (σ'_m) at the center of each layer. The unit weight, plasticity index, OCR, and depth to ground water table were assumed to be 19 kN/m³, 15, 1, and 5 m, respectively. Summaries of the input shear wave velocity layering and σ'_m for all sites is provided in Appendix B. The Darendeli and Stokoe (2001) model for modulus reduction and damping was used for layer 1, and the Schnabel (1973) model for modulus reduction and damping for rock was used for layers 2 through 5 because of the large shear wave velocities associated with these layers. An elastic half-space was assumed below 100 m with a damping ratio of 0.4%.

A total of 124 seismic records (62 individual seismic events composed of East-West (EW) and North-South (NS) components) were used for the site response comparison for site IWTH27 and analyzed independently. The number of recordings corresponding to each strain bin is summarized in Table 4.3.

Table 4.2: Site IWTH27 layer discretization for EQL site response analysis.

Layer No.	Thickness (m)	Depth (m)	V_s (m/s)	σ'_m (atm)
1	4	4	150	0.25
2	12	16	1100	0.93
3	30	46	1950	2.20
4	32	78	2590	4.07
5	22	100	2790	5.70

Table 4.3: Number of recordings assigned to strain bins for site IWTH27.

Bin	Calculated Maximum Shear Strain (%)	No. Recordings
1	< 0.01	57
2	0.01 – 0.03	48
3	0.03 – 0.1	12
4	> 0.1	7
Total		124

The median computed and observed transfer functions and response spectral amplification were determined for each strain bin. Transfer functions are compared for frequencies between 0.5 and 20 Hz and spectral amplification is compared for periods between 0.05 and 2 s. Periods greater than 2 s were not considered because surface waves can influence the observed site response at longer periods which cannot be modelled in one-dimensional site response analysis.

The median computed, median observed, and individual observed transfer functions for site IWTH27 are shown in Figure 4.5. The largest peak in the transfer function occurs at the fundamental frequency of the soil deposit. The observed fundamental frequency for site IWTH27 is approximately 7.5 Hz and corresponds predominantly with the response of the soft surface layer. There is good agreement between the computed and observed fundamental frequency for site IWTH27. However, the computed transfer function predicts a larger response at the fundamental frequency than the observed transfer function, most significantly at smaller strains. The larger computed response is due to the “within” boundary condition assumed at the base of the downhole array, which models fully the destructive interference of the upward and downward waves. However, this destructive interference may not fully materialize in situ due to refraction, wave scattering, and/or material damping, and therefore the observed transfer function at the fundamental frequency may be smaller than computed.

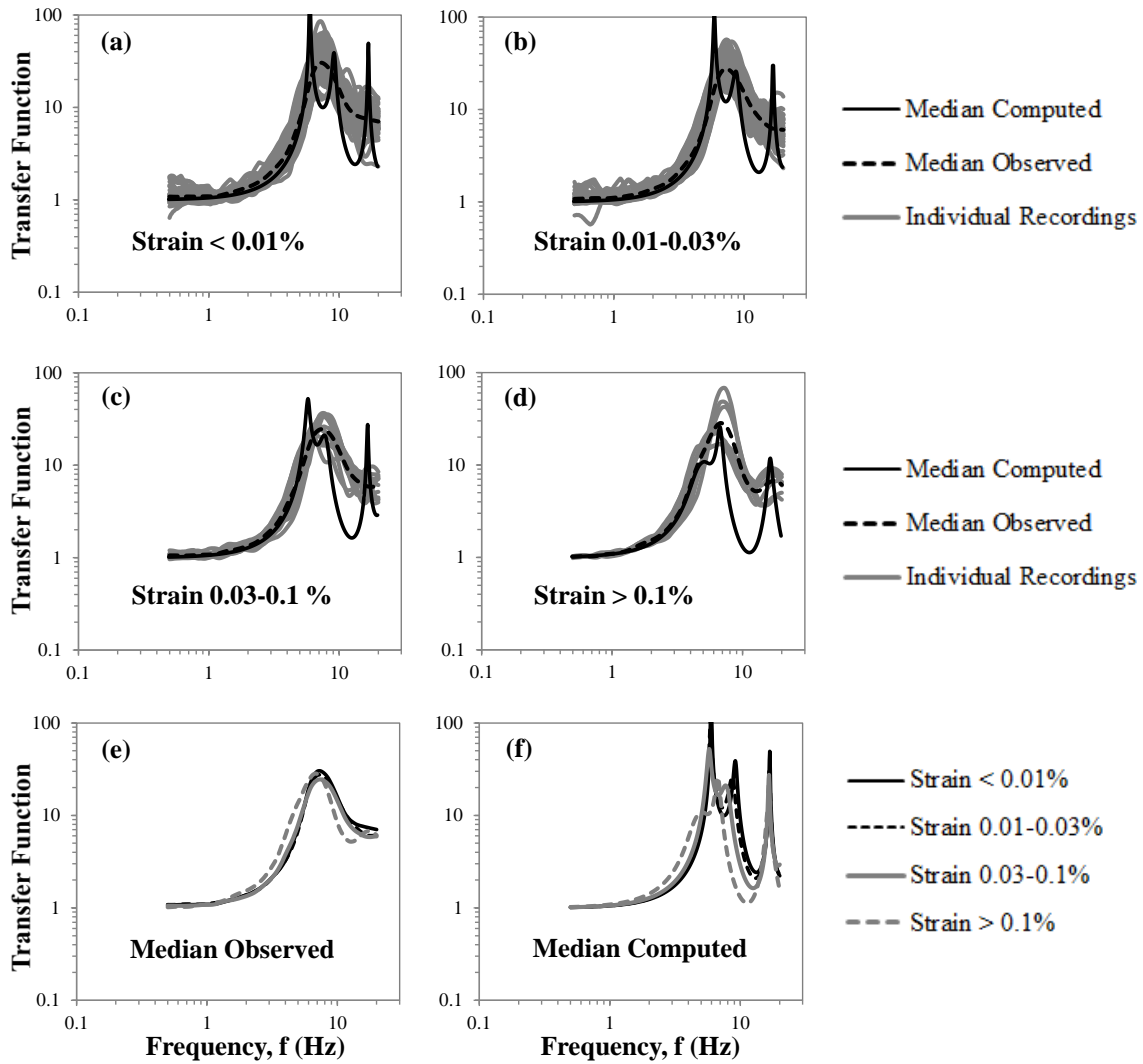


Figure 4.5: Computed and observed transfer functions for site IWTH27.

There is good agreement between the computed and observed transfer functions for frequencies below the fundamental frequency across all four strain bins. There is less agreement for frequencies greater than the fundamental frequency. Specifically, the computed transfer functions show additional peaks associated with high modes of response and these modes are not observed in the recordings from site IWTH27.

Figure 4.5(e) shows the median observed transfer functions for the four strain bins. There is little variation in the observed transfer functions for strain bins 1 through 3, while the observed transfer function for strain bin 4 is slightly shifted towards lower frequencies due to some soil nonlinearity. Figure 4.5(f) shows the median computed transfer functions for the four strain bins. The computed transfer functions show larger differences among the strain bins. The modal frequencies shift towards lower frequencies with increasing shear strain and the peaks are significantly diminished. These changes are due to a reduction in shear modulus and an increase in damping at larger strains.

The median computed, median observed, and individual observed response spectral amplification for site IWTH27 are shown in Figure 4.6. The largest spectral amplification occurs at the period associated with the fundamental mode of the site (i.e., the site period). There is good agreement between the computed and observed site period of site IWTH27. While the computed spectral amplification at the site period is greater than the observed spectral amplification, the difference is not as large as it was for the transfer function. There is good agreement between the computed and observed spectral amplification for periods greater than the site period across all four strain bins. There is less agreement for periods less than the site period due to higher modes being more apparent in the computed values. Similar to the transfer functions, the spectral amplification decreases and shifts towards longer periods with increasing shear strain due to soil nonlinearity.

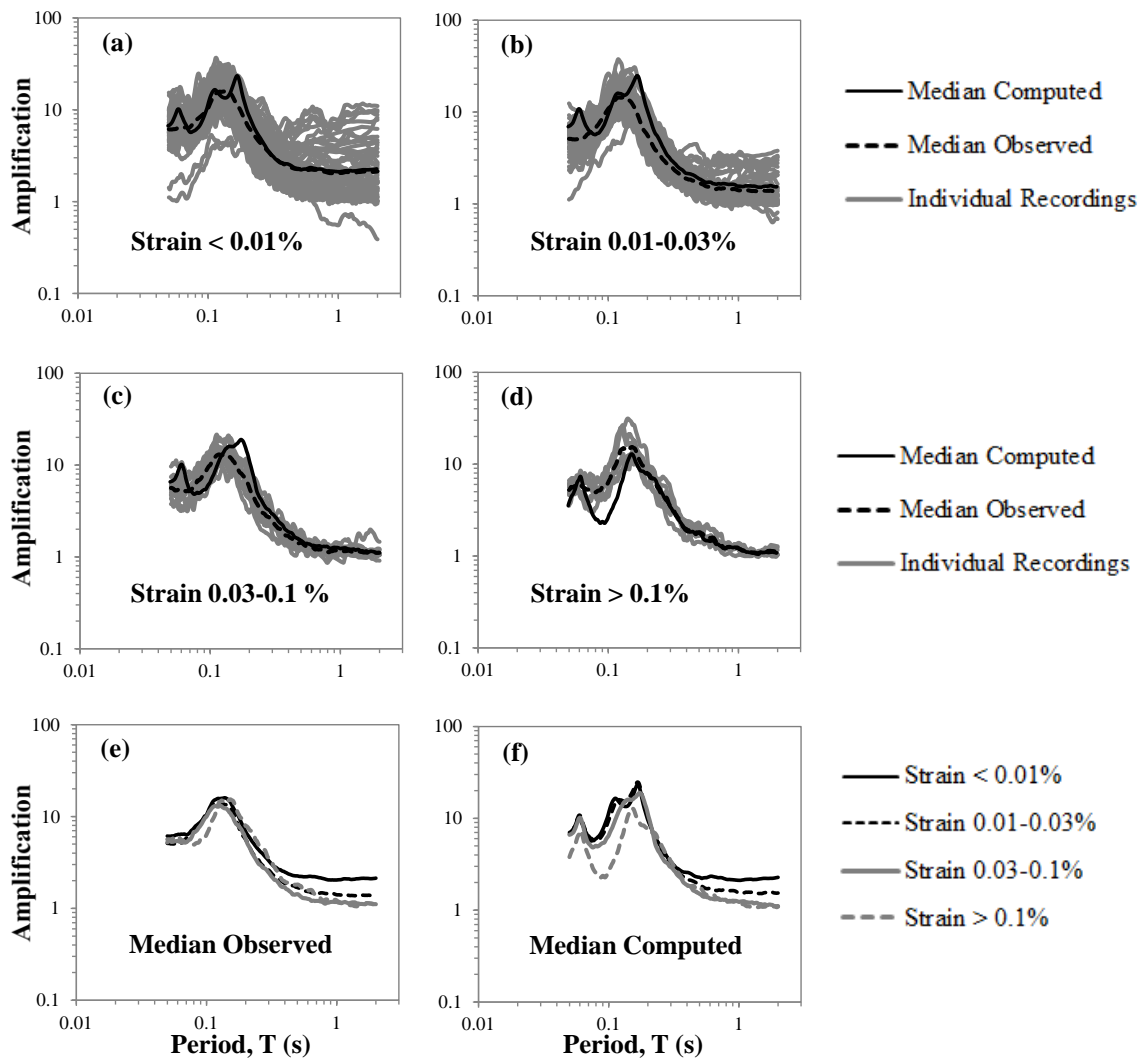


Figure 4.6: Computed and observed response spectral amplification for site IWTH27.

To quantify the difference between the computed and observed response spectral amplification, the residual is used. The residual is a measure of the difference between the observed and computed response spectral amplification at a given period. The residual at period T is defined as,

$$\text{Residual}(T) = \ln(\text{AF}_{\text{Observed}}(T)) - \ln(\text{AF}_{\text{Computed}}(T)) \quad (4.1)$$

where $\text{AF}_{\text{Observed}}(T)$ is the observed spectral amplification at period T and $\text{AF}_{\text{Computed}}(T)$ is the computed spectral amplification at period T from EQL site response analysis. Because the residual is defined in terms of natural log, negative residuals occur when the computed amplification is greater than the observed amplification (i.e., over-prediction). Positive residuals occur when the computed amplification is less than the observed amplification (i.e., under-prediction). A residual of zero indicates exact agreement between the computed and observed amplification values. The residual offers a way to easily visualize the over- or under-prediction of the amplification for a range of periods and at different levels of shear strain.

The average residuals for site IWTH27 are plotted versus period in Figure 4.7(a) for the four strain bins. There is over-prediction in the site amplification at the computed site period ($T_{\text{SITE}} \sim 0.17$ s) and at higher modes ($T \sim 0.06$ s), except for the largest strain bin. The over-prediction increases from strains less than 0.01% to strains between 0.01 – 0.03%, but then decreases with increasing shear strain levels. There is under-prediction in the site amplification at periods between the site period and the next higher mode, with more under-prediction occurring with increasing shear strain levels. There is good agreement between the computed and observed amplification at periods greater than the site period for all four strain bins.

The period at which the residual is plotted can also be normalized by the site period (T_{SITE}). This normalization is convenient for comparing multiple sites as it relates all sites to a common reference and it offers a way for engineers to easily visualize the over- or under-prediction of the amplification at the site period and at periods less than the site period. Figure 4.7(b) shows the average residuals for site IWTH27 plotted versus T/T_{SITE} for the four strain bins. There is over-prediction at the site period ($T/T_{\text{SITE}} \sim 1$), except for strain of 0.1% or greater. There is good agreement between the observed and computed amplification at periods greater than the site period ($T/T_{\text{SITE}} > 1$) for all four strain bins.

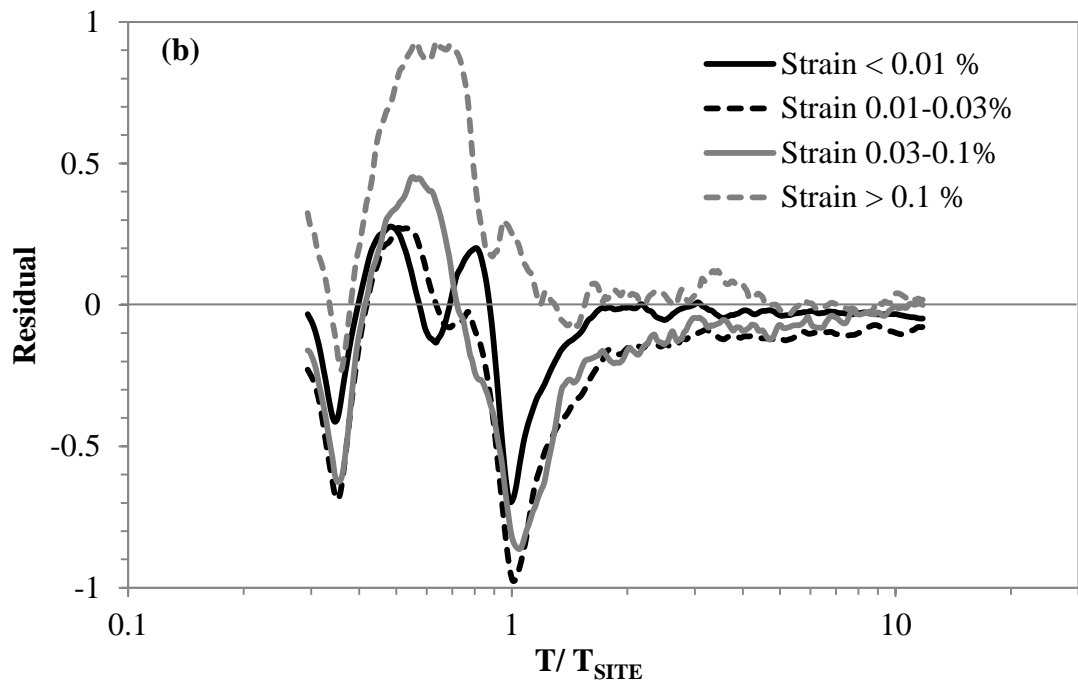
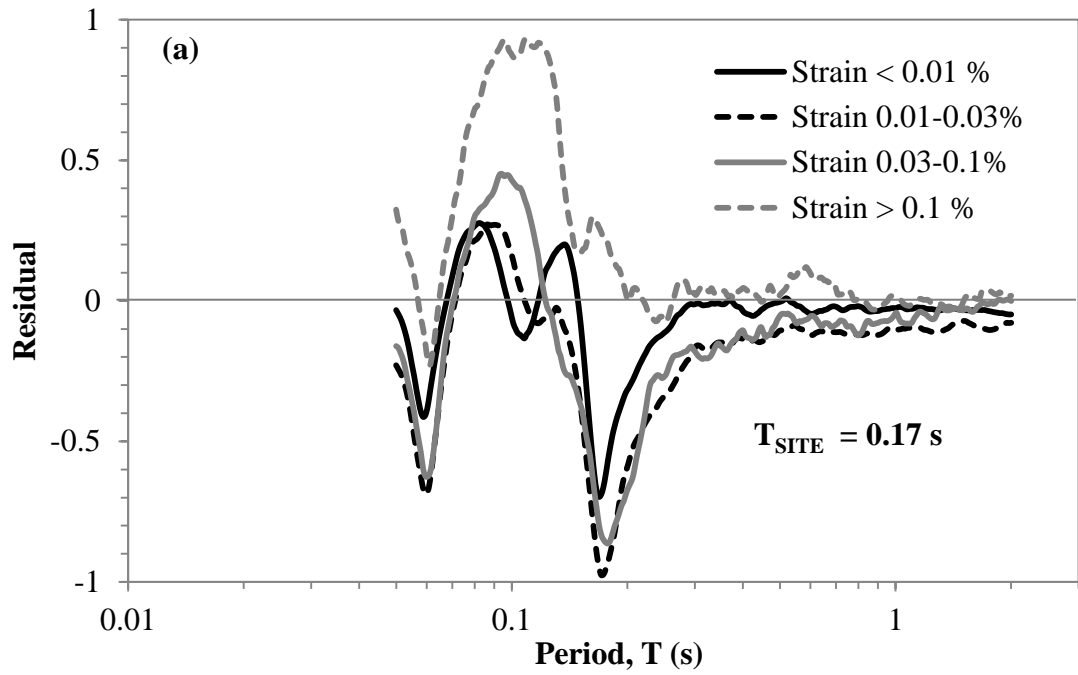


Figure 4.7: (a) Average residuals plotted versus period T and (b) average residuals plotted versus T/T_{SITE} for site IWTH27 and all four strain bins.

4.3 LOW INTENSITY SHAKING

To investigate the accuracy of the site response results across all sites for different levels of nonlinearity, comparisons are made separately for low intensity shaking and high intensity shaking. Low intensity shaking is defined as having a maximum shear strain less than 0.01%, while large intensity shaking is defined as having a maximum shear strain of 0.01% or greater. This section focuses on low intensity shaking where the response is close to linear-elastic.

The total number of motions per site and the number of motions corresponding to each strain bin per site are listed in Table 4.4. This table shows that all sites contribute to the small strain bin (i.e., less than 0.01%), although some sites contribute more than others (102 motions for IWTH25 and 13 motions for MYGH06). A similar distribution is found for strains between 0.01 - 0.03%, although the absolute number of motions is smaller and the sites with the largest numbers of motions are different. At the largest strains, some of the sites do not contribute at all because motions strong enough to induce large strains did not occur.

Table 4.4: Total number of KiK-net recordings per site and corresponding strain bins.

KiK-net Site Name	Number of KiK-net Recordings				Total
	Strain < 0.01%	Strain 0.01-0.03%	Strain 0.03-0.1%	Strain > 0.1%	
FKSH09	56	28	6	2	92
IWTH04	37	28	3	6	74
IWTH05	86	24	8	6	124
IWTH21	88	34	4	8	134
IWTH24	31	13	11	7	62
IWTH25	102	12	0	2	116
IWTH27	57	48	12	7	124
MYGH06	13	9	4	0	26
NIGH09	18	13	8	3	42
NIGH12	70	8	2	0	80
SMNH01	48	5	1	2	56
Total	606	222	59	43	930

The computed and observed transfer functions for low intensity motions with maximum shear strain levels less than 0.01% at the 11 sites are provided in Figure 4.8. Overall, there is mostly good agreement between the computed and observed transfer functions for these low intensity motions. There is generally good agreement between the computed and observed fundamental frequencies for the sites, although the amplitudes are quite different. The computed fundamental frequency is slightly less than the observed fundamental frequency for sites FKSH09, IWTH24, and IWTH27, while it is slightly greater than the observed fundamental frequency for MYGH06 and NIGH09. For site SMNH01 the observed peak in the transfer function is very broad (from about 5 – 15 Hz), while the computed transfer function displays multiple, narrow peaks over this frequency range. The larger peaks in the computed transfer functions at the fundamental frequencies are due to the “within” boundary condition assumption incorporated in the analysis.

There is very good agreement between the computed and observed transfer functions at frequencies below the fundamental frequencies. There is less agreement between the computed and observed transfer functions at frequencies greater than the fundamental frequency. The troughs in the computed transfer functions are much lower than those in the observed transfer functions across all sites. However, there is mostly good agreement between the computed and observed higher modes of response, except for FKSH09 and NIGH09. Sites IWTH04, IWTH24, IWTH25, MYGH06, NIGH09, and NIGH12 predict multiple higher modes, some of which were not observed at those sites.

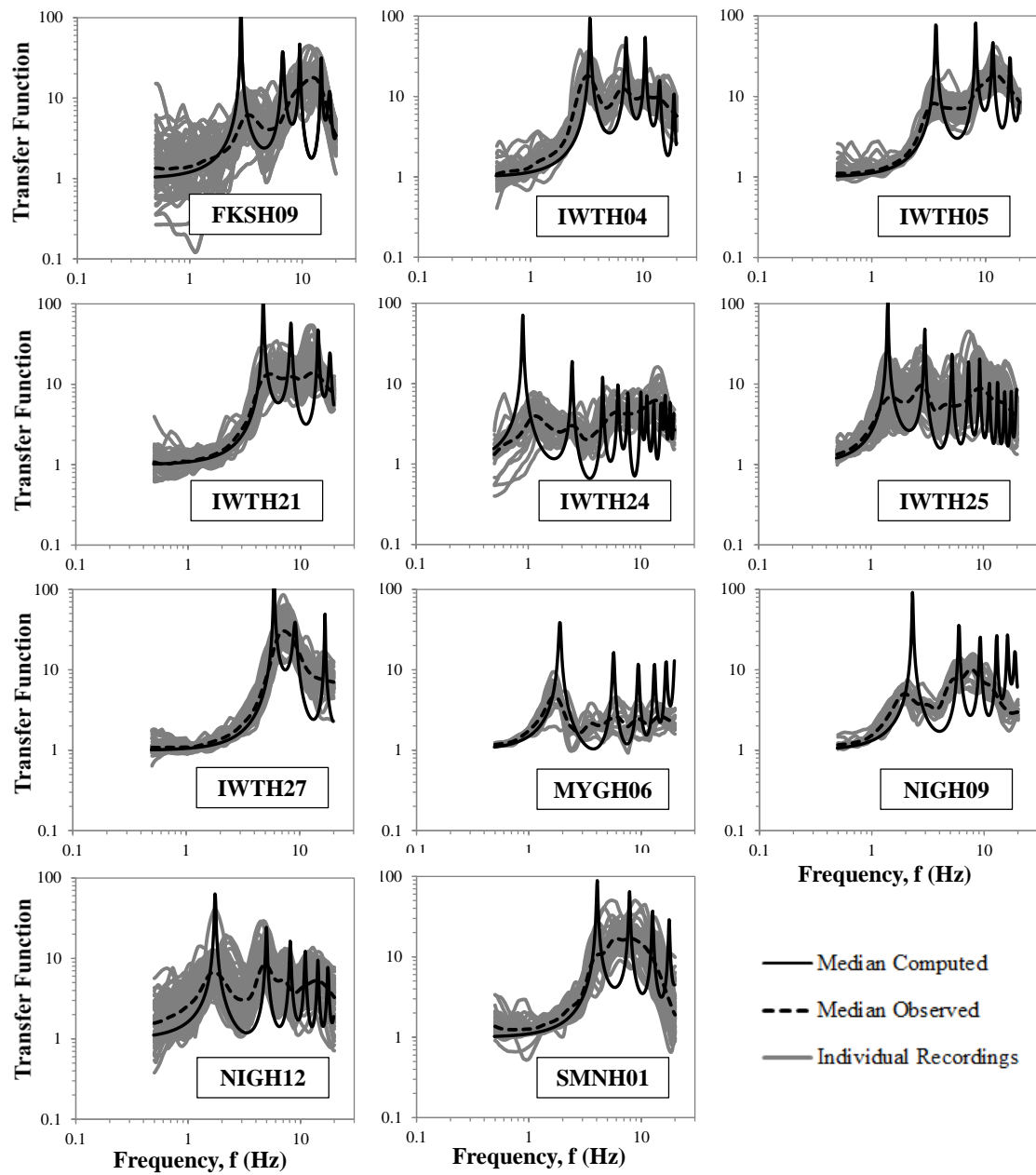


Figure 4.8: Transfer functions for low intensity shaking with calculated maximum shear strains less than 0.01%.

The computed and observed response spectral amplification for low intensity motions with maximum shear strain levels less than 0.01% at the 11 sites are provided in Figure 4.9. Similar to the transfer functions, there is generally good agreement between the computed and observed amplification for these low intensity motions. There is mostly good agreement between the computed and observed site periods for the sites, although in some cases the computed site period may be slightly smaller and larger than observed. The computed spectral amplification at these peaks tends to be larger than observed, due to the assumed “within” boundary condition as discussed earlier for the transfer functions. However, the over-prediction is not as large for response spectral amplification as it was for the transfer functions.

There is mostly good agreement between the computed and observed spectral amplification at periods larger than the site period. Sites FKSH09 and IWTH24 noticeably over-predict the amplification at these longer periods. Site IWTH24 has a site period of about 1 s and the over-predicted response around the site period (Figure 4.9) is influencing the site amplification at periods from 1 to 2 s. The over-prediction for FKSH09 is surprising because the transfer functions matched well in the corresponding frequency range (Figure 4.8). Sites IWTH05, IWTH21, and MYGH06 slightly over-predict the amplification at periods above the site period.

There is less agreement between the computed and observed spectral amplification for periods less than the site period. Specifically, there is over-prediction of the response at sites IWTH04, IWTH21, MYGH06, and NIGH09, and under-prediction of the response at site IWTH25. This is likely due to the inaccurate shear wave velocities and layer thicknesses of the upper layers, which often control the amplification at shorter periods.

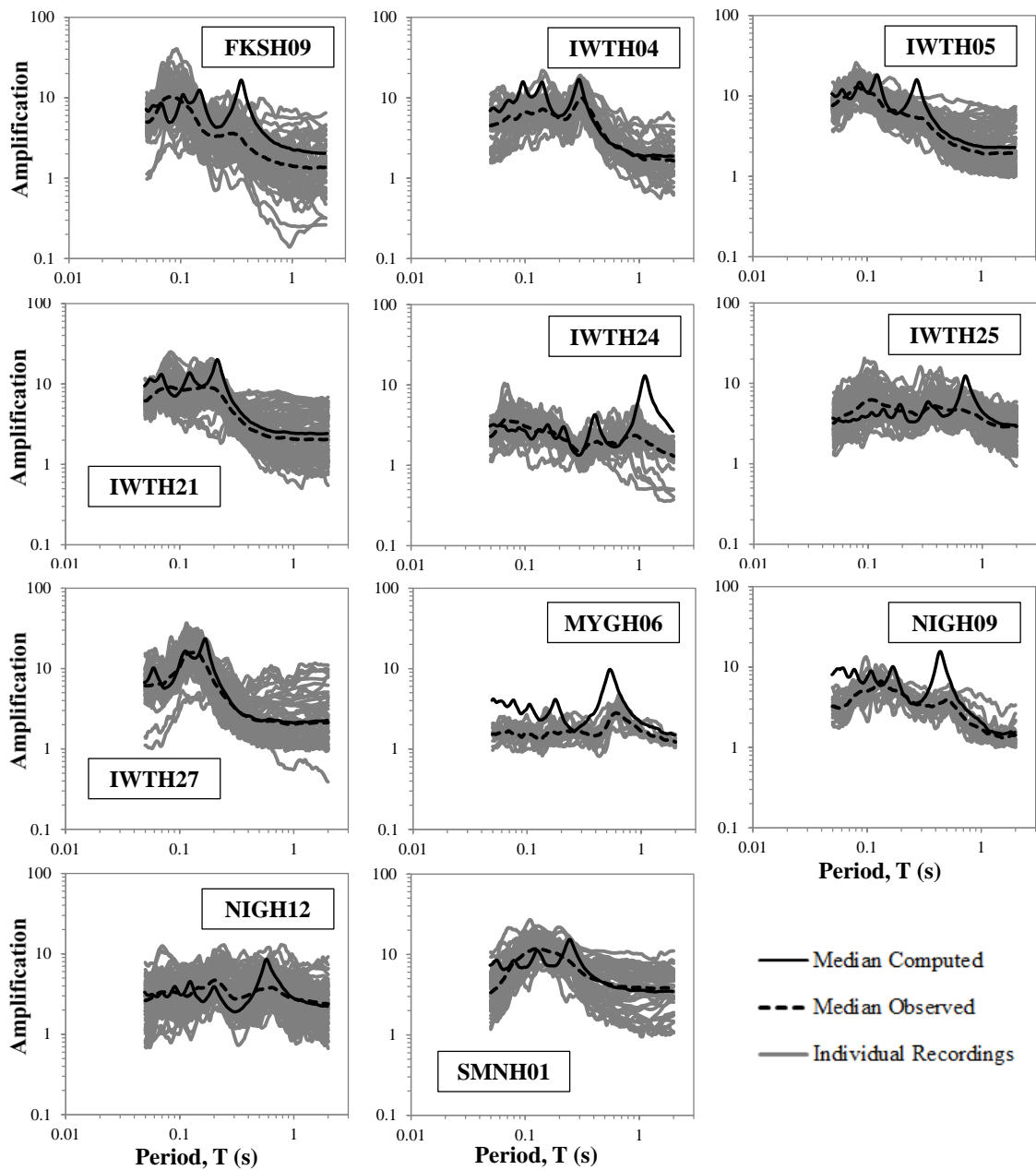


Figure 4.9: Spectral amplification for low intensity shaking with calculated maximum shear strains less than 0.01%.

As an example, the shear wave velocity profile for site IWTH04 was adjusted and the computed response spectral amplification was calculated. The reported and adjusted shear wave velocity profiles are provided in Table 4.5. Specifically, the shear wave velocities for layers 1 and 2 were adjusted from the reported 220 and 400 m/s, to 300 m/s each (an increase of 35% and decrease of 25%, respectively). This was assumed to be a reasonable assumption since the top 15 m at site IWTH04 was classified mostly as similar material (clayey silty sands and sandy clayey silts) according to the loosely translated boring log (see Appendix C). Figure 4.10 shows the observed amplification along with the computed amplification for the reported and adjusted shear wave velocity profiles. From Figure 4.10, the computed amplification at and above the site period are not significantly affected by the change in shear wave velocity, but the computed amplification from the adjusted shear wave velocity profile better matches the observed amplification at periods less than the site period. This suggests that the over-prediction of amplification at periods less than the site period at some sites may be due to inaccuracies in the shear wave velocities and/or thicknesses near the surface. However, the in situ seismic measurement methods used to measure the shear wave velocity are unknown and the raw measurements are not available; therefore, we are unable to definitively identify any potential errors in the surficial shear wave velocity profiles.

Table 4.5: Reported and adjusted shear wave velocity profiles for site IWTH04.

Layer No.	Thickness (m)	Depth (m)	Shear Wave Velocity, V_s (m/s)	
			Reported	Adjusted
1	5	5	220	300
2	10	15	400	300
3	34	49	830	830
4	60	109	2300	2300

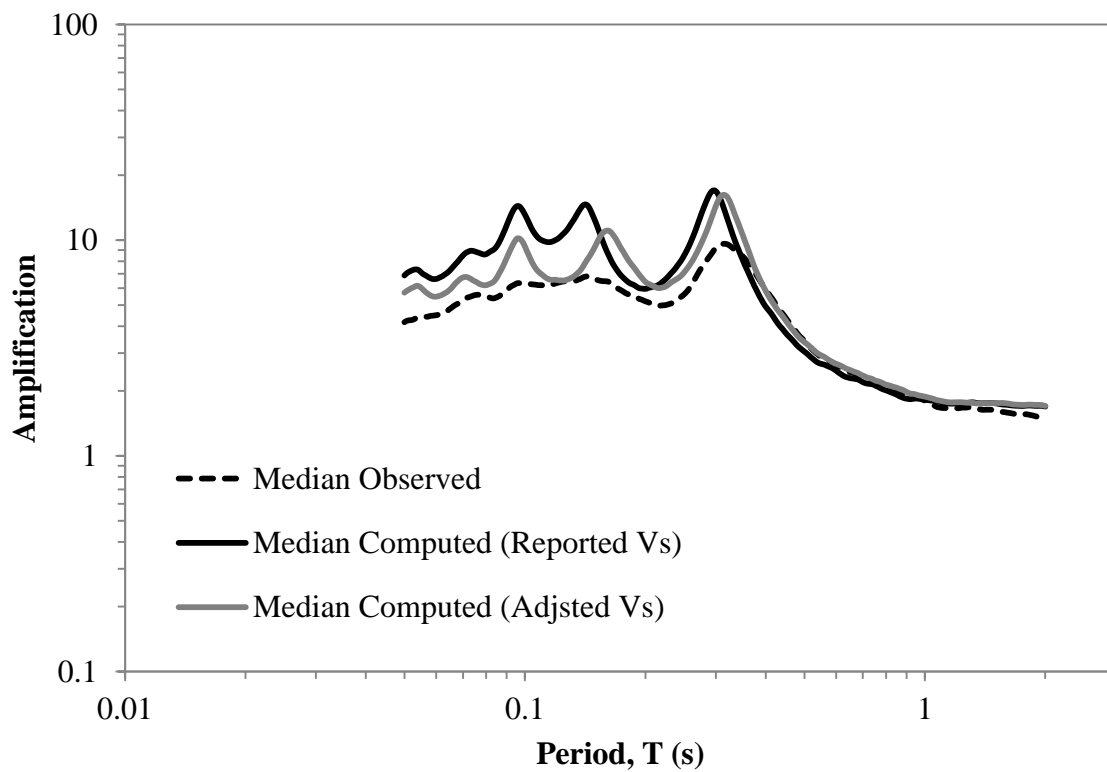


Figure 4.10: Observed and computed spectral amplification using reported and adjusted shear wave velocity profiles for site IWTH04.

4.4 LARGE INTENSITY SHAKING

In addition to comparing EQL site response analysis at low strains for low intensity shaking, we are also interested how well EQL site response analysis predicts surface motions at larger strains for large intensity shaking. Large intensity shaking is defined as having a calculated maximum shear strain of 0.01% or greater; for these motions, the soil response is more nonlinear. In order to compare similar levels of nonlinearity, comparisons were made for different levels of calculated maximum strain (i.e., 0.01 - 0.03%, 0.03 - 0.1%, and greater than 0.1%).

The computed and observed transfer functions for maximum strain levels of 0.01 - 0.03%, 0.03 - 0.1%, and greater than 0.1% are provided in Figure 4.11, Figure 4.12, and Figure 4.13, respectively. Figure 4.14 and Figure 4.15 show the median observed and computed transfer functions at all four strain bin levels for the 11 sites.

There is little change to the computed and observed transfer functions when comparing the results for strains levels less than 0.01% (discussed in Section 4.3) and for strain levels between 0.01 - 0.03%. The peaks of the computed and observed transfer functions decrease to some extent, but the general shapes of the transfer functions remain similar.

As strain levels increase from to 0.03 - 0.1% (Figure 4.12), the same frequency shortening effect described in Section 4.2 (i.e., transfer function decreasing and shifting towards lower frequencies) becomes more apparent. The peaks of the natural frequencies noticeably decrease, particularly at sites IWTH04, IWTH27, and MYGH06. The computed and observed transfer functions also decrease noticeably at frequencies greater than the natural frequencies for sites IWTH24 and MYGH06.

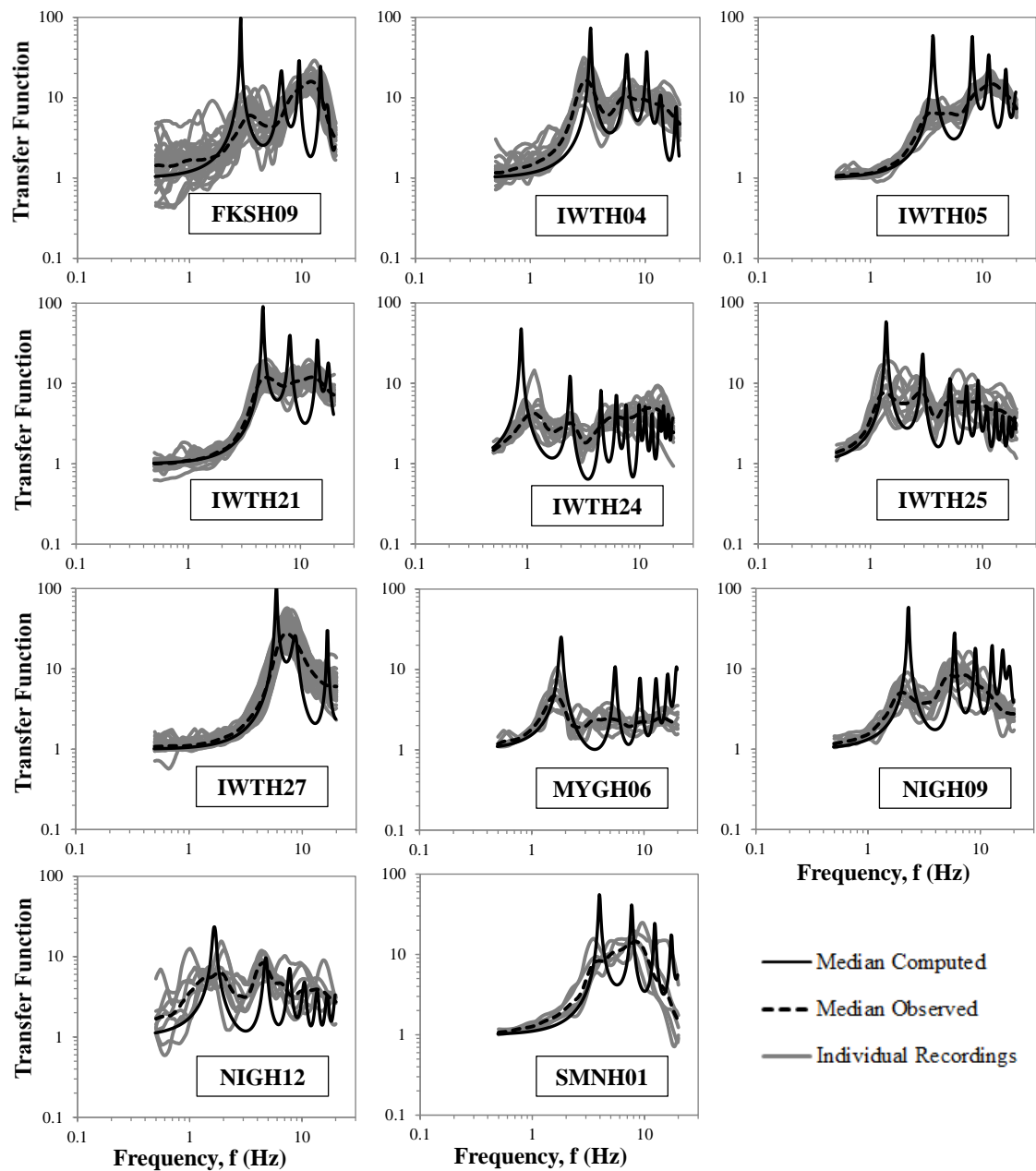


Figure 4.11: Transfer functions for large intensity shaking with calculated maximum shear strains between 0.01 and 0.03%.

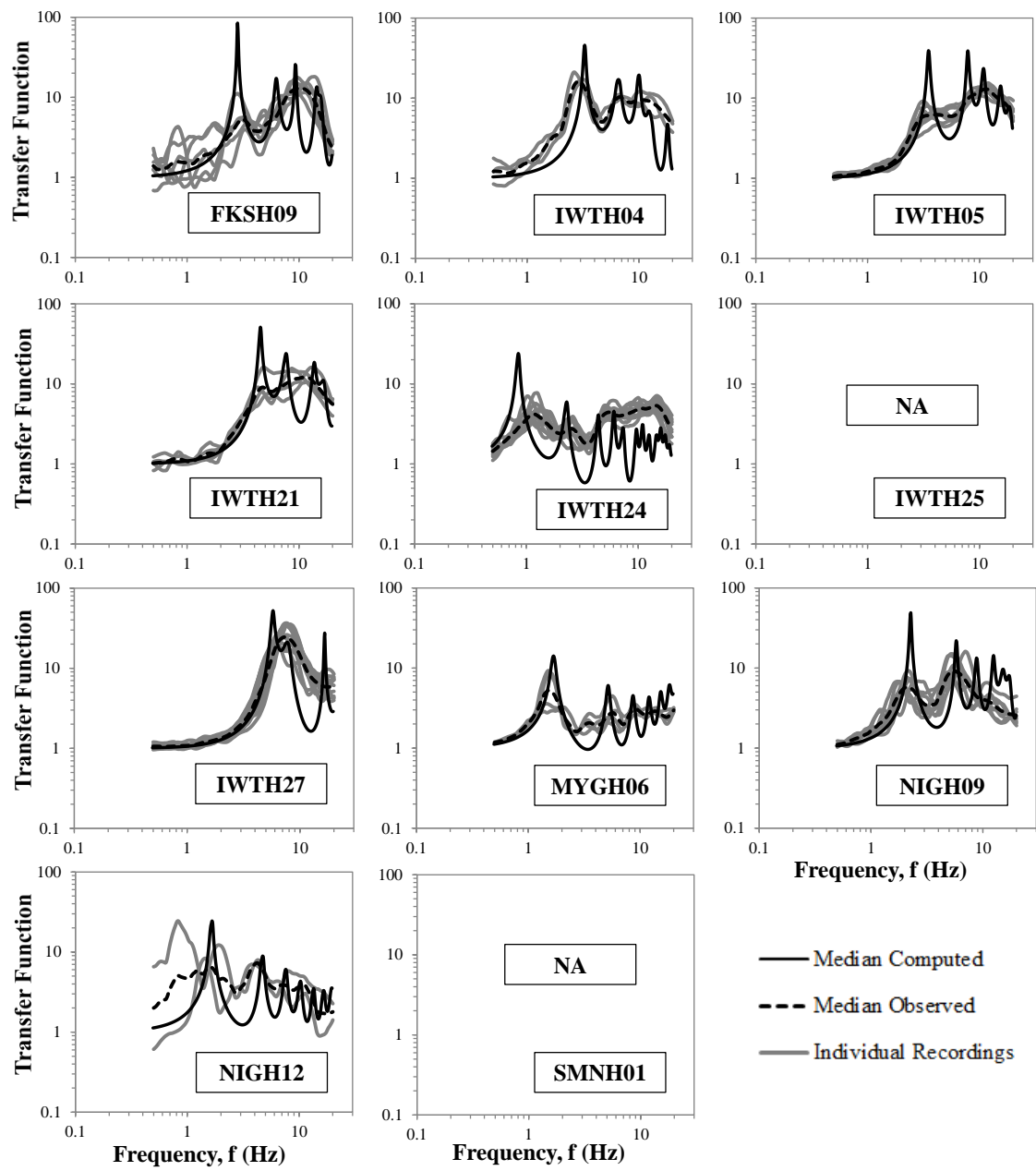


Figure 4.12: Transfer functions for large intensity shaking with calculated maximum shear strains between 0.03 and 0.1%.

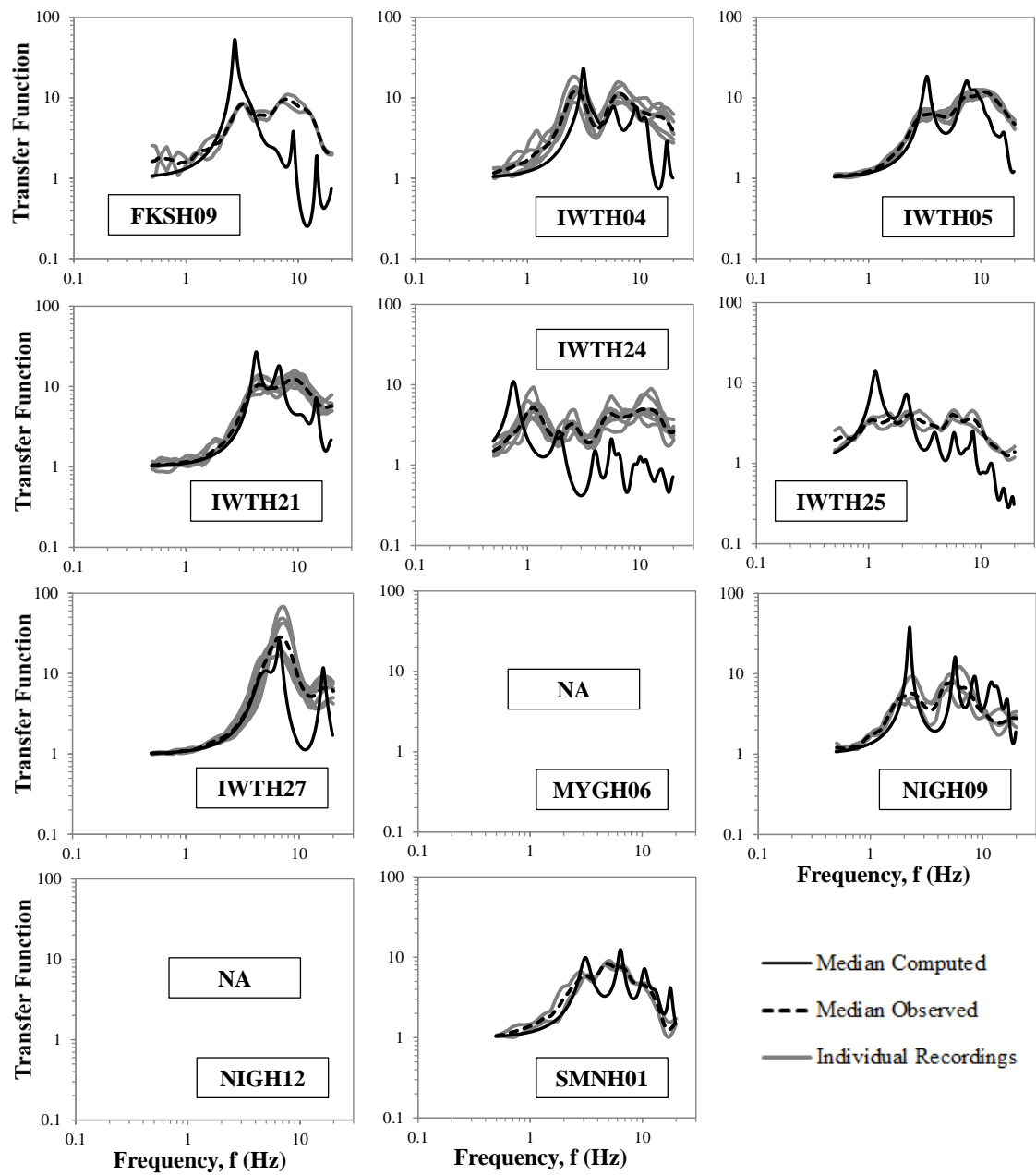


Figure 4.13: Transfer functions for large intensity shaking with calculated maximum shear strains of 0.1% or greater.

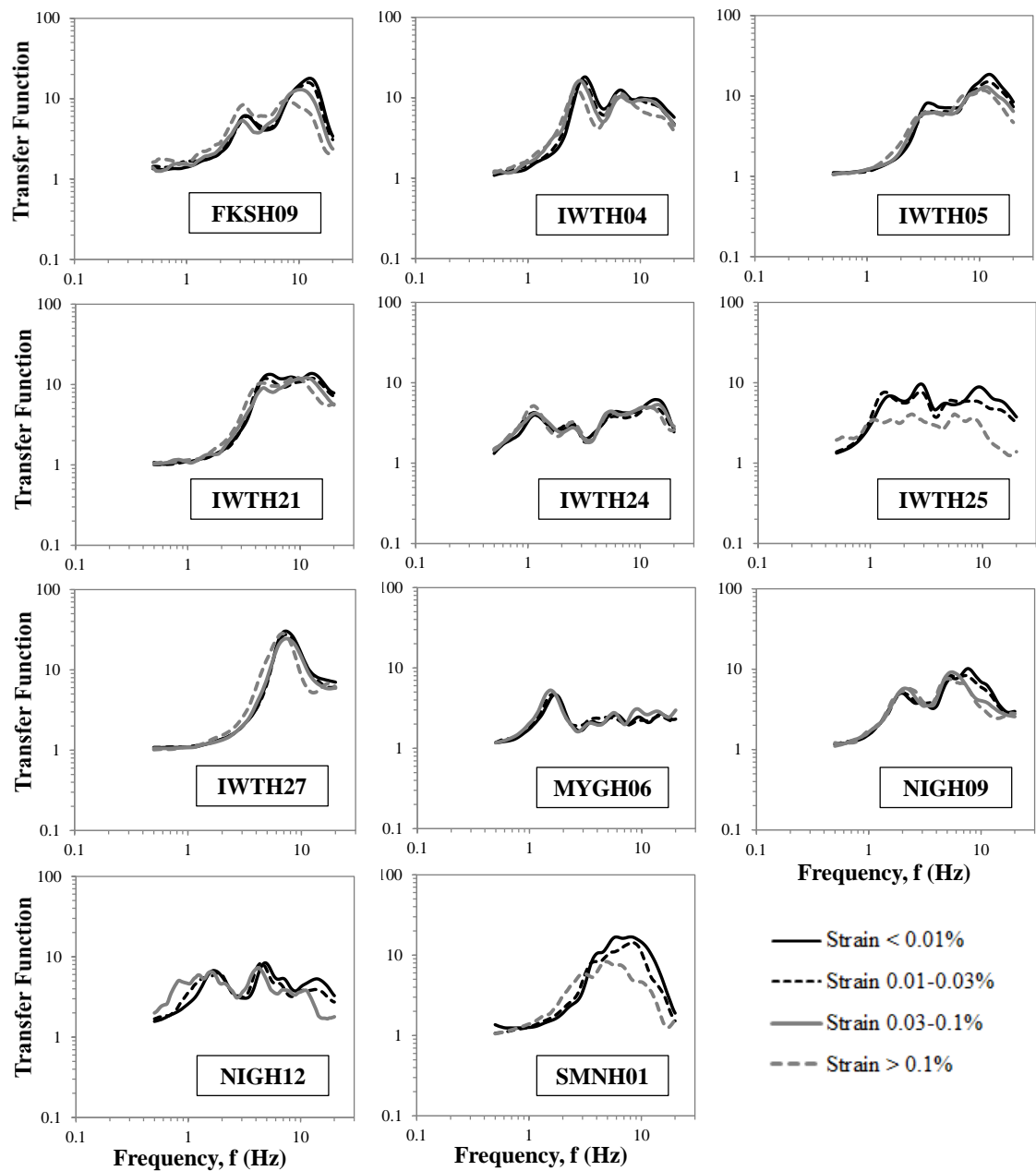


Figure 4.14: Observed transfer functions with calculated maximum shear strains less than 0.01%, 0.01 - 0.03%, 0.03 - 0.1%, and 0.1% or greater.

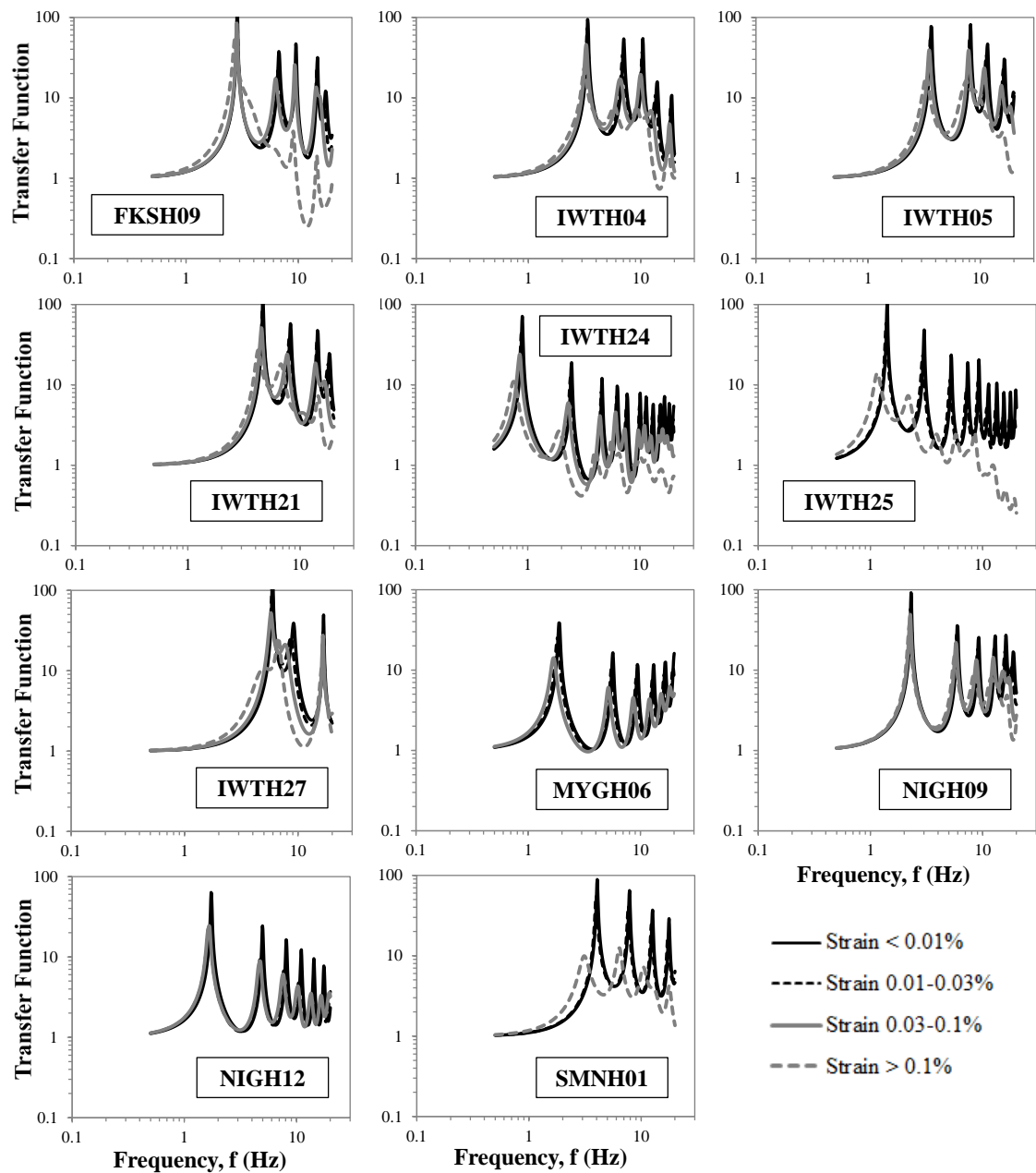


Figure 4.15: Computed transfer functions with calculated maximum shear strains less than 0.01%, 0.01 - 0.03%, 0.03 - 0.1%, and 0.1% or greater.

Care should be taken in the interpretation of the comparison for strains 0.1% or greater (Figure 4.13) due to the limited number of motions. Nonetheless, the frequency shortening effect for the computed response is most significant at these strain levels (Figure 4.13 and Figure 4.15). Significant decreases in the peaks of the computed transfer function across all sites are apparent. Significant decreases in the computed transfer function are also apparent at frequencies above the fundamental frequency and particularly for frequencies greater than 2 Hz. The computed transfer functions decrease at higher frequencies because damping has a greater effect on higher frequencies and at larger strains.

The largest calculated maximum shear strains at the 11 sites are summarized in Table 4.6. The sites that experience the largest maximum shear strains (greater than about 0.7%) show the most pronounced shortening effect for the computed transfer functions (i.e., sites FKSH09, IWTH04, IWTH05, and IWTH21). The shortening effect is the least pronounced at higher frequencies for sites MYGH06, NIGH09, NIGH12, and SMNH01, which have the lowest maximum shear strains. Note NIGH06 and NIGH12 do not have motions with maximum strains of 0.1% or greater.

Looking at the observed transfer functions across the different strain bins (Figure 4.14), there is a small change in the observed transfer functions for sites IWTH04, IWTH05, IWTH21, IWTH24, IWTH27, and MYGH06. Generally, we see a small amount of frequency shortening at these sites. There is significant change in the observed transfer functions at sites FKSH09, IWTH25, NIGH12, and SMNH01. The frequency shortening effect is most pronounced at calculated maximum shear strains of 0.1% or greater and at higher frequencies for these sites.

Table 4.6: Largest calculated maximum shear strain at the 11 sites.

KiK-net Site Name	Largest Calculated Maximum Shear Strain (%)
FKSH09	2.95
IWTH04	1.98
IWTH05	0.71
IWTH21	0.94
IWTH24	0.30
IWTH25	0.58
IWTH27	0.27
MYGH06	0.06
NIGH09	0.17
NIGH12	0.05
SMNH01	0.21

The computed and observed response spectral amplification for maximum strain levels of 0.01 - 0.03%, 0.03 - 0.1%, and greater than 0.1% are provided Figure 4.16, Figure 4.17, and Figure 4.18, respectively. Figure 4.19 and Figure 4.20 show the median observed and computed spectral amplification at the four strain bin levels for the 11 sites.

There is some change in the computed and observed amplification as strains levels increase from less than 0.01% to 0.01 - 0.03%, specifically at periods below the site period (Figure 4.16). As strain levels increase from 0.01 - 0.03% to 0.03 - 0.1% (Figure 4.17), the general shapes of the computed response remain similar, while the overall amplification decreases, particularly below the site periods. Again, the observed site periods are accounted for by the computed site periods, but with decreased peaks. Note that no motions are available corresponding to strains 0.03 – 0.1% for sites IWTH25 and SMNH01.

As previously mentioned, care should be taken in the interpretation of the comparison for strains 0.1% or greater (Figure 4.18) due to a limited number of motions. The most significant decrease in the computed amplification occurs at strain levels of

0.1% or greater. Significant decreases in the peaks of the computed amplification across all sites are seen from Figure 4.18 and Figure 4.20. Significant decreases in the computed amplification are also seen across all sites at periods below the site period and particularly for periods less than 0.5 s. The decreased computed amplification below the site period is most pronounced in sites FKSH09, IWTH04, IWTH05, IWTH24, IWTH25, IWTH27, and SMNH01.

Considering the observed amplification across all strain bins (Figure 4.19), there is only a small change in the observed amplification across all strain levels for sites IWTH04, IWTH05, IWTH21, IWTH24, MYGH06, NIGH09, and NIGH12. In general, the amplification slightly decreases and shifts slightly towards higher periods at these sites. There is significant change in the observed amplification at sites FKSH09, IWTH25, IWTH27, and SMNH01 with increasing shear strain levels. These sites experienced strains greater than 0.2% (Table 4.6). As shear strain levels increase, the observed response significantly decreases at periods less than the site period for site FKSH09 and above the site period for site IWTH27. The computed response decreases at all periods with increasing shear strain levels for sites IWTH25 and SMNH01, with the most pronounced decrease at strain levels of 0.1% or greater.

Sites FKSH09, IWTH05, NIGH12, and SMNH01 noticeably over-predict the amplification at strain levels 0.01 - 0.03%, while they reasonably predicted the response at strain levels less than 0.01%. Site IWTH25 reasonably predicts the response at strain levels 0.01 – 0.03%, while it under-predicted at strain levels less than 0.01%. Like the transfer function, the peaks of the computed and observed amplification decrease to some extent, but the general shapes of the amplification remain similar. The individual site trends at and above the site period for strain levels less than 0.01% is similar to the trends

for strain levels 0.01 – 0.03%. The decrease in the amplification is due to the increase in damping from larger strains.

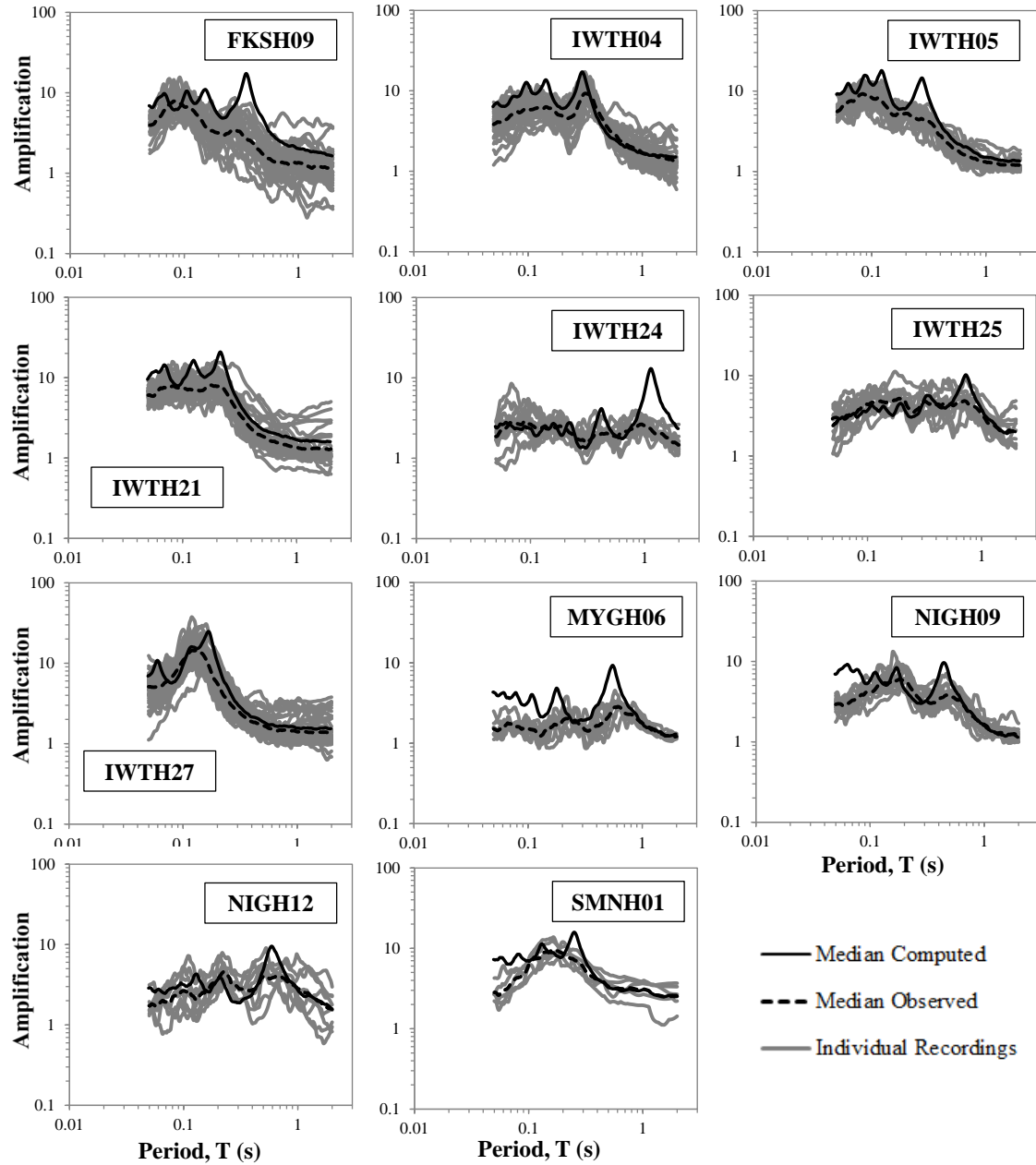


Figure 4.16: Spectral amplification for large intensity shaking with calculated maximum shear strains between 0.01 and 0.03%.

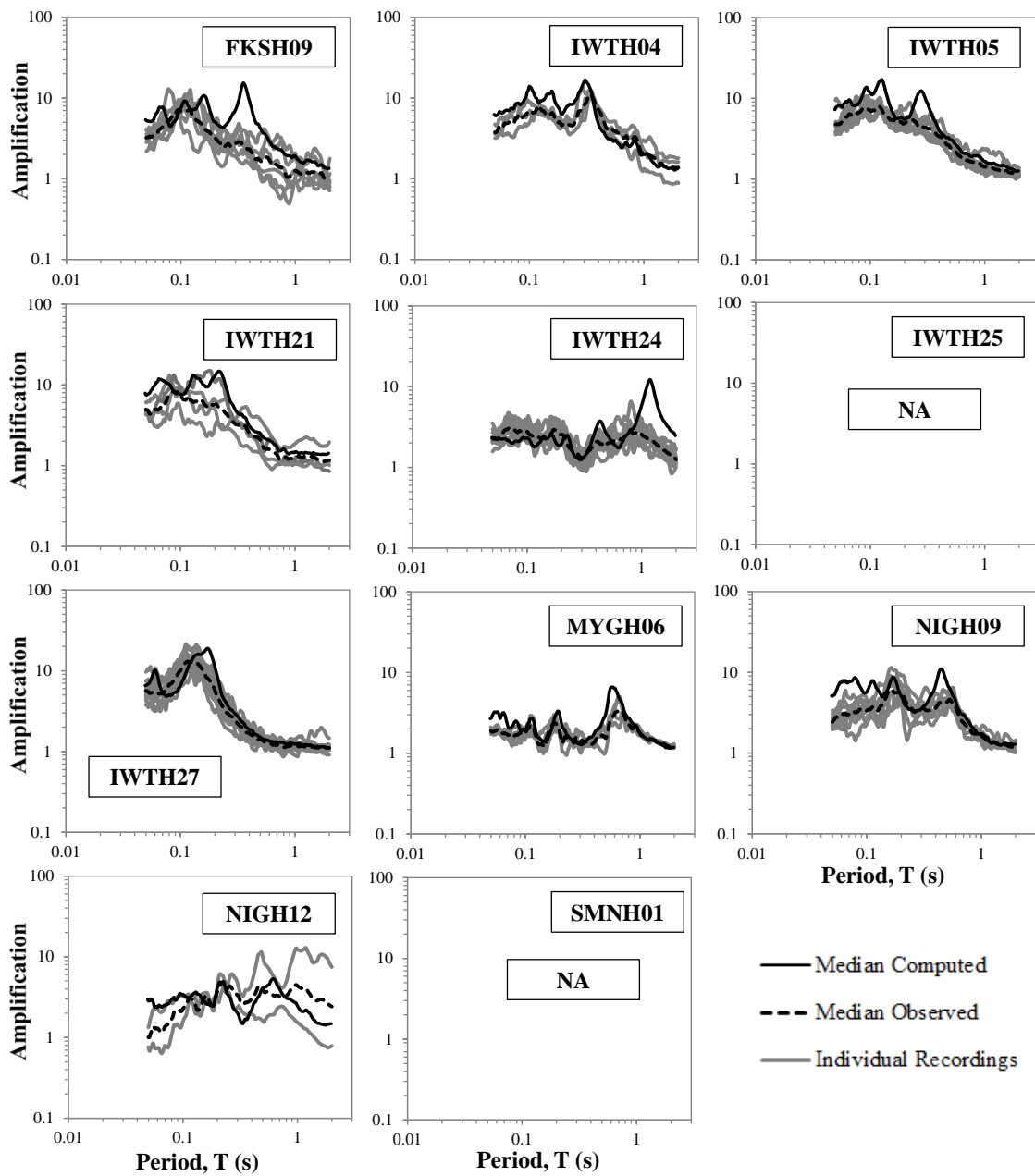


Figure 4.17: Spectral amplification for large intensity shaking with calculated maximum shear strains between 0.03 and 0.1%.

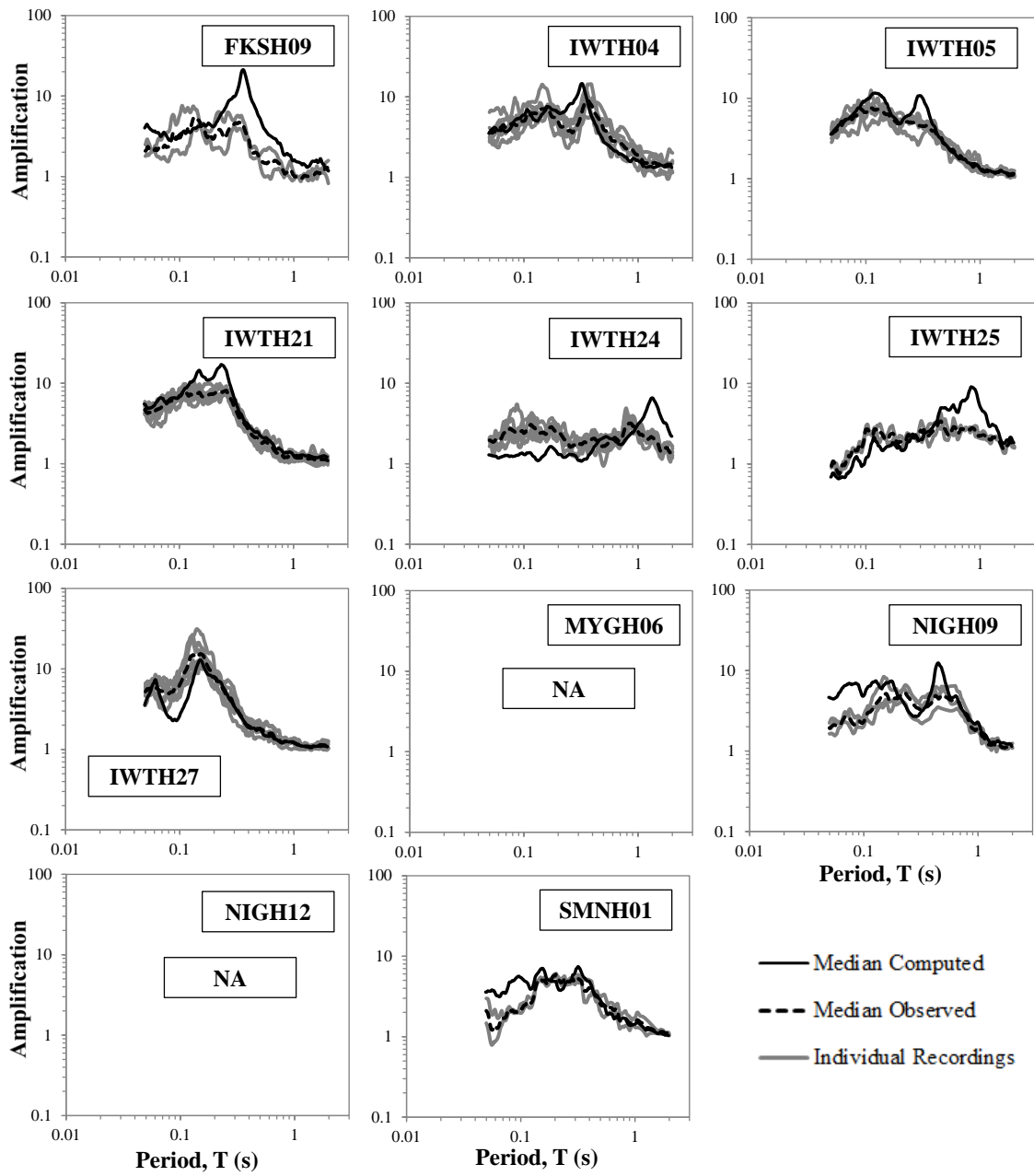


Figure 4.18: Spectral amplification for large intensity shaking with calculated maximum shear strains of 0.1% or greater.

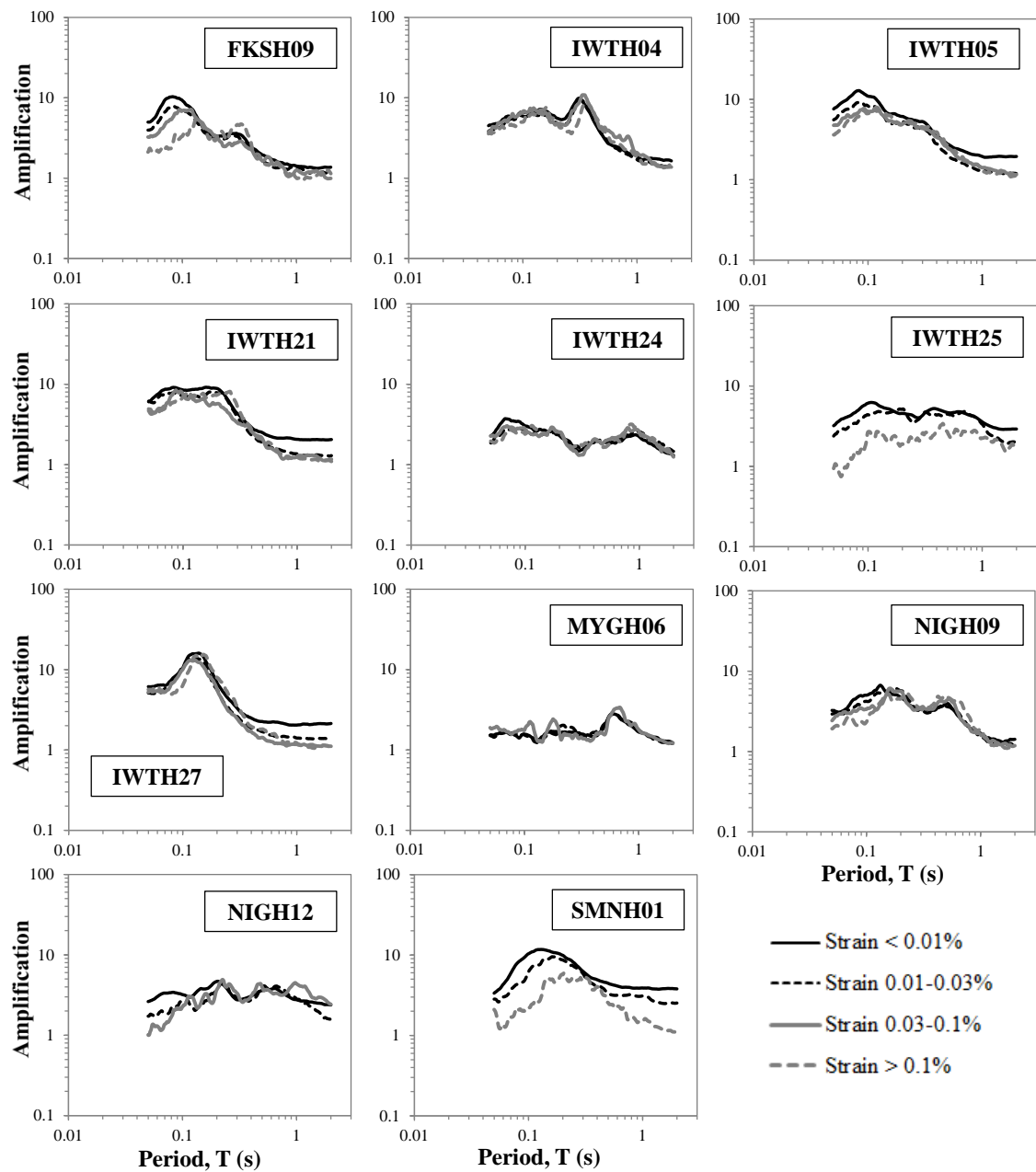


Figure 4.19: Observed spectral amplification with calculated maximum shear strains less than 0.01%, 0.01 - 0.03%, 0.03 - 0.1%, and 0.1% or greater.

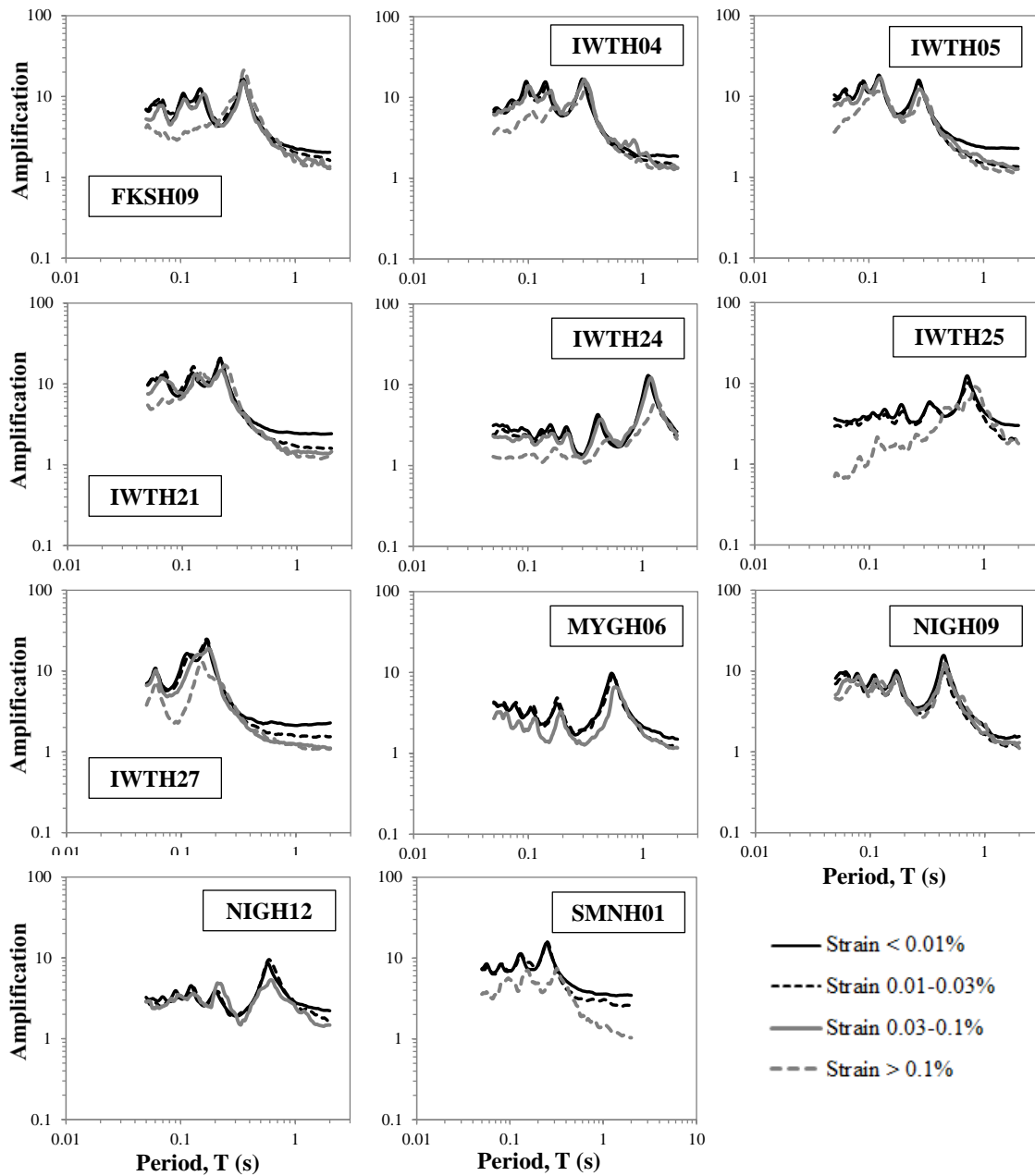


Figure 4.20: Computed spectral amplification with calculated maximum shear strains less than 0.01%, 0.01 - 0.03%, 0.03 - 0.1%, and 0.1% or greater

4.5 AGGREGATED RESULTS

The residual is the difference between the observed and computed response spectral amplification at a given period and is a measure of the over- or under-prediction of the calculated response from EQL site response analysis. To investigate the strain dependence of the residuals on a finer scale, the residual is computed for 15 strain bins between 0.001% and 10%, spaced equally in log space. The residuals were determined at periods from 0.05 to 2 s.

The average residuals within each strain bin were calculated from the residuals of the motions corresponding to each strain bin. The average residuals are represented using a contour color plot in which the x-axis represents period T , the y-axis represents the maximum shear strain, and the color represents the residuals. Blue (negative residual) represents over-prediction, red (positive residual) represents under-prediction, and white/gray represents reasonable agreement between the computed and observed amplification within +/-20%.

The average residuals plotted versus period T and T/T_{SITE} for the individual 11 sites are provided in Appendix A. Care should be taken in the interpretation of the individual site contour color plots because there may be only a few motions per strain bin. When aggregating data across sites this issue is not much of a concern because it is less likely that a strain bin will have only a few motions.

The residuals were averaged across all sites for each strain bin to generate aggregate average residual contour color plots in Figure 4.21. The computed site period was used to normalize the period because the observed site period would be unknown apriori in an EQL site response analysis.

A summary of the computed, observed, and approximated site periods, including the percent difference between the computed and observed site periods, is provided in Table 4.7. The computed and observed site periods are the site periods identified by the longest period peak in the median computed and observed spectral amplification, respectively. The approximated site periods were calculated using $4 \cdot D_{\text{base}} / V_{s \text{ AVG}}$, where $V_{s \text{ AVG}}$ is the average shear wave velocity from the surface to the installation depth of the base sensor (D_{base}). The computed site periods are reasonable considering they are within +/-20% of the observed site periods, with the exception of site SMNH01. The approximated site periods in some cases are more different from the observed values, which may indicate some errors in the reported shear wave velocity profiles.

Table 4.7: Summary of computed, observed, and approximated KiK-net site periods.

KiK-net Site Name	Site Period, T_{SITE} (s)			Percent Difference Computed & Observed
	Computed	Observed	Approximated ($4D_{\text{base}}/V_{s \text{ AVG}}$)	
FKSH09	0.35	0.30	0.49	18
IWTH04	0.30	0.31	0.46	5
IWTH05	0.27	0.30	0.43	8
IWTH21	0.22	0.20	0.37	9
IWTH24	1.12	0.93	1.15	21
IWTH25	0.72	0.64	0.96	11
IWTH27	0.17	0.14	0.29	21
MYGH06	0.53	0.60	0.56	11
NIGH09	0.44	0.51	0.57	14
NIGH12	0.58	0.64	0.63	10
SMNH01	0.25	0.13	0.39	91

The number of recordings per shear strain bin used for the individual site and aggregate average residual contour color plots are shown in Table 4.8. The percent contribution of the number of motions for each site to each strain bin and the aggregate residual contour color plots is provided in Table 4.9. A minimum of 4 motions per shear strain bin was used to generate the individual site average residual contour color plots (Appendix A) and the aggregate average residual contour color plots (Figure 4.21). Bolded numbers indicate sites that comprise at least 30% of the motions for a given strain bin and drive the computed residual at that strain level. Bins shaded gray represent the shear strain bins used to generate the average residual contour color plots. Residual strain bins that do not have at least four recordings were not included in the average residual color plots. Shear strain bins that did not have at least four motions, but were between bins of four or more motions were interpolated. For example, strain bins 2, 4 through 9, and 12 were used to generate the individual residual color plots for site IWTH24. Shear strain bins 1, and 13 through 15 were not included, and strain bins 3, and 10 through 11 are interpolated. A total of 910 motions were considered for the aggregate average residual contour color plots, as opposed to the 930 motions for the transfer function and spectral amplification comparisons, because a maximum shear strain of 0.001% or greater and a minimum of 4 motions per strain bin was used that excluded 20 motions.

Table 4.8: Number of recordings per strain bin for average residual contour color plots. Bins shaded gray represents shear strains used to generate residual contour color plots.

Bin	Maximum Shear Strain	Number of KiK-net Recordings											
		FKSH09	IWTH04	IWTH05	IWTH21	IWTH24	IWTH25	IWTH27	MYGH06	NIGH09	NIGH12	SMNH01	Aggregate
1	0.001 - 0.0016	1	0	2	0	0	28	0	0	0	14	1	46
2	0.0016 - 0.0026	5	0	11	1	6	16	0	0	1	29	10	79
3	0.0026 - 0.0041	4	3	23	19	3	23	11	2	1	11	18	118
4	0.0041 - 0.0066	19	16	25	39	9	13	22	7	5	10	12	177
5	0.0066 - 0.0105	30	18	27	32	13	12	27	4	12	3	7	185
6	0.0105 - 0.0168	14	18	11	24	8	6	23	4	4	4	4	120
7	0.0168 - 0.0268	8	8	11	7	5	2	16	5	7	4	0	73
8	0.0268 - 0.043	7	3	5	2	5	2	12	1	4	1	1	43
9	0.043 - 0.0687	2	1	3	1	4	0	5	3	4	1	0	24
10	0.0687 - 0.11	0	1	0	1	2	0	2	0	2	0	0	8
11	0.11 - 0.2199	0	4	2	2	1	0	5	0	2	0	2	18
12	0.2199 - 0.4398	0	1	2	4	6	1	1	0	0	0	0	15
13	0.4398 - 0.8796	0	0	2	1	0	1	0	0	0	0	0	4
14	0.8796 - 2	1	1	0	1	0	0	0	0	0	0	0	3
15	2 - 10	1	0	0	0	0	0	0	0	0	0	0	1
Total		92	74	124	134	62	104	124	26	42	77	55	914

Table 4.9: Percent contribution of recordings to strain bin per site and percent contribution of each strain bin to total number of motions for aggregate average residual contour color plots.

Bin	Maximum Shear Strain (%)	Percent Contribution of KiK-net Recordings											
		FKSH09	IWTH04	IWTH05	IWTH21	IWTH24	IWTH25	IWTH27	MYGH06	NIGH09	NIGH12	SMNH01	Aggregate
1	0.001 - 0.0016	2	0	4	0	0	61	0	0	0	30	2	5
2	0.0016 - 0.0026	6	0	14	1	8	20	0	0	1	37	13	9
3	0.0026 - 0.0041	3	3	19	16	3	19	9	2	1	9	15	13
4	0.0041 - 0.0066	11	9	14	22	5	7	12	4	3	6	7	19
5	0.0066 - 0.0105	16	10	15	17	7	6	15	2	6	2	4	20
6	0.0105 - 0.0168	12	15	9	20	7	5	19	3	3	3	3	13
7	0.0168 - 0.0268	11	11	15	10	7	3	22	7	10	5	0	8
8	0.0268 - 0.043	16	7	12	5	12	5	28	2	9	2	2	5
9	0.043 - 0.0687	8	4	13	4	17	0	21	13	17	4	0	3
10	0.0687 - 0.11	0	13	0	13	25	0	25	0	25	0	0	1
11	0.11 - 0.2199	0	22	11	11	6	0	28	0	11	0	11	2
12	0.2199 - 0.4398	0	7	13	27	40	7	7	0	0	0	0	2
13	0.4398 - 0.8796	0	0	50	25	0	25	0	0	0	0	0	0.4
14	0.8796 - 2	33	33	0	33	0	0	0	0	0	0	0	0.3
15	2 - 10	100	0	0	0	0	0	0	0	0	0	0	0.1
Total		10	8	14	15	7	11	14	3	5	8	6	100

The aggregate average residual contour color plots as a function of period T and normalized period (T/T_{SITE}) are provided in Figure 4.21. Overall, there is both good agreement (white and gray residual) and moderate over-prediction (blue residual) between the computed and observed amplification.

For the residuals plotted as a function of period (Figure 4.21(a)), the computed amplification may be as much as 2.5 times larger than observed (Residual ~ -0.9). The residual is observed to vary more at certain periods with increasing shear strain as compared to others. The maximum over-prediction at periods between 0.05 and 0.07 s occurs at strain levels of approximately 0.02%. As shear strain increases above 0.03% and decreases below 0.015%, the level of over-prediction decreases. At periods between approximately 0.07 and 0.1 s, there is good agreement between the computed and observed amplification across all strain levels except at the lowest and highest strains levels. At periods between 0.1 and 0.4 s, the maximum over-prediction occurs at strain levels between approximately 0.004 and 0.04%. As shear strain increases above 0.04% and decreases below 0.004%, the level of over-prediction decreases. At periods between 0.4 and 0.6 s, the maximum over-prediction occurs at strain levels of approximately 0.07 and 0.15%. As shear strain increases above 0.15% and decreases below 0.07%, the level of over-prediction decreases. At periods between 0.6 and 0.9 s, the maximum over-prediction occurs at strain levels of approximately 0.001 and 0.002%. As shear strain increases above 0.002%, the level of over-prediction decreases. At periods between 0.2 and 2.0 s, the over-prediction occurs at strain levels of approximately 0.005 and 0.015%, and 0.05 and 0.2%, with reasonable agreement between the computed and observed amplification for strain levels in between.

From Figure 4.21(a), a minor under-prediction was experienced at lower periods and lower shear strains. Table 4.8 and Table 4.9 show that 61% of the 46 motions from shear strain bin 1 (0.001 – 0.0016%) and 20% of the 79 motions from shear strain bin 2 (0.0016 – 0.0026%) are contributed by site IWTH25. From Figure 4.9, site IWTH25 under-predicts the response at approximately 0.5 s and less. The fact that site IWTH25 dominates the data for shear strain bins 1 and 2 offers an explanation to why the aggregate response was under-predicted, especially at low periods and low shear strains.

The trend of the results is that the maximum difference between the observed and computed responses occurs around a maximum shear strain of approximately 0.01 to 0.03%, with the results in better agreement at smaller and larger strains. It was expected that the results would move from over-prediction to under-prediction (or vice versa) as shear strain increased. No explanation for the trend of the results is offered and more research is required to offer reasonable conclusions.

Figure 4.21(b) shows the residuals as a function of T/T_{SITE} . At $T/T_{\text{SITE}} \sim 1.0$, there is significant over-prediction at the site period (i.e., computed amplification as much as 2.5 times larger than observed, Residual = - 1.0) due to the fact that “within” boundary condition produces a large predicted response at the site period. Because each site has a different site period, this consistent over-prediction is masked in Figure 4.21(a) but is readily apparent in Figure 4.21(b). For periods less than the site period ($T/T_{\text{SITE}} < 1.0$), we again see that the maximum over-prediction occurs around a strain level of 0.02% with less over-prediction at smaller and larger strains.

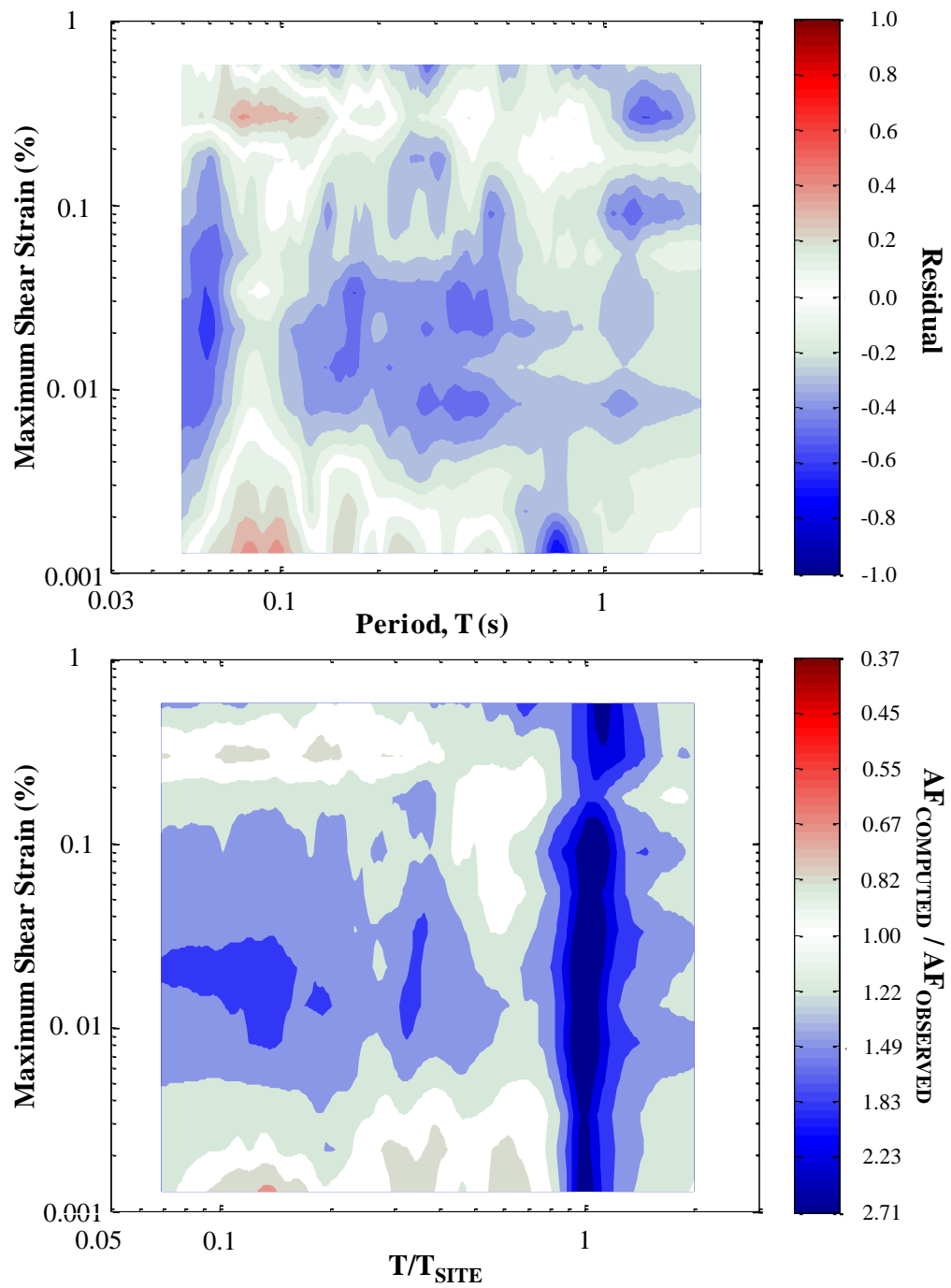


Figure 4.21: (a) Aggregate average residuals plotted versus period T and (b) aggregate average residuals plotted versus T/T_{SITE} for 910 motions across 11 sites. Blue represents over-prediction and red represents under-prediction.

Chapter 5: Summary, Conclusions, and Recommendations

5.1 SUMMARY

Accurately predicting surface ground motions is a critical aspect of geotechnical earthquake engineering. Equivalent-linear (EQL) site response analysis is a numerical technique used to compute surface ground motions from input motions at bedrock using the site-specific dynamic soil properties. These surface motions play an important role in earthquake engineering applications. The purpose of this study was to investigate the accuracy of EQL site response analysis for stiff soil sites by comparing computed and observed transfer functions and response spectral amplification.

The Kiban Kyoshin network (KiK-net) in Japan is a seismograph network consisting of approximately 700 downhole array sites with strong-motion accelerometers located at the ground surface and at depth. The National Research Institute for Earth Science and Disaster Prevention (NIED) in Japan publishes strong-motion recordings and shear wave velocity profiles for most KiK-net sites. Observed transfer functions and response spectral amplification were determined at 11 sites and for 930 individual seismic recordings.

Computed transfer functions and response spectral amplification were calculated from EQL site response analysis by specifying the KiK-net base sensor motion as the input motion and using the published shear wave velocity profiles. Sites were also characterized using nonlinear soil properties estimated from empirical models.

Computed and observed transfer functions and response spectral amplification were compared at different levels of strain for each site. The average difference between

the observed and computed response spectral amplification across the 11 sites were compared at different levels of strain.

5.2 CONCLUSIONS

Overall, there is reasonable agreement between the computed and observed transfer functions and response spectral amplification. There is agreement between the computed and observed fundamental site periods. There is mostly over-prediction of the computed transfer functions and response spectral amplification at the observed site periods due to the “within” boundary condition assumed at the base of the downhole array, which models fully the destructive interference of the up going and down going waves. Higher modes were often predicted by the theoretical model, but not always observed by the recordings at some sites. There is very good agreement between the computed and observed transfer functions and response spectral amplification for periods larger than the site periods.

There is less agreement between the computed and observed transfer functions and response spectral amplification for periods less than the site period. There is mostly over-prediction of the response spectral amplification at these periods, while some under-prediction also occurred. Inaccurate shear wave velocity profiles may account for the lack of agreement between the computed and observed response spectral amplification at periods below the site periods. Nonetheless, across all 11 sites the predicted spectral amplification is within +/-20% at maximum shear strains less than 0.01%. At maximum shear strains between approximately 0.01 and 0.03%, the spectral amplification is over-predicted, in some instances by as little as 5% and in other instances by a factor of 2 or more.

5.3 RECOMMENDATIONS FOR FUTURE STUDIES

With the completion of this study, several recommendations can be offered for future studies that compare the observed response from downhole arrays at stiff soil sites to the computed response from EQL site response analysis.

Increasing the number of sites and motions will allow for better and more even coverage across strain bins that will better characterize the variation of the average residual with strain. This approach will avoid individual sites dominating and/or driving the computed residuals at different levels of strain. In general, increasing the number of sites and motions is recommended for future studies since it provides a better representation of the median observations for a given site.

Future studies could develop calibrated shear wave velocity profiles for KiK-net sites before comparing computed and observed response spectra. Calibrating the shear wave velocity profiles may help improve the accuracy of the site response comparison at periods below the site periods. Using linear-elastic site response analysis and low intensity input motions, the shear wave velocity profiles could be calibrated by varying the layer thicknesses and/or shear wave velocities (within acceptable limits) until the computed response best fit the observed response, particularly at lower periods. The calibrated model that best fit the observed response could be used in the site response comparison.

Appendix A: Individual Site Average Residual Plots

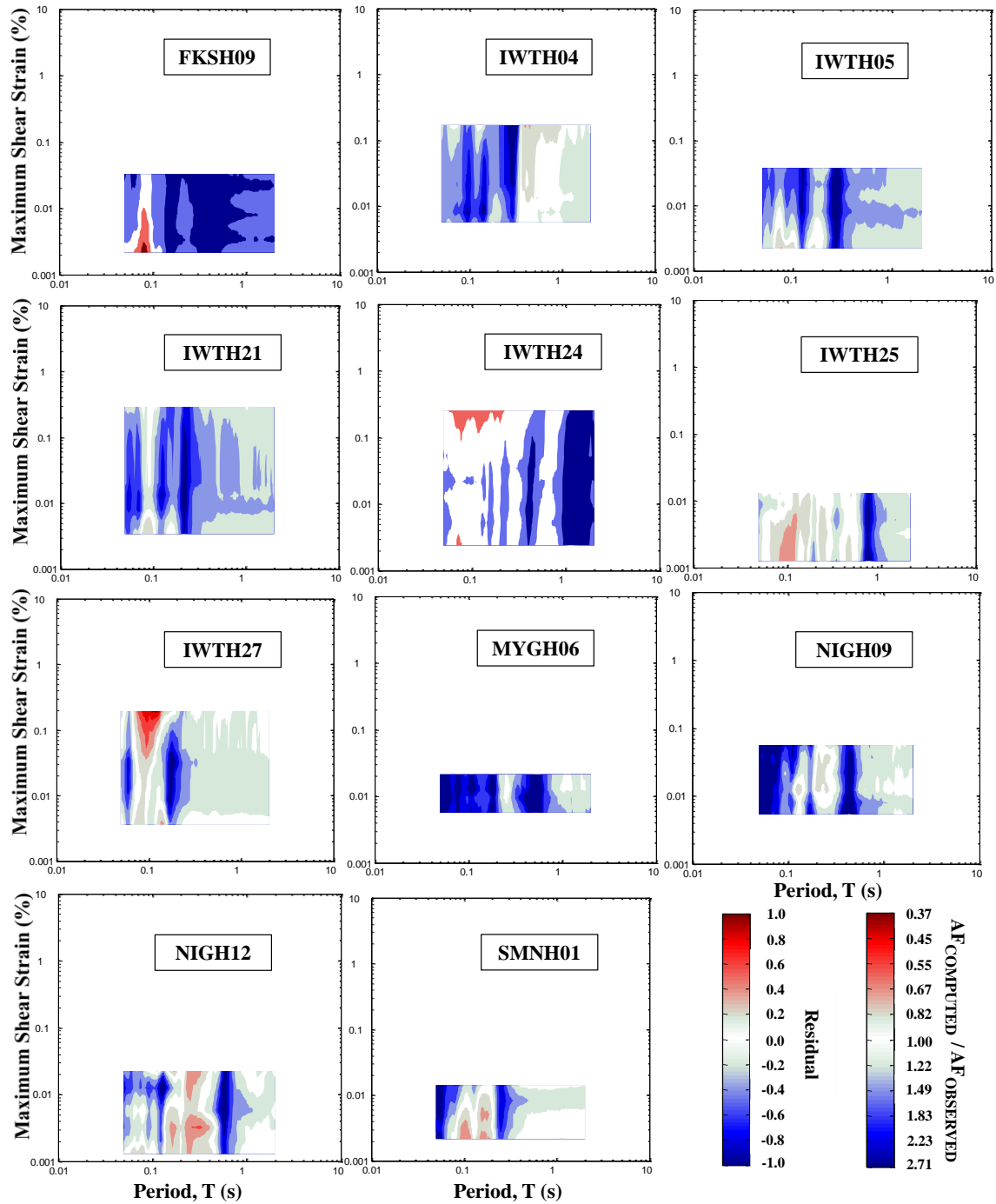


Figure A.1: Average residuals plotted versus period T for the 11 individual sites. Blue represents over-prediction and red represents under-prediction.

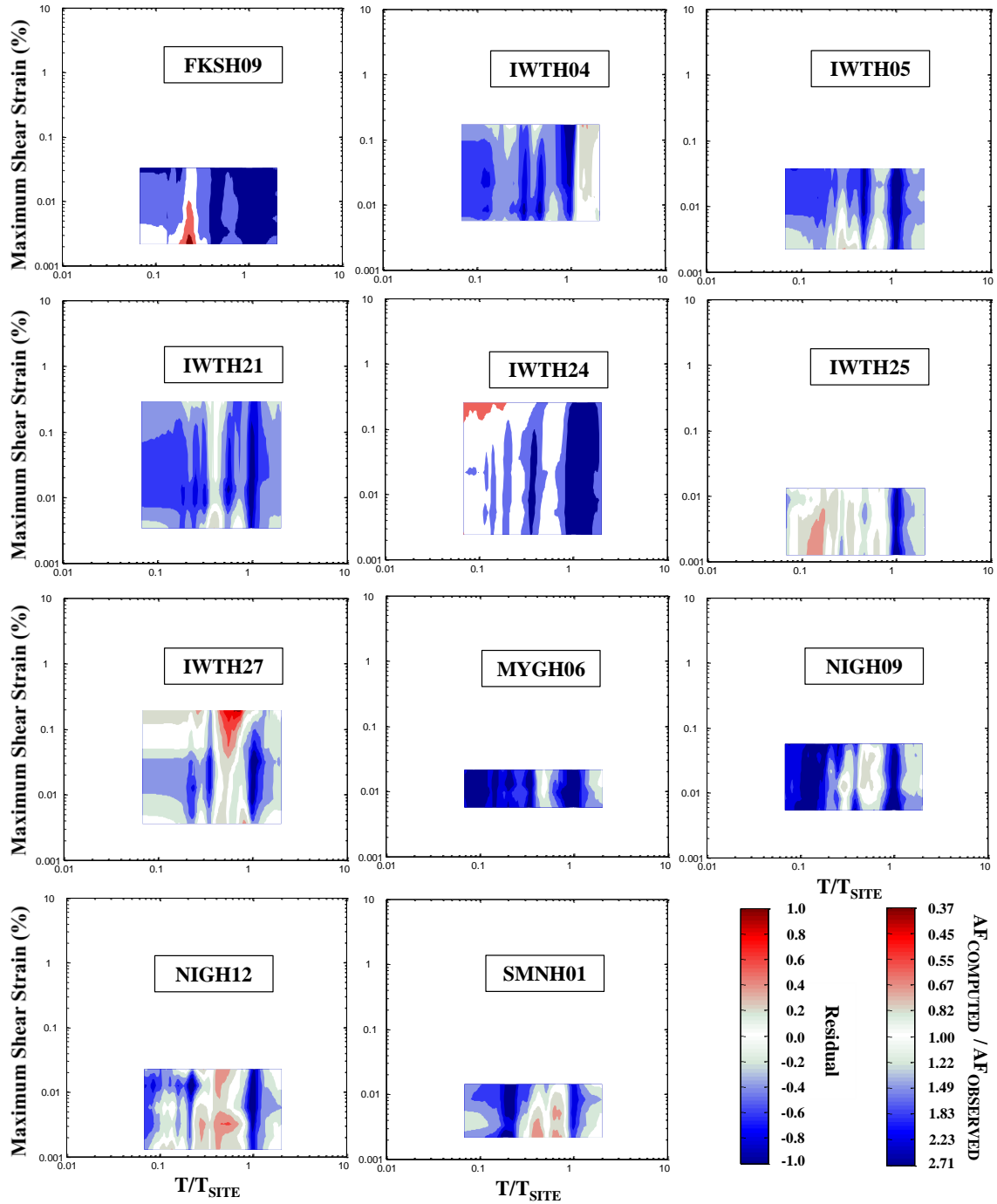


Figure A.2: Average residuals plotted versus T/T_{SITE} for the 11 individual sites. Blue represents over-prediction and red represents under-prediction

Appendix B: Layer Discretization for EQL Site Response Analysis

Table B.1: Site FKSH09 layer discretization for EQL site response analysis.

Layer No.	Thickness (m)	Depth (m)	V_s (m/s)	σ'_m (atm)
1	2	2	140	0.25
2	8	10	300	0.69
3	34	44	1930	1.96
4	126	170	2540	6.79
5	30	200	1960	11.51

Table B.2: Site IWTH04 layer discretization for EQL site response analysis.

Layer No.	Thickness (m)	Depth (m)	V_s (m/s)	σ'_m (atm)
1	5	5	220	0.31
2	10	15	400	0.93
3	34	49	830	2.26
4	60	109	2300	5.10

Table B.3: Site IWTH05 layer discretization for EQL site response analysis.

Layer No.	Thickness (m)	Depth (m)	V_s (m/s)	σ'_m (atm)
1	2	2	160	0.25
2	7	9	350	0.66
3	17	26	520	1.38
4	11	37	850	2.23
5	11	48	1500	2.89
6	55	103	2600	4.89

Table B.4: Site IWTH21 layer discretization for EQL site response analysis.

Layer No.	Thickness (m)	Depth (m)	V_s (m/s)	σ'_m (atm)
1	2	2	150	0.25
2	6	8	320	0.63
3	4	12	400	0.93
4	8	20	990	1.29
5	20	40	1350	2.14
6	30	70	2000	3.65
7	30	100	2460	5.46

Table B.5: Site IWTH24 layer discretization for EQL site response analysis.

Layer No.	Thickness (m)	Depth (m)	V_s (m/s)	σ'_m (atm)
1	2	2	180	0.25
2	8	10	480	0.69
3	38	48	590	2.08
4	8	56	300	3.47
5	34	90	550	4.74
6	28	118	600	6.61
7	32	150	540	8.43

Table B.6: Site IWTH25 layer discretization for EQL site response analysis.

Layer No.	Thickness (m)	Depth (m)	V_s (m/s)	σ'_m (atm)
1	6	6	430	0.38
2	28	34	530	1.53
3	30	64	680	3.29
4	48	112	1120	5.64
5	64	176	1780	9.03
6	28	204	1380	11.81
7	56	260	1810	14.35

Table B.7: Site IWTH27 layer discretization for EQL site response analysis.

Layer No.	Thickness (m)	Depth (m)	V_s (m/s)	σ'_m (atm)
1	4	4	150	0.25
2	12	16	1100	0.93
3	30	46	1950	2.20
4	32	78	2590	4.07
5	22	100	2790	5.70

Table B.8: Site MYGH06 layer discretization for EQL site response analysis.

Layer No.	Thickness (m)	Depth (m)	V_s (m/s)	σ'_m (atm)
1	2	2	200	0.25
2	84	86	690	2.98
3	14	100	1480	5.95

Table B.9: Site NIGH09 layer discretization for EQL site response analysis.

Layer No.	Thickness (m)	Depth (m)	V_s (m/s)	σ'_m (atm)
1	2	2	150	0.25
2	6	8	400	0.63
3	4	12	400	0.93
4	34	46	680	2.08
5	34	80	880	4.13
6	20	100	1380	5.76

Table B.10: Site NIGH12 layer discretization for EQL site response analysis.

Layer No.	Thickness (m)	Depth (m)	V_s (m/s)	σ'_m (atm)
1	2	2	240	0.25
2	12	14	500	0.81
3	36	50	730	2.26
4	60	110	780	5.16

Table B.11: Site SMNH01 layer discretization for EQL site response analysis.

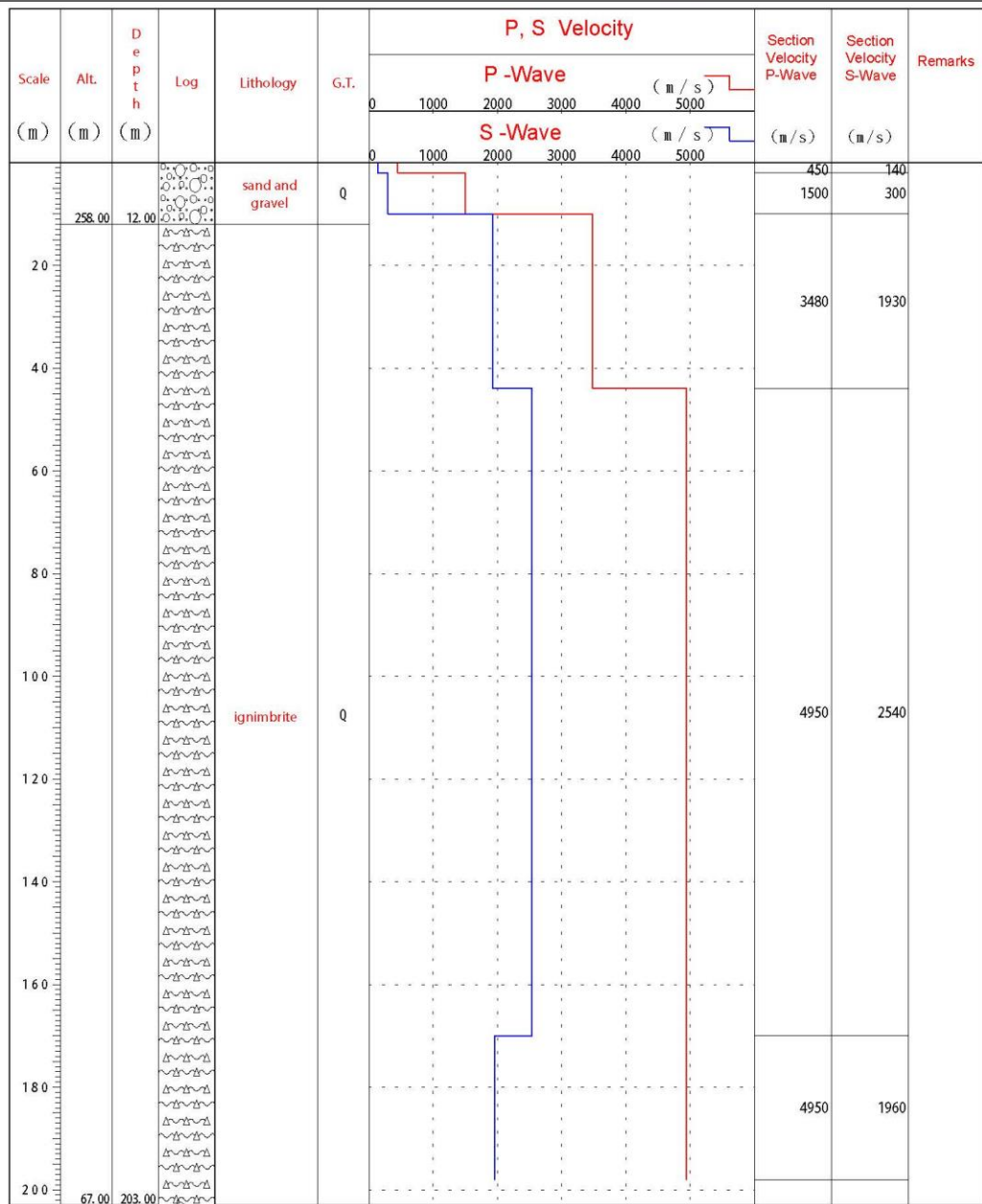
Layer No.	Thickness (m)	Depth (m)	V_s (m/s)	σ'_m (atm)
1	4	4	290	0.25
2	7	11	290	0.78
3	11	22	550	1.32
4	20	42	1200	2.26
5	12	54	1900	3.54
6	47	101	2800	6.03

Appendix C: KiK-net Site Boring Logs

Soil and Rock Condition

Station Point : 郡山(こおりやま)
 Location : 福島県郡山市田村町小川字石淵166
 Latitude : 37° 21' 0.00"
 Altitude : +270m

Station Code : FKSH09
 Longitude : 140° 25' 47.0"
 Depth : 203.00m



ボーリング柱状図(暫定版)

観測点名： 住田(すみた)

所在地： 岩手県気仙郡住田町世田米字子飼沢30-191

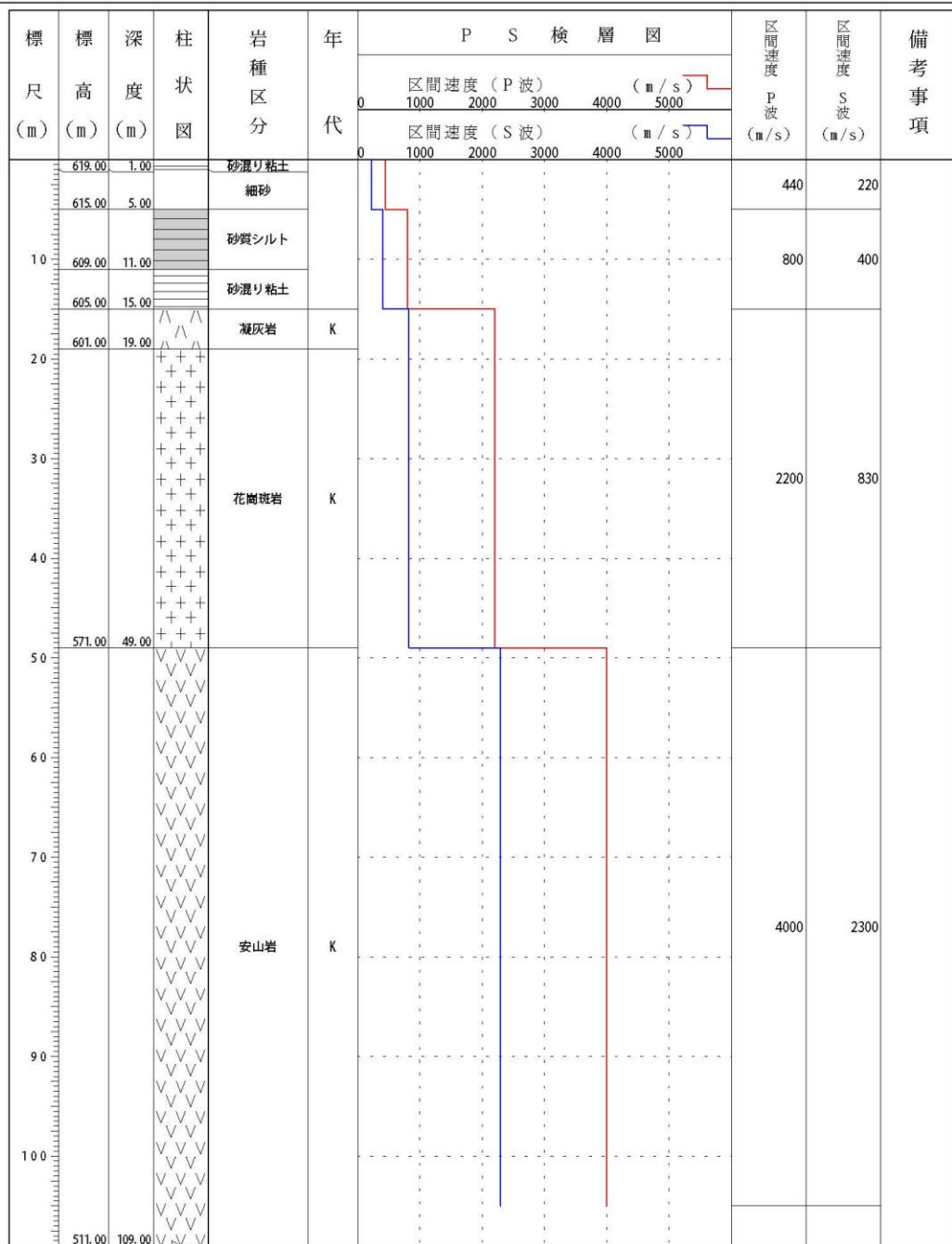
緯度： 39° 10' 41.0"

孔口標高： +620m

観測点コード： IWITH04

経度： 141° 23' 40.0"

総掘進長： 109.00m



Soil and Rock Condition

Station Point : 住田(すみた)

Location : 岩手県気仙郡住田町世田米字子飼沢30-191

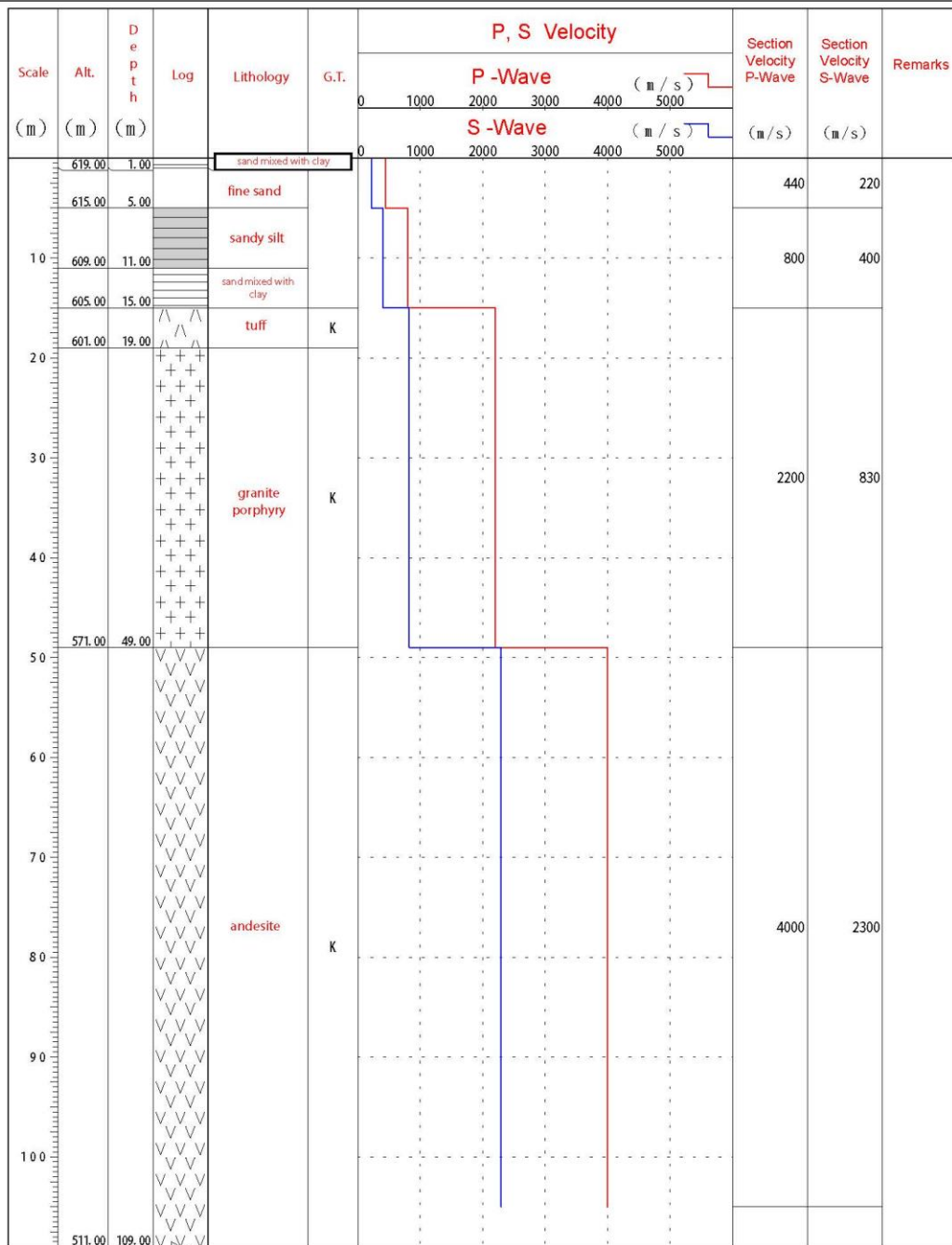
Latitude : 39° 10' 41.0"

Altitude : +620m

Station Code : IWTH04

Longitude : 141° 23' 40.0"

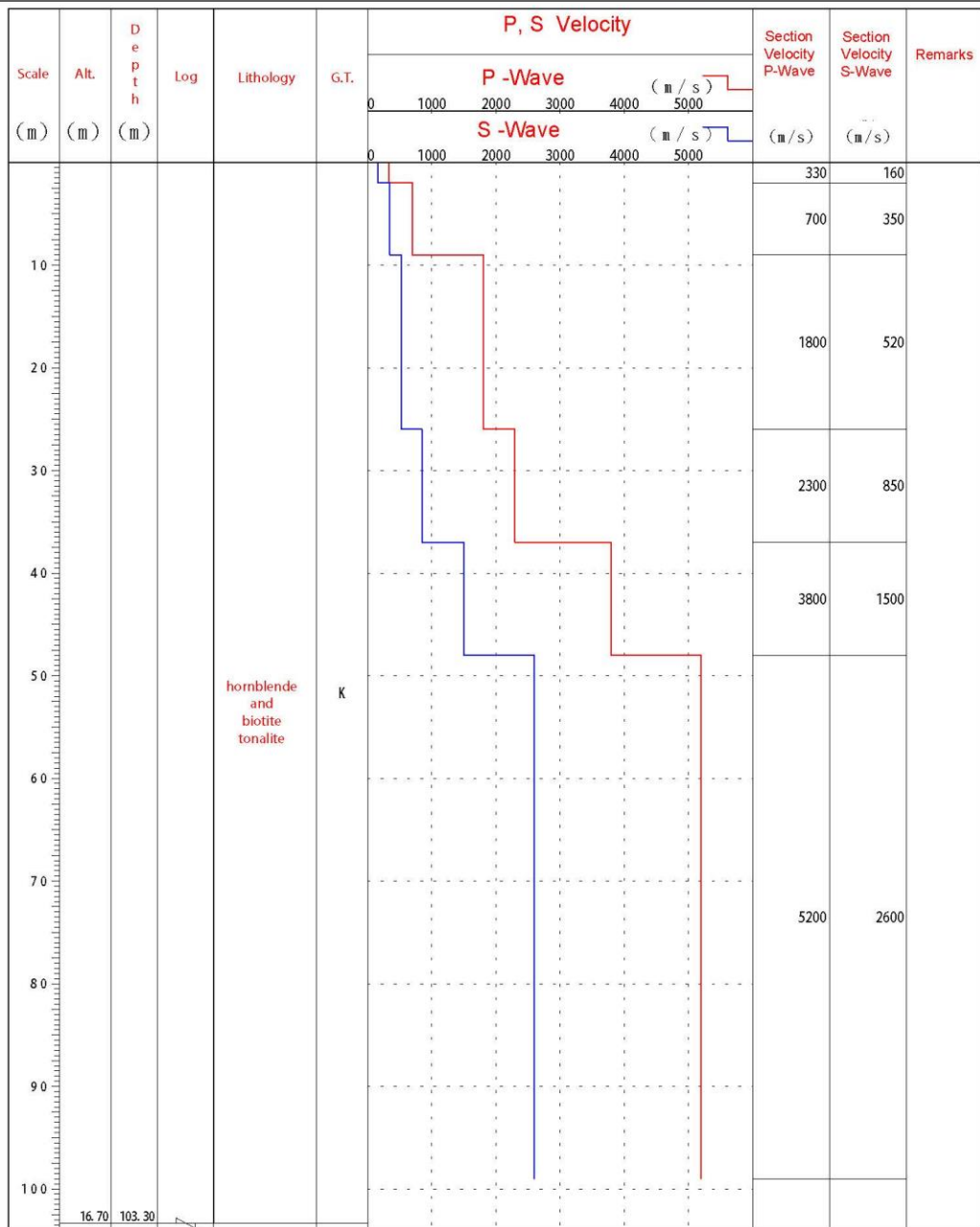
Depth : 109.00m



Soil and Rock Condition

Station Point : 藤沢(ふじさわ)
 Location : 岩手県東磐井郡藤沢町藤沢字仁郷50
 Latitude : 38° 51' 45.0
 Altitude : +120m

Station Code : IWTH05
 Longitude : 141° 21' 17.0 ''
 Depth : 103.30m



ボーリング柱状図(暫定版)

観測点名： 山田(やまだ)

所在地： 岩手県下閉伊郡山田町山田6-9-10

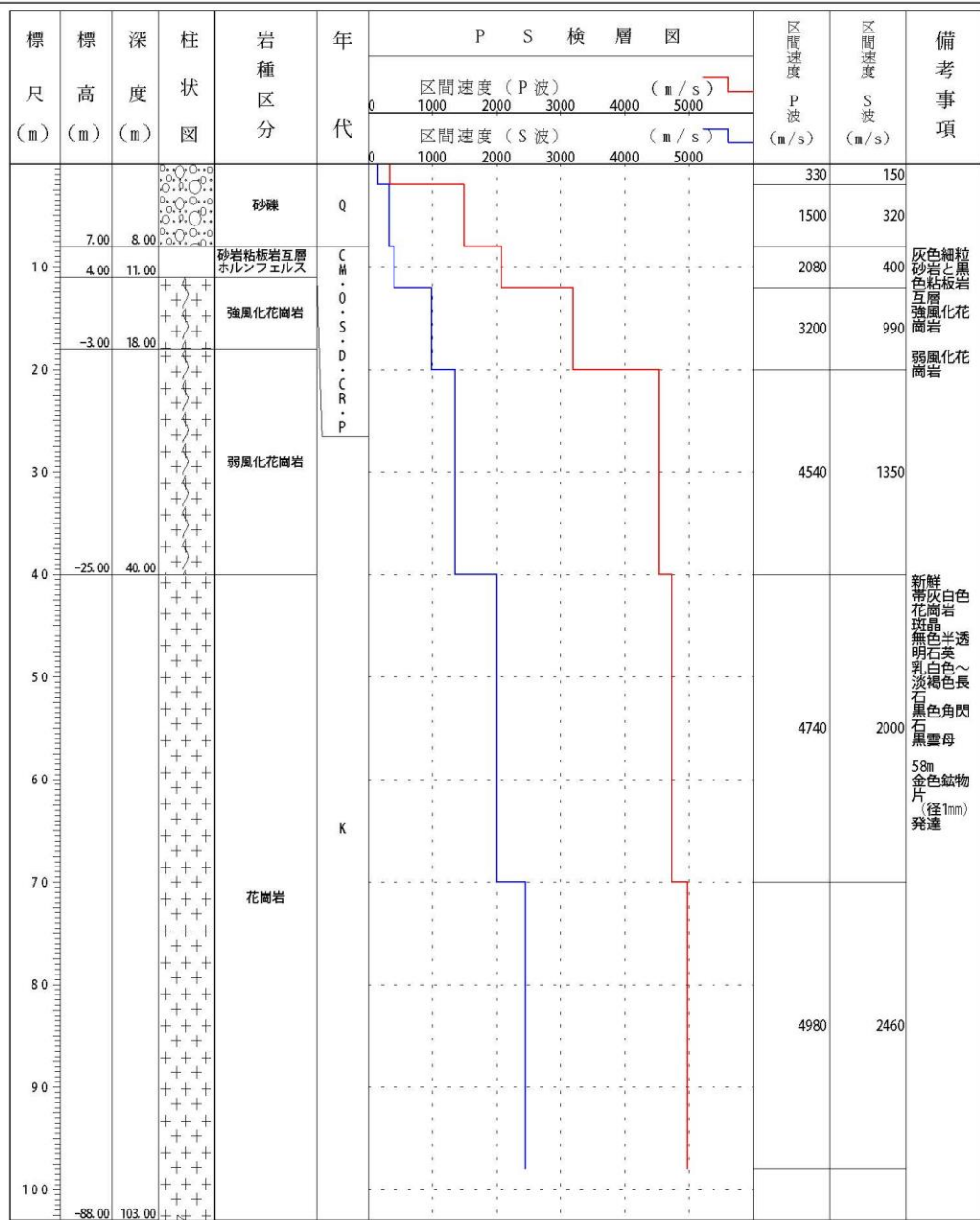
緯度： 39° 28' 14.0"

孔口標高： +15m

観測コード： IWTH21

経度： 141° 56' 14.0"

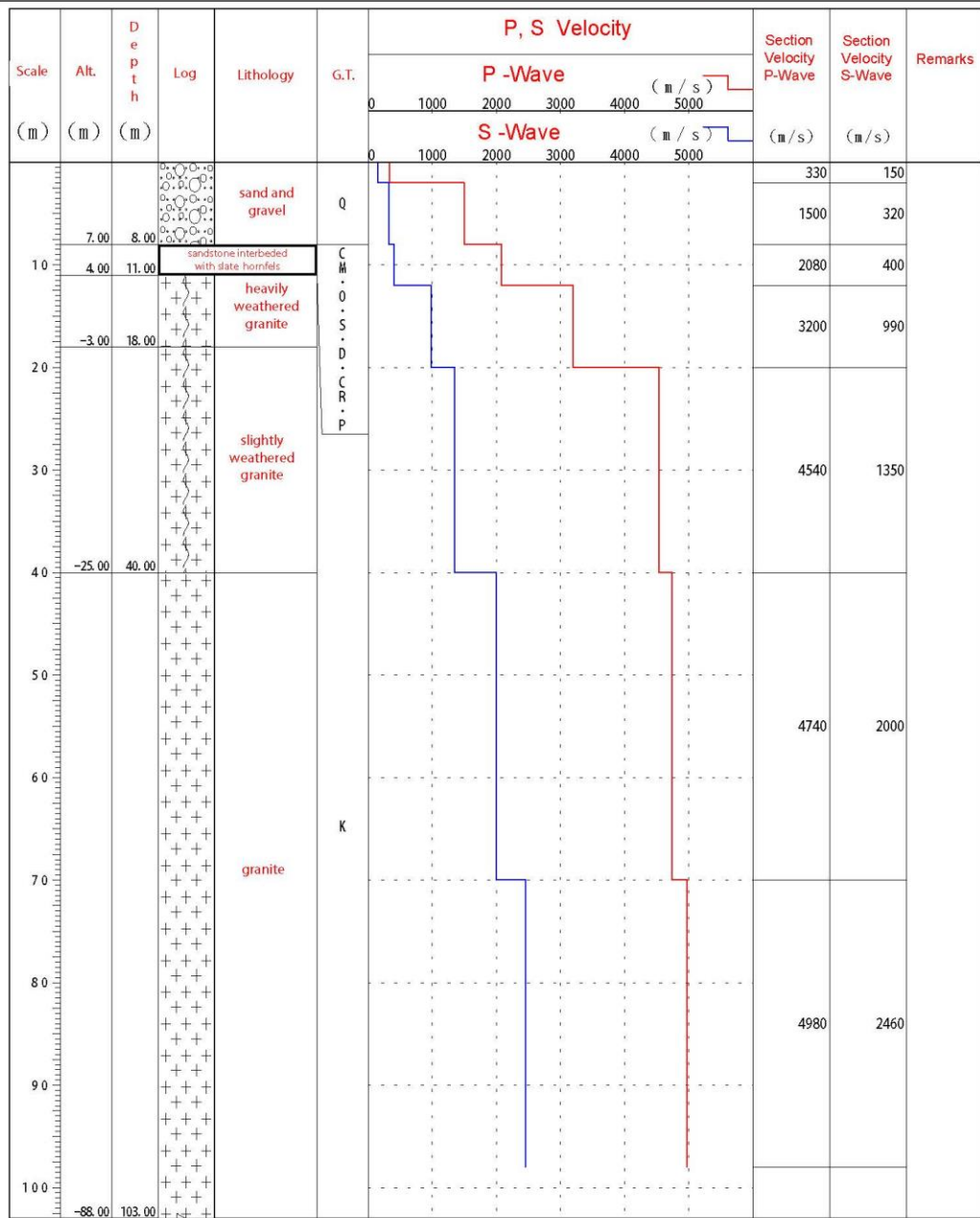
総掘進長： 103.00m



Soil and Rock Condition

Station Point : 山田(やまだ)
 Location : 岩手県下閉伊郡山田町山田6-9-10
 Latitude : 39° 28' 14.0"
 Altitude : +15m

Station Code : IWTH21
 Longitude : 141° 56' 14.0"
 Depth : 103.00m



ボーリング柱状図(暫定版)

観測点名： 金ヶ崎(かねがさき)

所在地： 岩手県胆沢郡金ヶ崎町西根和光183-1

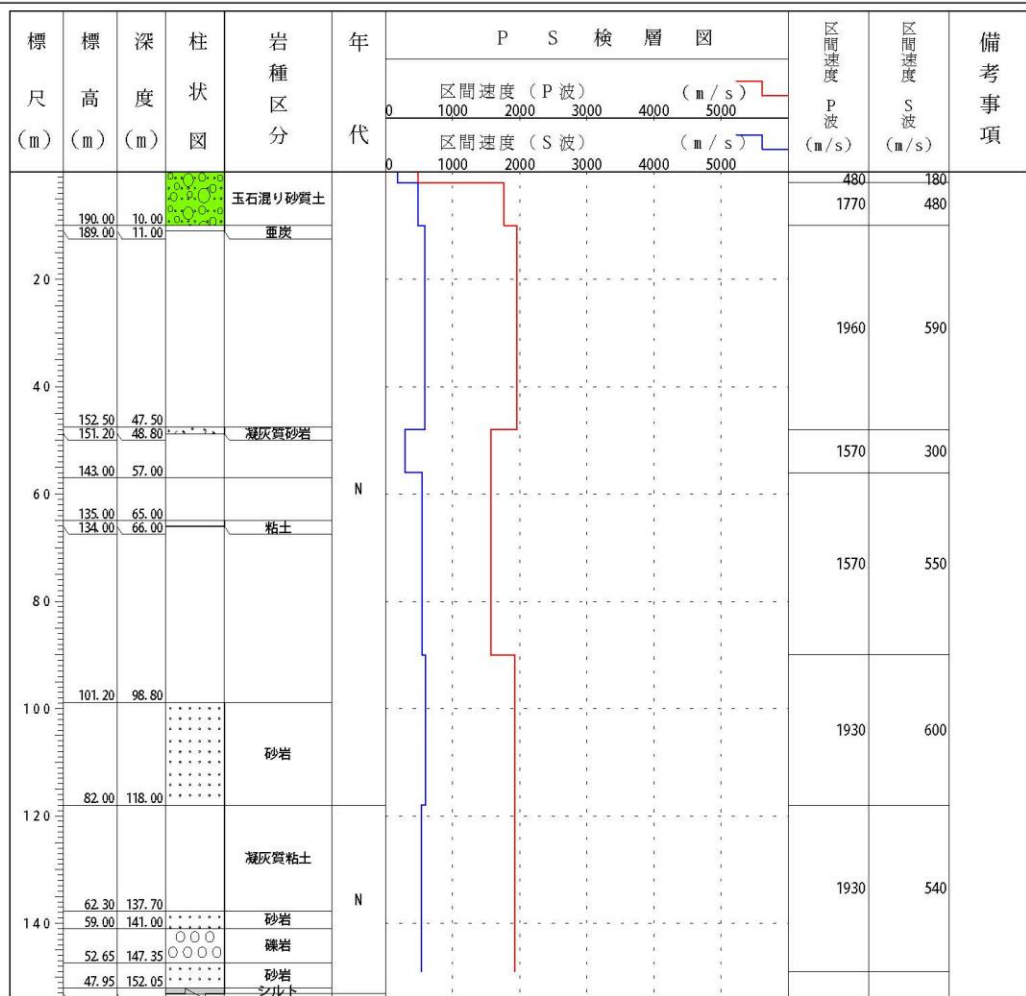
緯度： 39° 11' 42.0"

孔口標高： +200m

観測点コード： IWITH24

経度： 141° 0' 55.0"

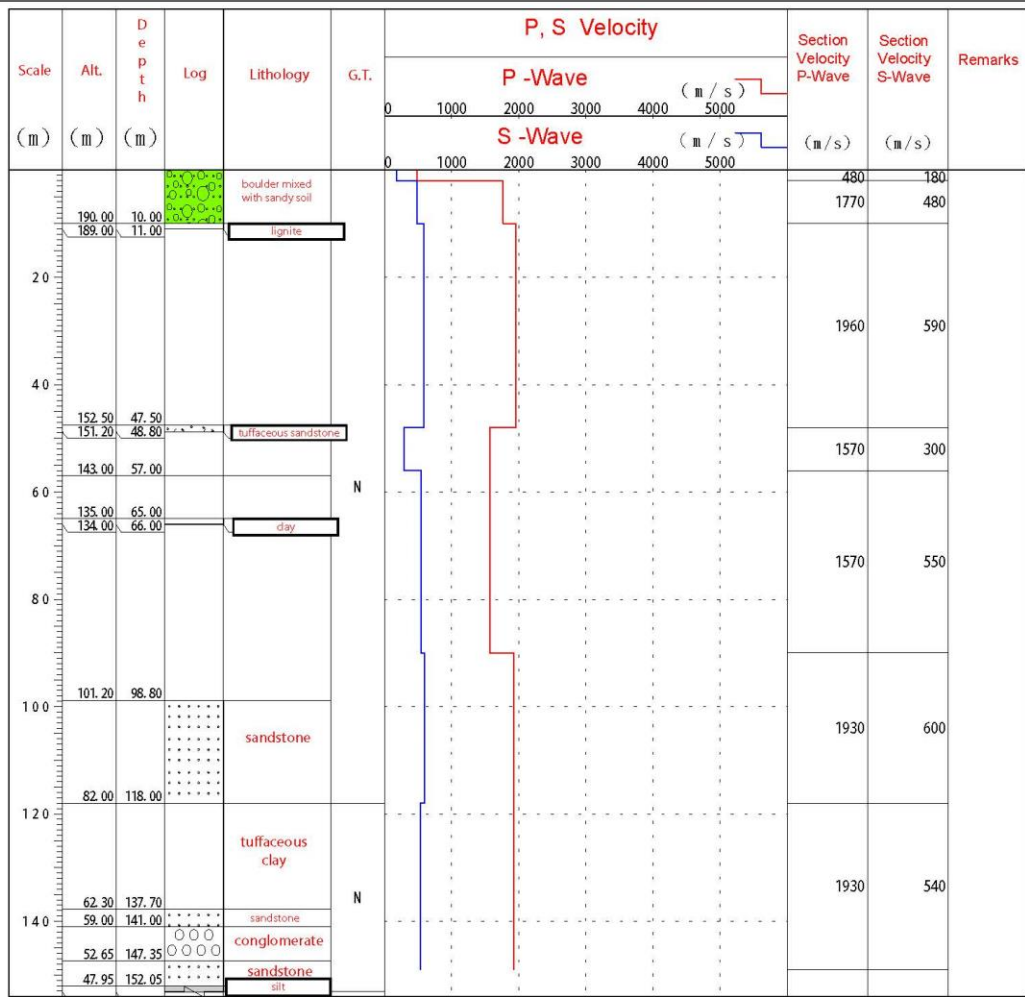
総掘進長： 153.10m



Soil and Rock Condition

Station Point : 金ヶ崎(かねがさき)
 Location : 岩手県胆沢郡金ヶ崎町西根和光183-1
 Latitude : 39° 11' 42.0"
 Altitude : +200m

Station Code : IWTH24
 Longitude : 141° 0' 55.0"
 Depth : 153.10m

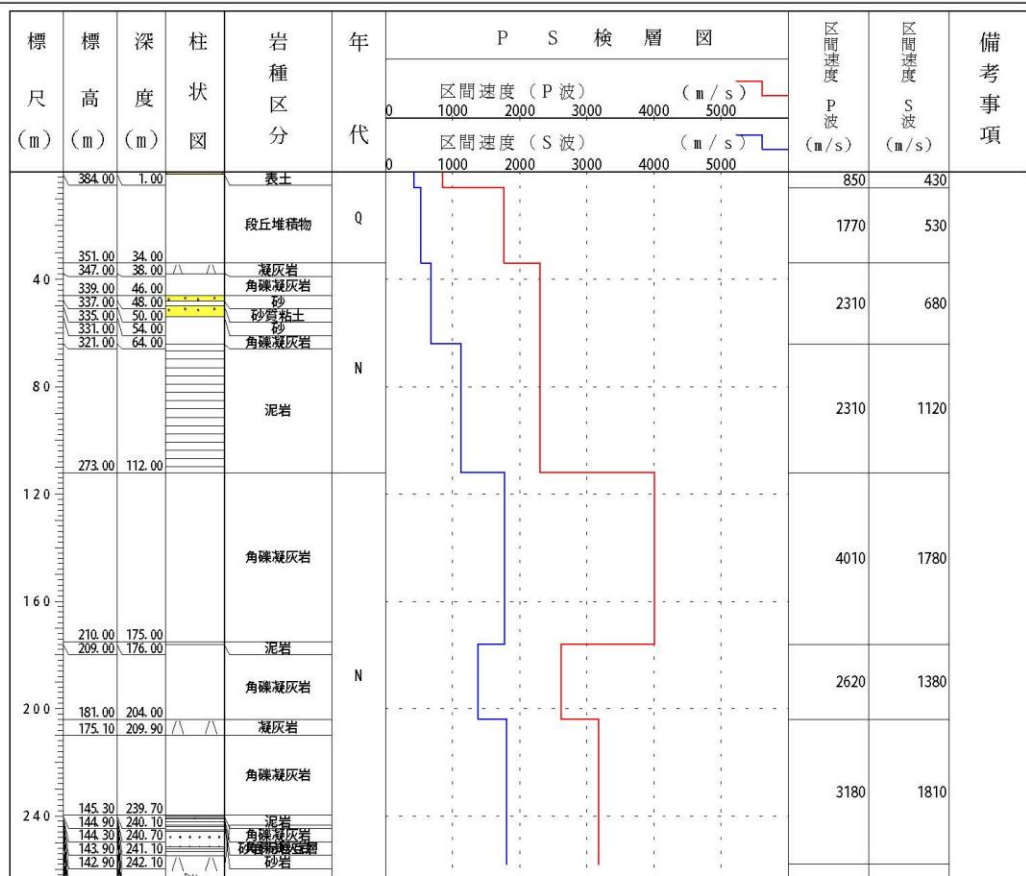


NIED 独立行政法人防災科学技術研究所
 Copyright (c) National Research Institute for Earth Science and Disaster Prevention, All rights Reserved.

ボーリング柱状図(暫定版)

観測点名： 一関西(いちのせきにし)
 所在地： 岩手県一関市巖美町字祭時251
 緯度： 39° 0' 22.0"
 孔口標高： +385m

観測点コード： IWTH25
 経度： 140° 52' 0.0"
 総掘進長： 263.40m

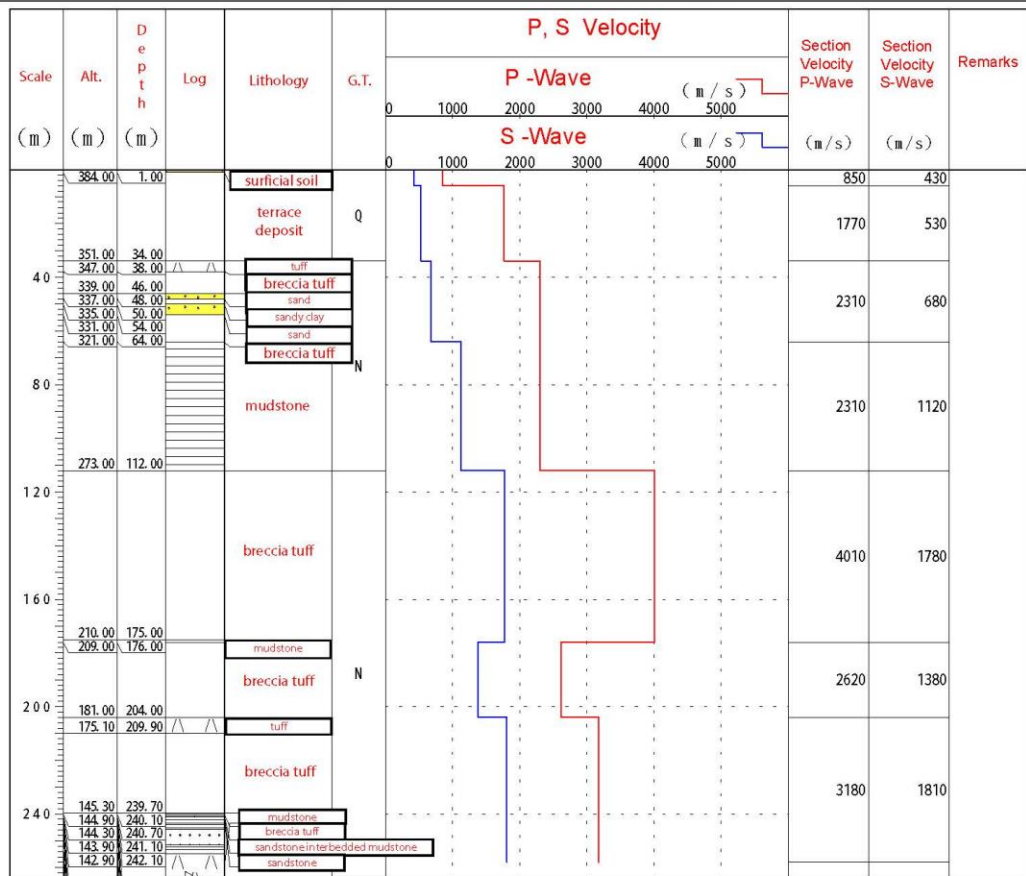


NIED 独立行政法人防災科学技術研究所
 Copyright (c) National Research Institute for Earth Science and Disaster Prevention, All rights Reserved.

Soil and Rock Condition

Station Point : 一関西(いちのせきにし)
 Location : 岩手県一関市巖美町字祭時251
 Latitude : 39° 0' 22.0"
 Altitude : +385m

Station Code : IWTH25
 Longitude : 140° 52' 0.0"
 Depth : 263.40m

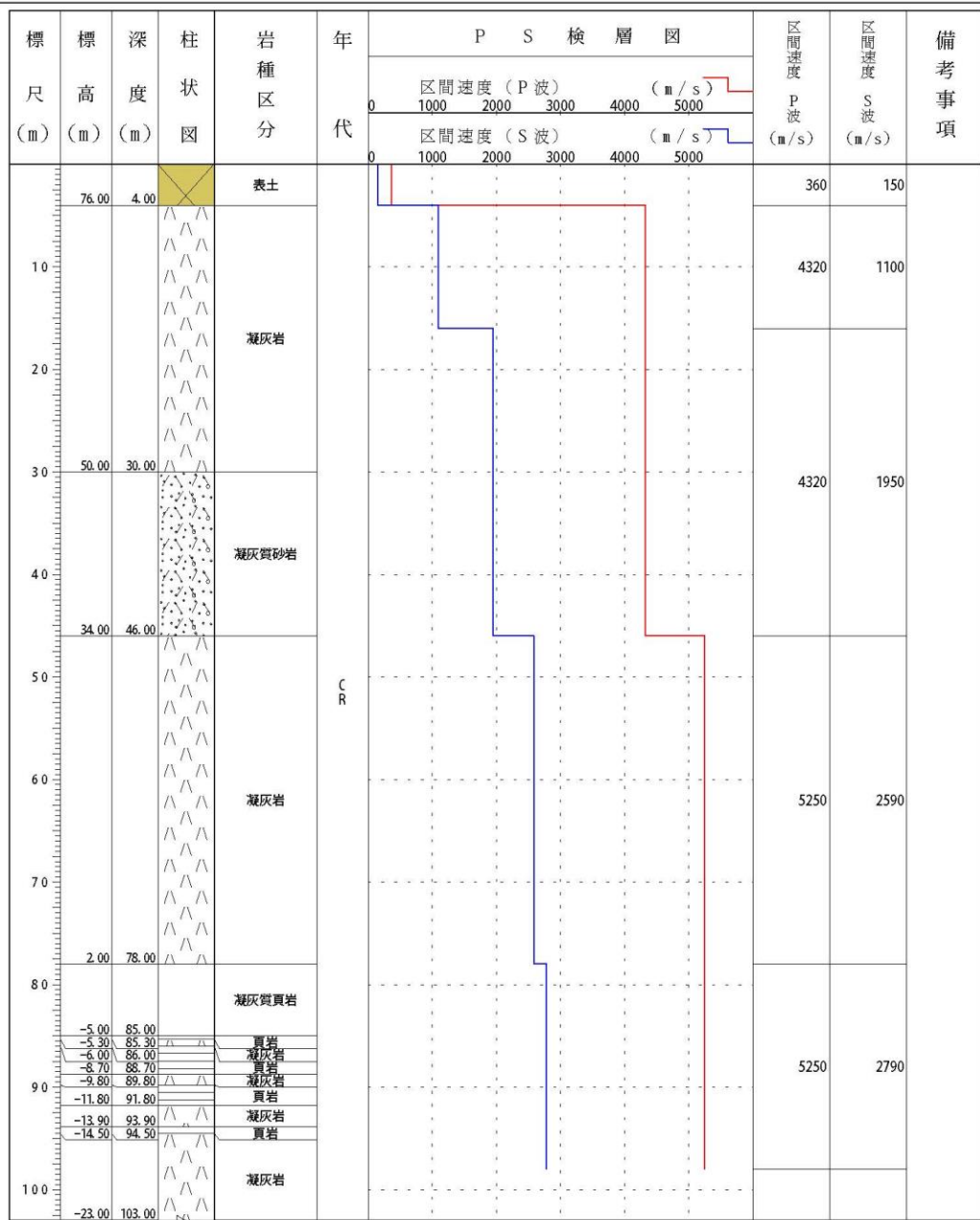


NIED 独立行政法人防災科学技術研究所
 Copyright (c) National Research Institute for Earth Science and Disaster Prevention, All rights Reserved.

ボーリング柱状図(暫定版)

観測点名： 陸前高田(りくぜんたかた)
 所在地： 岩手県陸前高田市矢作町字鍋谷5-2
 緯度： 39° 1' 40.0"
 孔口標高： +80m

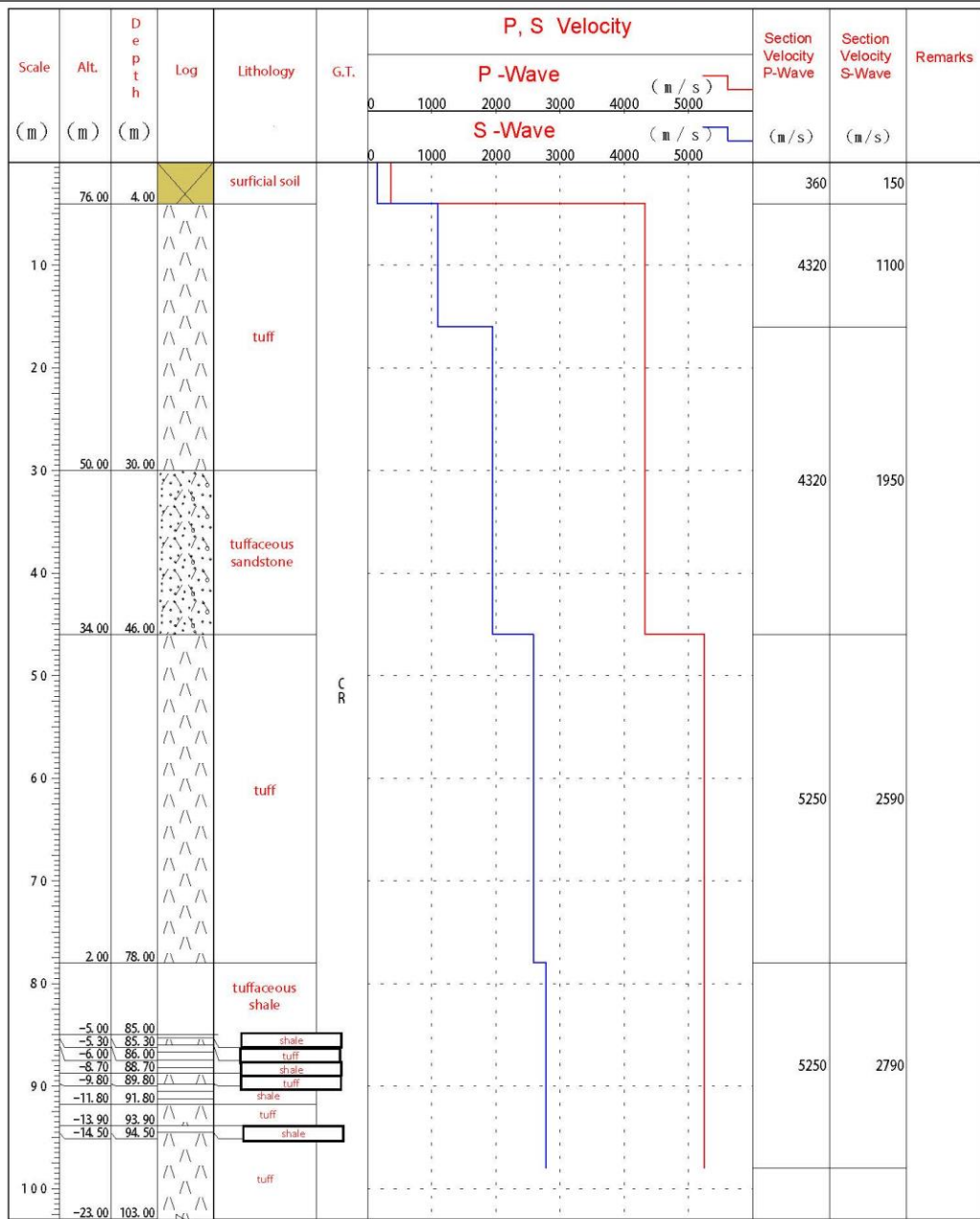
観測点コード： IWITH27
 経度： 141° 32' 8.0"
 総掘進長： 103.00m



Soil and Rock Condition

Station Point : 陸前高田(りくぜんたかた)
 Location : 岩手県陸前高田市矢作町字鍋谷5-2
 Latitude : 39° 1' 40.0
 Altitude : +80m

Station Code : IWITH27
 Longitude : 141° 32' 8.0 ''
 Depth : 103.00m



ボーリング柱状図(暫定版)

観測点名： 田尻(たじり)

所在地： 宮城県遠田郡田尻町小塩字八ツ沢51番地1

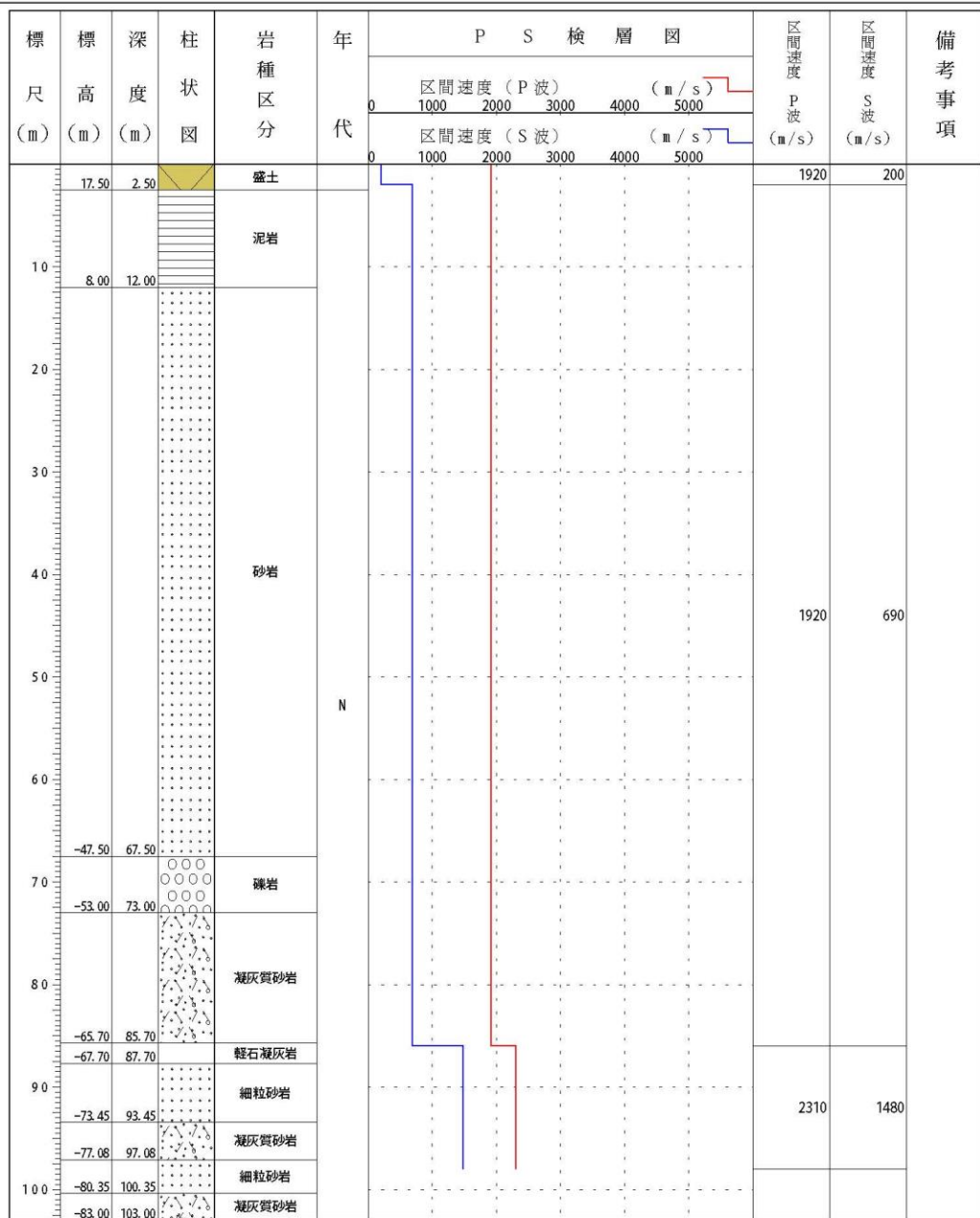
緯度： 38° 35' 16.0"

孔口標高： +20m

観測点コード： MYGH06

経度： 141° 4' 28.0"

総掘進長： 103.00m



Soil and Rock Condition

Station Point : 田尻(たじり)

Location : 宮城県遠田郡田尻町小塩字八ツ沢51番地1

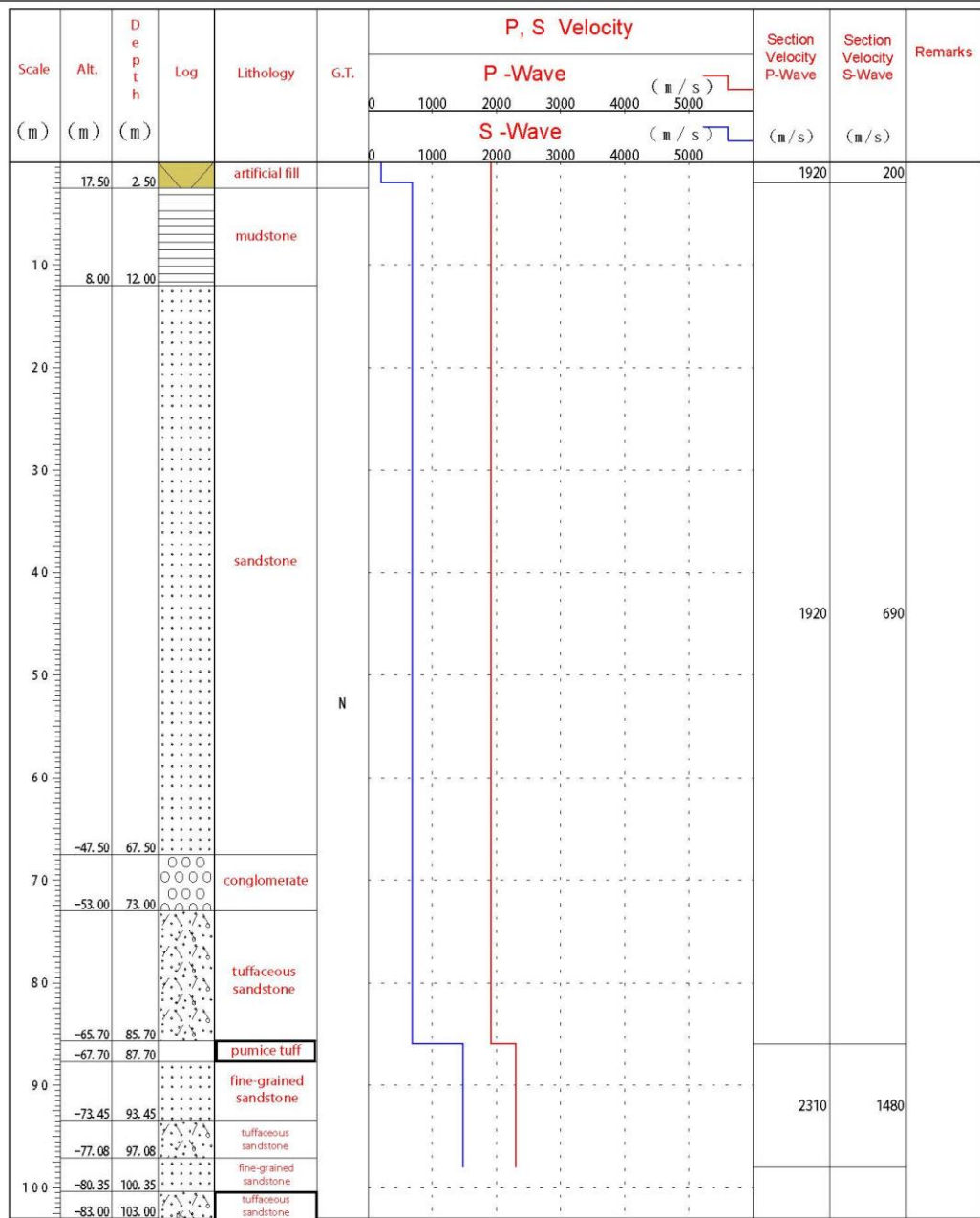
Latitude : 38° 35' 16.0"

Altitude : +20m

Station Code : MYGH06

Longitude : 141° 4' 28.0"

Depth : 103.00m



NIED 独立行政法人防災科学技術研究所

Copyright (c) National Research Institute for Earth Science and Disaster Prevention, All rights Reserved.

ボーリング柱状図(暫定版)

観測点名： 下田(しただ)

所在地： 新潟県南蒲原郡下田村南五百川字山本67-4

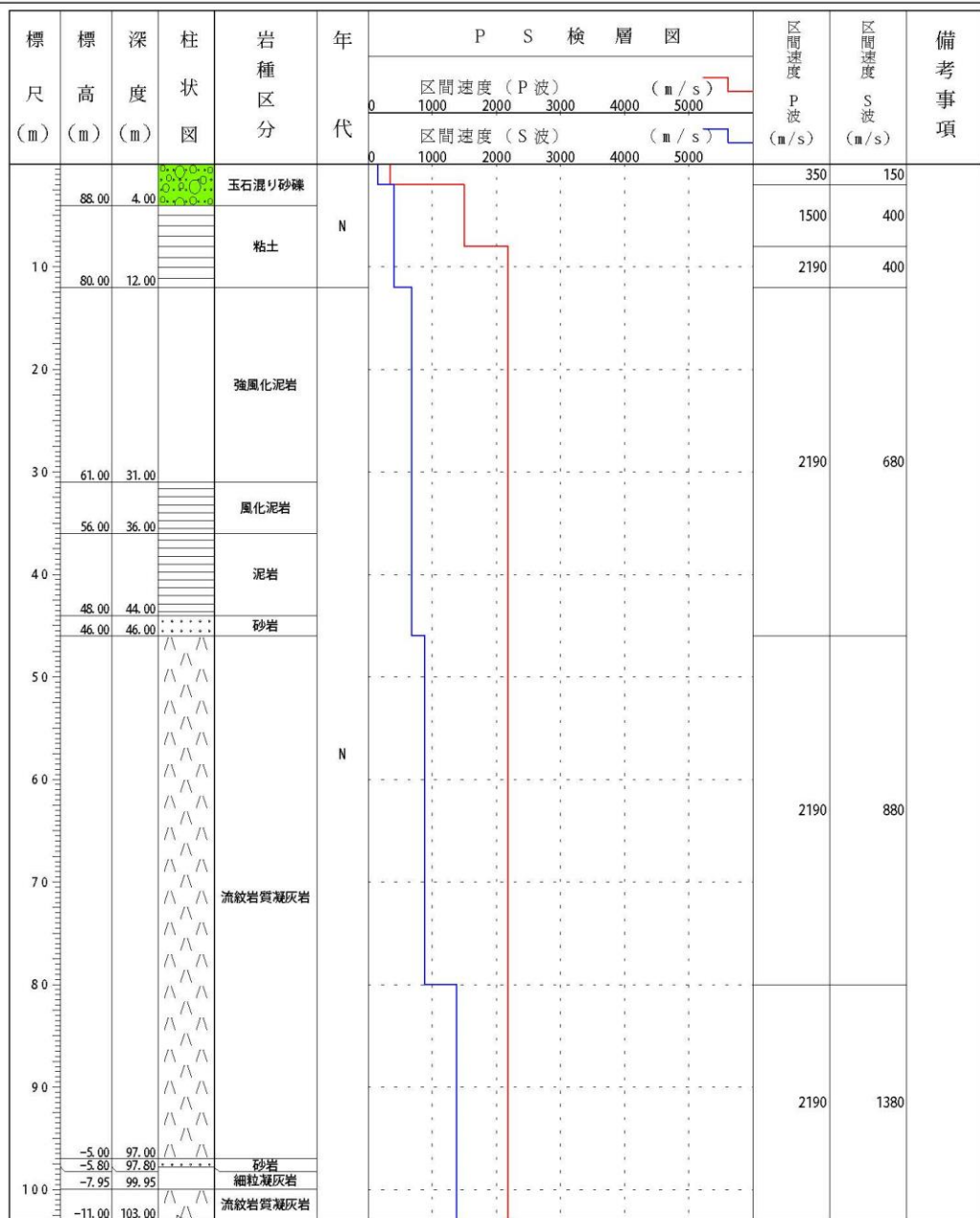
緯度： 37° 32' 8.0"

孔口標高： +92m

観測点コード： N1GH09

経度： 139° 7' 52.0"

総掘進長： 103.00m



Soil and Rock Condition

Station Point : 下田(しただ)

Location : 新潟県南蒲原郡下田村南五百川字山本67-4

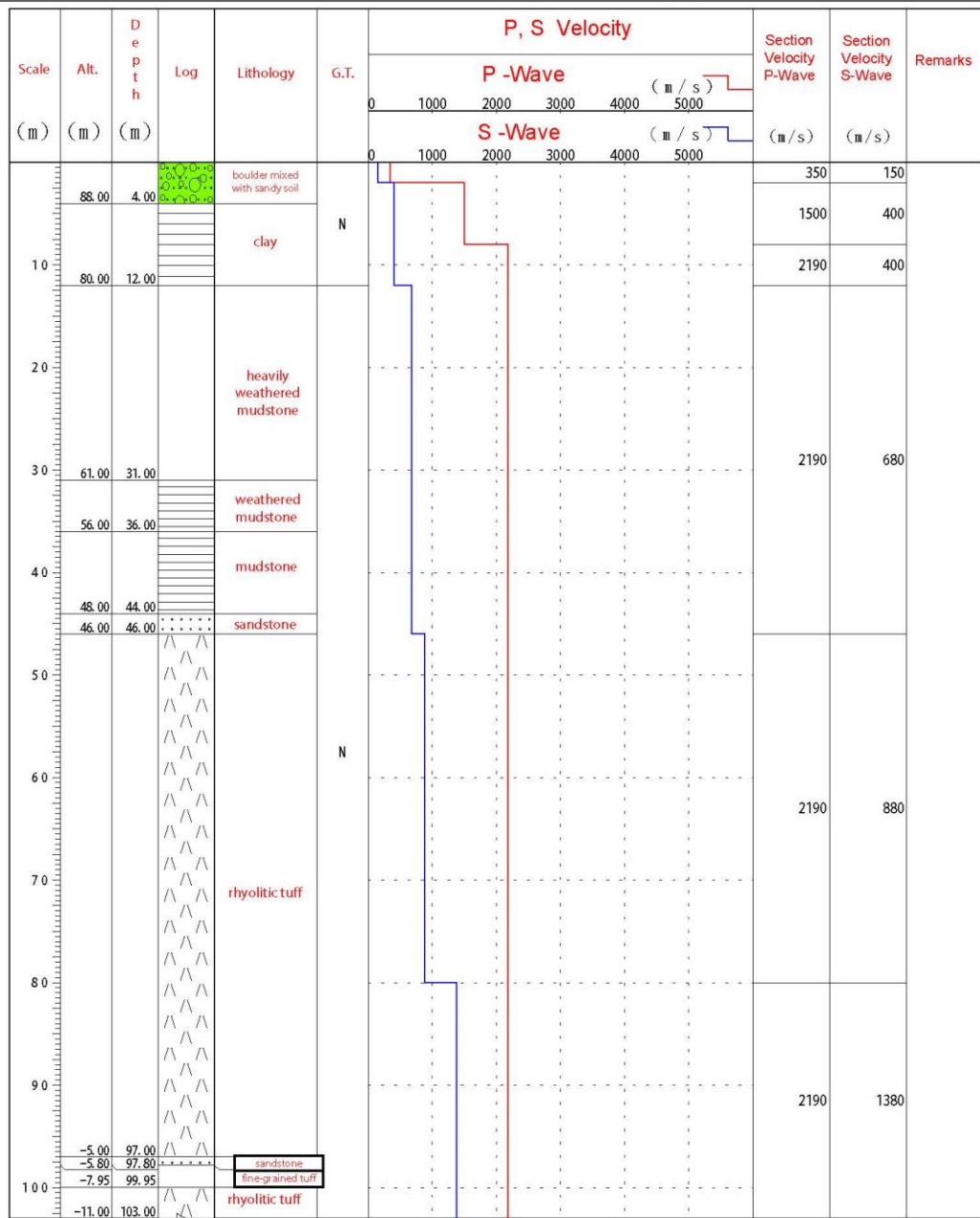
Latitude : 37° 32' 8.0"

Altitude : +92m

Station Code : N1GH09

Longitude : 139° 7' 52.0"

Depth : 103.00m



NIED 独立行政法人防災科学技術研究所
Copyright (c) National Research Institute for Earth Science and Disaster Prevention. All rights Reserved.

Soil & Rock Condition

Station Point: YUNOTANI

Station Code: NIGH12

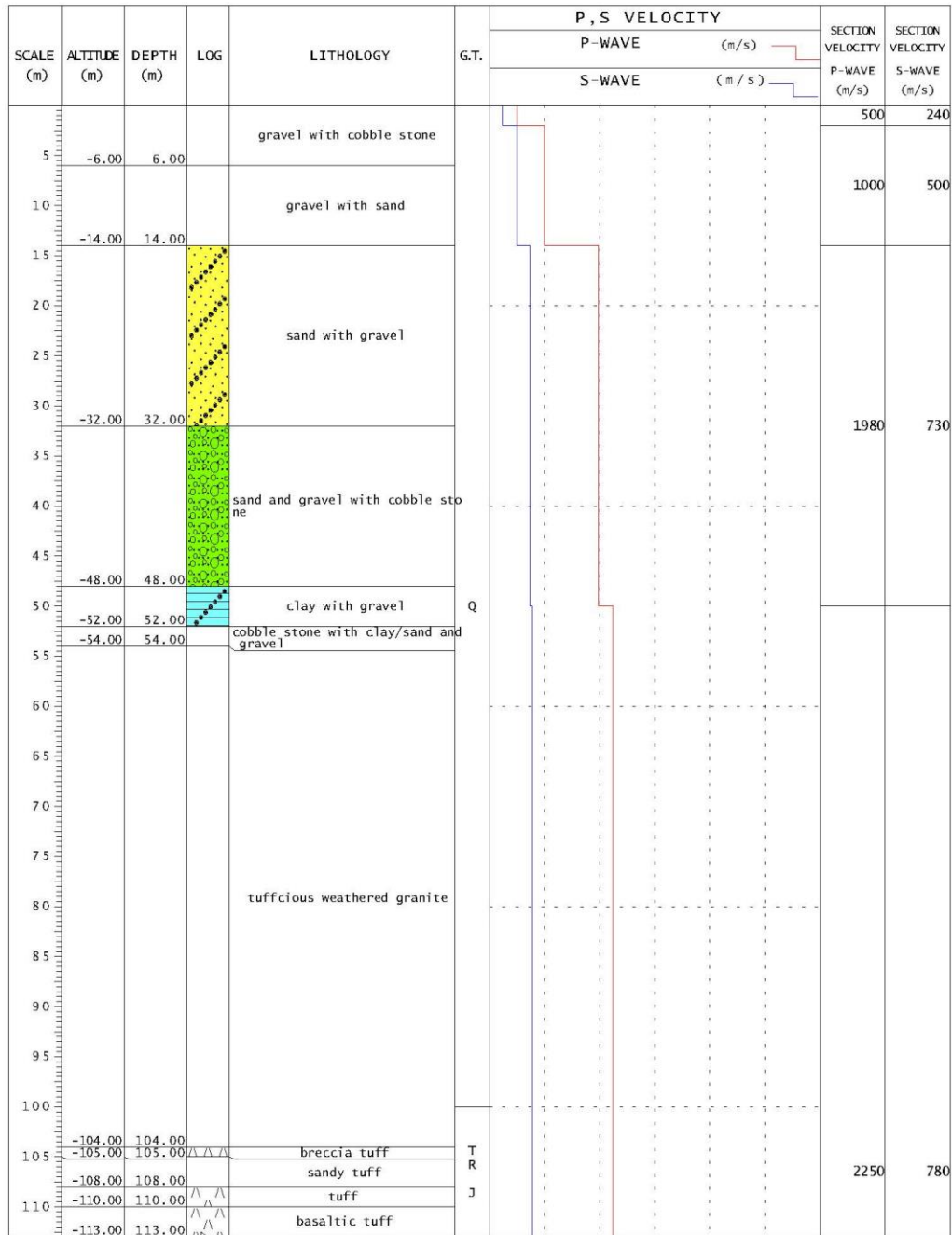
Location : NIIGATAKEN KITALONMAGUN YUNOTANIMURA YOSHIDA 1142

Latitude : 37 deg 13 ' 15.0 ''

Longitude : 138 deg 59 ' 7.0 ''

Altitude : 0m

Depth : 113.00m



Soil & Rock Condition

Station Point: HAKUTA

Station Code: SMNH01

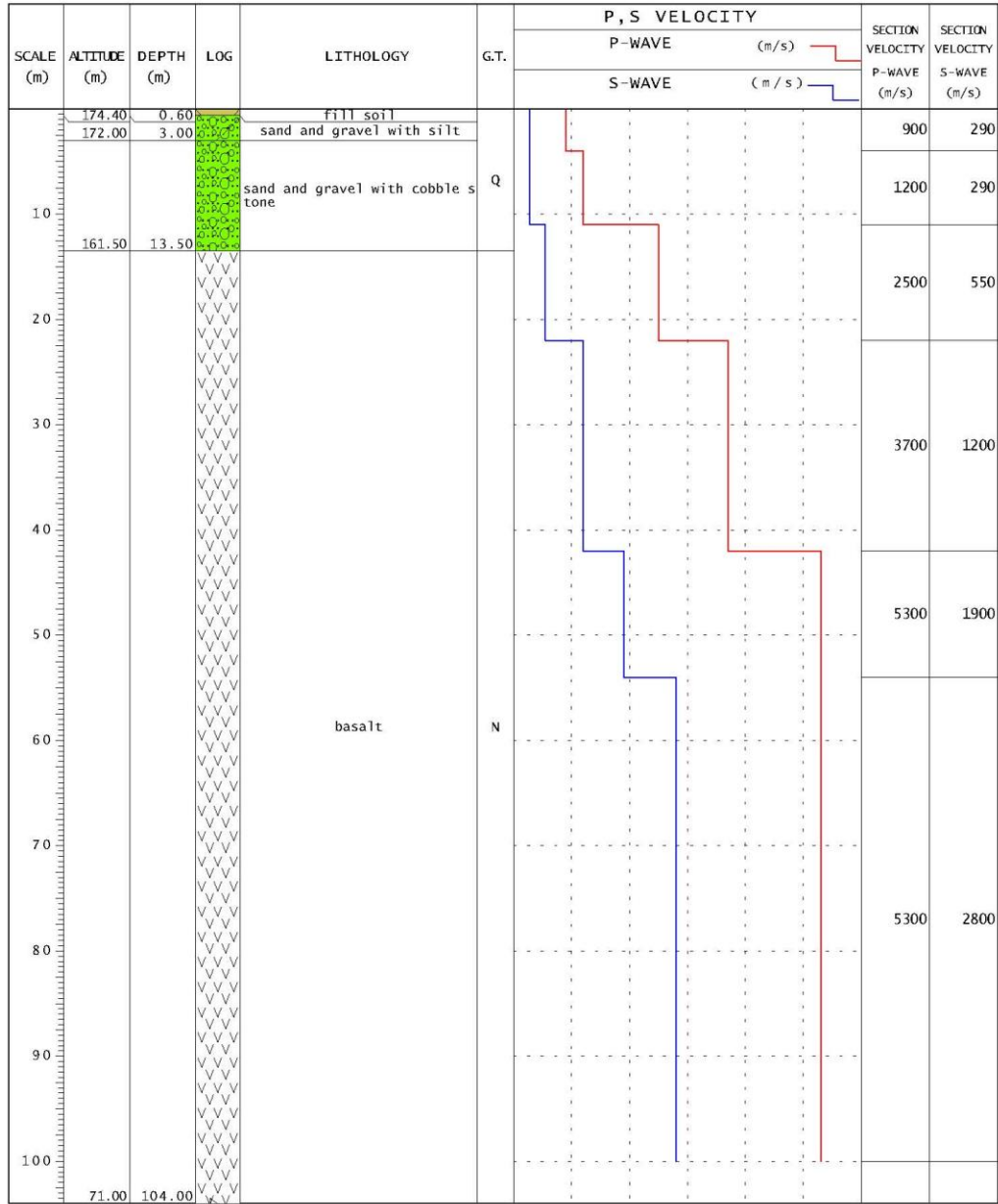
Location : SHIMANEKEN NOGIGUN HAKUTACHO AKAYA 118-2

Latitude : 35 deg 17 ' 35.2 "

Longitude : 133 deg 15 ' 46.1 "

Altitude : +175m

Depth : 104.00m



NIED 独立行政法人防災科学技術研究所
Copyright (c) National Research Institute for Earth Science and Disaster Prevention. All rights Reserved.

References

- 2014 International Building Code*. (2013). Country Club Hills, IL: International Code Council, Inc.
- Google Inc. (2013). Google Earth (Version 7.1.2.2041) [Software].
- KiK-net, Kiban Kyoshin network, URL <http://kik.bosai.go.jp/>.
- Kottke, A. R., & Rathje, E. M. (2008). *Technical Manual for Strata*. Berkeley: Pacific Earthquake Engineering Research Center.
- Kramer, S. L. (1996). *Geotechnical Earthquake Engineering*. New Jersey: Prentice Hall.
- Romo, M. P., & Seed, H. B. (1986). Analytical modelling of dynamic soil response in the Mexico earthquake of September 19, 1985". *ASCE International Conference on the Mexico Earthquakes*, (pp. 134-140). Mexico City.
- Schabel, P. B. (1973). Effects of Local Geology and Distance from Source on Earthquake Ground Motions. *Ph.D. Thesis*. The University of California at Berkeley.
- Zalachoris, G., & Rathje, E. M. (2013). Evaluating One Dimensional Site Response Analysis Using Borehole Arrays. *10th International Conference on Urban Earthquake Engineering*. Tokyo, Japan.